

MAT SCI 361: Crystallography and Diffraction

Michael J. Bedzyk
Northwestern University
Department of Materials Science and Engineering

January 7, 2025

Contents

1 Course Description	2
2 Course Outcomes	2
3 Symmetry of Crystals	3
3.1 Types of Symmetry	3
3.1.1 Mirror Planes and Chirality	3
3.1.2 Proper Rotation Axes	4
3.1.3 Inversion Symmetry	5
3.1.4 Improper Rotation Axes	6
3.2 Symmetry Projections	7
3.2.1 Roto-inversion's Effect on Arrangement of Symmetry-equivalent Objects	8
3.3 Group Theory	13
3.3.1 Matrix Representation of Symmetry Operations	14
4 Crystal Lattices	17
4.1 Indexing within a crystal lattice	17
4.1.1 Hexagonal Prism	18
4.1.2 Form	20
4.1.3 Direction Indices	21
4.1.4 Zone	21
4.2 Lattices	22
4.2.1 Unit cell	24
4.2.2 Plane Groups	24
4.3 Example Graphene	27
4.3.1 Space Lattices or Bravais Lattices	28
4.3.2 Positions Within the Unit Cell	28
4.3.3 Hexagonal Close-Packed Structure HCP	28
4.3.4 Rhombohedral (Hexagonal)	29
5 Ster. Projections	31
5.1 Poles on the Reference Sphere	31

5.2	Projection Plane	33
5.3	Wulff Net	33
5.3.1	Cubic System StereoGrams	34
5.4	Vector Representation of Periodic (hkl) Planes	35
5.5	Reciprocal Lattice Concept	37
5.5.1	Cartesian axial system	40
5.6	Use of Reciprocal Lattice Vectors	41
6	Crystal Structures	49
6.1	Crystal Structure Examples	49
6.2	Voids in FCC	53
6.3	Atomic Sizes and Coordination	54
7	Diffraction	58
7.1	X-ray	58
7.2	Interference	58
7.3	X-ray Diffraction History	60
7.4	How does X-ray diffraction work?	60
7.5	Absent (or forbidden) Reflections	64
8	Absorption/Emission	65
8.1	Spectrometers	65
8.2	Bremsstrahlung Radiation	66
8.3	Synchrotron Radiation	67
8.4	Characteristic Spectrum	69
8.5	Auger Effect	72
8.6	Radioactive Source	73
8.7	X-ray Absorption	74
8.8	X-ray Transmission Filters	77
8.9	Photoelectric effect	79
8.10	X ray scattered by an electron	80
8.11	Theory for Radiation Generating by Accelerated Charge	81
9	Scattering	83
9.1	X-ray Scattering & Polarization	83
9.1.1	Barkla	85
9.2	Thomson Scattering by two electrons	86
9.2.1	Thomson scattering from N electrons	88
9.2.2	X-ray Scattering from an atom with Z electrons in spherically symmetrical distributions	89
9.2.3	Defining Atomic Scattering Factor	89
9.2.4	Calculating the Atomic Scattering Factor	90
9.3	Compton Scattering	92
9.3.1	Anomalous Dispersion	96
9.3.2	Honl's Correction Factors	97
9.3.3	X-ray Scattering by Many Atoms	98
10	Kinematical Theory	99
10.1	Scattering from N atoms	100
10.1.1	Scattered Intensity from N Atoms	100

10.2 Scattering from Small Crystal	101
10.2.1 1D Interference Function Summary	107
10.3 1D Interference Function Example	107
11 Recipriocal Space	109
11.1 Laue condition for diffraction	109
11.1.1 Vector Representation in Reciprocal Space	110
11.1.2 Ewald Sphere	111
11.2 Single Crystal Diffractometer	111
11.3 Diffraction Methods	113
11.3.1 Laue Method - white beam / single crystal	114
11.3.2 Reciprocal lattice treatment of Laue method	115
11.4 Structure Factor Examples	116
11.4.1 Primitive Unit Cell (P)	117
11.4.2 Body-Centred (I) Bravais Lattice	118
11.4.3 Base-Centred (C) Bravais Lattice	119
11.4.4 Face-Centred (F) Bravais Lattice	119
11.4.5 Hexagonal Closed Pack (HCP)	120
11.4.6 More than one atom type per unit cell	121
11.5 Peak Width	122
11.6 Transverse Scan	124
11.7 Polycrystalline Aggregate (Powder sample)	125
11.7.1 Ewald construction	126
11.7.2 Calculated Diffracted Intensity (Power)	126
11.7.3 Multiplicity Correction	127
11.7.4 Powder Diffraction Intensity	127
11.7.5 Absorption Effects	127
11.7.6 Summarize: Powder diffractometer in symmetric reflection geometry	129
11.7.7 Multiplicity Factor	130
11.7.8 Indexing Powder Diffraction Patterns	131
11.7.9 Example 1	133
11.7.10 Example 2	133
11.7.11 Quantitative Analysis	135
11.8 Rotating Crystal Method	136
11.8.1 Rotating Crystal Method	136
11.8.2 Reciprocal Lattice Treatment of Rotating-Crystal Method	137
11.8.3 Ewald Construction for Rotating Crystal Method	139
11.8.4 Bernal Chart	140
12 Temperature Effects	144
12.1 Primitive Unit Crystal	144
12.2 Debye Theory	148
12.3 Powder Diffraction	150
13 Thin Film X-ray Scattering	151
13.1 1-D interference function	152
13.2 Ferroelectric Film	152
13.3 Friedel's Law	154

13.4 PZT thin-film	155
13.4.1 Total External Reflection of X-rays from a Mirror Surface . .	163
13.4.2 X-ray Reflectivity of UDAME monolayer on Si (111) Substrate	166
13.4.3 X-ray Reflectivity Analysis Fundamentals	167
14 Order-Disorder	170
14.1 Order-disorder geometry	170
14.2 Long-range Order	170
14.2.1 Long range order parameter	171
14.2.2 Effective Atomic Scattering Factor	171
14.2.3 Order-disorder phase transitions	172
15 Special Topics	174
15.1 XANES	175
15.2 EXAFS	176
15.3 Outgoing photoelectron: electrons as spherical waves	177
15.4 XAFS spectra of mono and diatomic gases	177
15.4.1 How surrounding atoms affect the modulations	178
15.4.2 How XAFS data is measured: transmission and fluorescence detection	178
15.4.3 Background subtraction: extracting the quasi-periodic modulations	179
15.4.4 E-Space to K-Space conversion	180
15.4.5 The EXAFS equation: Describing the k-space data mathematically	180
15.4.6 What affects the k-space data?	180
15.4.7 Fourier transform	181
15.4.8 How do multiple coordination shells affect the spectrum? . .	182
15.4.9 Recap: Extended X-ray Absorption Fine Structure (EXAFS)	182
15.4.10 The modeling process (crystallography)	183
15.4.11 The EXAFS equation: how do we treat this in creating a model?	184
15.4.12 Variables defined for each pathway	184
15.4.13 Evaluating best-fit model (Statistics)	184
15.4.14 Some Examples: Materials Science problems solved by EXAFS	185

1 Course Description

This course covers elementary crystallography and basic diffraction theory with a reciprocal space perspective. Applications include structure analysis and preferred crystalline orientation. Characterization techniques include both point and 2D detector acquisition and analysis. This course has both lecture and weekly laboratory components.

Prerequisites: GEN_ENG 205 (EA1), Physics 135-2 and 135-3, and Calculus 1-3. We will use linear algebra, as covered in EA1.

2 Course Outcomes

At the conclusion of this course, MAT_SCI 361, students will be able to:

1. Identify different types of 2D and 3D crystal structures and symmetry elements, such as plane groups, space groups, point symmetry, and glide planes, that occur in metals, ceramics, and polymers.
2. Perform standard X-ray diffraction measurements on metals, ceramics, and polymers and quantitatively determine lattice constants, grain size, texture, and strain in bulk crystals and epitaxial films.
3. Describe the basic particle and wave physical processes underlying x-ray emission, elastic and inelastic scattering, absorption, and interference of coherent waves.
4. Identify symmetry elements in (point, translation) in 2D and 3D patterns and crystals.
5. Describe basic principles underlying x-ray tube and rotating anode sources, synchrotron x-ray sources, x-ray fluorescence spectroscopy, and electron and neutron diffraction.
6. Use reciprocal space graphical constructions and vector algebra to interpret diffraction from 3D and 2D single crystals, as well as random and textured polycrystalline samples.

3 Symmetry of Crystals

For the three states of matter—gas, liquid, and solid—solids in thermal equilibrium form crystals. A **crystal** can be defined as a solid composed of an atomic arrangement that is periodic in three dimensions (3D). Crystal systems exhibit various types of **symmetry** which refer to different forms of repetitiveness. The specific symmetry type is determined by a set of operations that, when applied to the crystal, result in its self-coincidence. In other words, a crystal is symmetric concerning a particular operation if it is impossible to distinguish its state before and after that operation.

A macroscopic crystal can be described by detailing the position of each atom using its x, y, and z coordinates. For a crystal measuring 1 mm^3 , this would involve approximately 10^{21} atoms. Fortunately, the field of crystallography enables us to simplify this description by identifying only a small set of atoms with their coordinates, along with a limited number of symmetry operators.

3.1 Types of Symmetry

Symmetry elements can be of the following types:

- ◊ **Rotational axis**
- ◊ **Mirror plane**
- ◊ **Inversion center**
- ◊ **Translation symmetry**

(or a combination of these):

- ◊ **Rotoinversion axis**
- ◊ **Glide plane**
- ◊ **Screw axis**

3.1.1 Mirror Planes and Chirality

Probably the most familiar form of symmetry from daily life is reflection symmetry. We refer to some objects as being symmetric with respect to reflection (or having mirror symmetry) if a mirror cutting through the object would result in no apparent change to the object (we call this lack of change “self-coincidence”). The lines (or planes in three dimensions) on which these hypothetical mirrors could be placed are appropriately called mirror planes. Observe Fig. 3.1, noticing that the image could be replicated by holding half of it up to an appropriately placed mirror. In a sense, symmetry thus allows us to define structures or patterns in terms of unique, fundamental units. Mirror planes will typically be denoted in figures by bold lines. It is also worth noting that the two shapes in Fig. 3.1 have opposite handedness or chirality. The points of the two objects proceed outward in either a clockwise or counterclockwise manner; as a result, the object on the right can be identified as distinct from the one on the left. Thus, we see that a reflection changes the chirality of an object. We encounter this phenomenon in daily life; it is possible to tell a person’s right hand from their left because of the arrangement of their fingers, but

an image of a left hand reflected from a mirror will have the same arrangement as that of a right hand (similar conclusions follow for the reflection of the right hand). In a Cartesian coordinate system, if we place the mirror plane in Fig. 1.1 at $x = 0$, then points (x', y') on the left side are symmetrically equivalent to points (x, y) on the right side by the matrix equation:

$$\begin{pmatrix} x' \\ y' \end{pmatrix} = \begin{pmatrix} -1 & 0 \\ 0 & 1 \end{pmatrix} \begin{pmatrix} x \\ y \end{pmatrix} \quad (3.1)$$

or $x' = -x$ and $y' = y$.

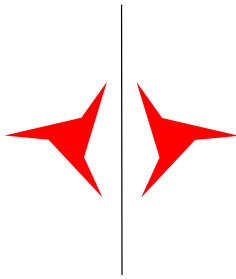


Figure 3.1: A 2D object with mirror symmetry. Note that the two parts of the object on either side of the mirror plane have opposite chirality.

3.1.2 Proper Rotation Axes

A rotational axis refers to a line that can be utilized as the center of a specific rotation that leaves the system (such as a pattern or crystal) unchanged (invariant). Rotational symmetry can exist in both three dimensions (3D) and two dimensions (2D), with the “line” represented as a point in the latter case, indicating lines perpendicular to the plane of view. The planar object pictured in Fig. 3.2 demonstrates 3-fold rotational symmetry, as a 120° or 240° or 360° turn about its center brings it into self-coincidence. In addition, this particular object has three mirror planes, and the object’s reflection across these planes also brings it into self-coincidence.

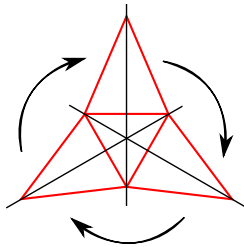


Figure 3.2: A planar object (denoted by red-line segments) that has 3-fold rotational symmetry, as well as three mirror planes denoted by black line segments.

Fig 3.3 shows the types of proper rotation axes that we are concerned with, as well as the symbols that will be used to represent each type. Referring back to Fig. 3.2, the object pictured has 3-fold rotational symmetry about an axis directed out of

the page, as a $360^\circ/3 = 120^\circ$ rotation allows for self-coincidence. In other words, an object has n -fold symmetry about an axis if a $360^\circ/n$ rotation about that axis brings it into self-coincidence. All objects exhibit 1-fold symmetry or are brought into self-coincidence by a full 360° turn about any axis. This case is trivial (hence why there is no associated symbol) but important nonetheless.

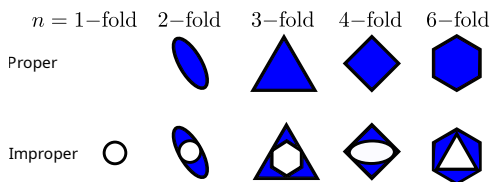


Figure 3.3: Symbols for proper and improper rotational symmetries.

You may notice that other types of rotational axes (i.e., 5, 7, or greater) are not provided. This is because such rotational axes are incompatible with translation symmetry (which will be discussed in Chapter 4). In brief, this simply refers to the fact that objects with, for example, 5-fold symmetry cannot be translated in a way that fills all of space. For instance, Figure 3.4 demonstrates that pentagons cannot be used to fill space without gaps (this is also known as tiling). A parallelogram, which has 2-fold symmetry, can be translated to fill or tile all space in 2D.

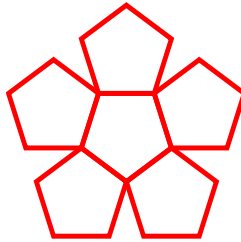


Figure 3.4: An example of an object with 5-fold symmetry that does not (and cannot) fill space.

3.1.3 Inversion Symmetry

An object is said to have inversion symmetry if there is some point (the **center of symmetry**) from which identical elements would be encountered when preceding equidistant forward and backward along a line passing through that point. An example of a planar object with inversion symmetry is pictured in Fig. 3.5. When a line is drawn through the center of symmetry of this planar object, corresponding symmetry equivalent points of the object are equidistant in opposite directions from the center. Open circles are commonly used to denote an inversion center as shown in Fig. 3.5. It will coincide with itself if all points on the object are inverted through the inversion center, which is also on this centerline. In terms of Cartesian coordinates, point (x,y) is equivalent to point $(-x,-y)$ in a planar object with an inversion center (or center of symmetry) at $(0,0)$. You will note that this object also exhibits rotational symmetry, as a 180° turn about its center brings it into self-coincidence. The nature of the inversion operation depends on the dimensionality

of the system. In 2D, inversion symmetry is identical to 2-fold rotational symmetry, while in 3D, inversion is distinct from other symmetries. Note that chiral objects do not have a center of symmetry.

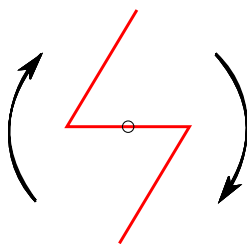


Figure 3.5: A 2D figure with an inversion center and 2-fold rotational symmetry

3.1.4 Improper Rotation Axes

An example of an **improper rotation axis** is the roto-inversion axis (or axis of inversion), a hybrid symmetry operation combining a rotational axis and an inversion center. Note that for a system containing such hybrid operations, it is not necessarily the case that the two-component symmetries are present individually; rather, it is the sequential application of both that results in self-coincidence. This operation only exists in 3D, due to the redundancy of inversion with rotation in 2D. Since this operation is a combination of one that inverts the chirality of objects (inversion) and one that preserves chirality (rotation), it will invert the chirality of components.

Figure 3.3 shows the symbols utilized to denote roto-inversion axes in images. Note that the 1-fold roto-inversion operation ($\bar{1}$) is represented by an open circle, as it is exactly equivalent to the inversion operation (given that 1-fold rotation is equivalent to not changing the structure at all). To help visualize these operations, observe Fig. 3.6, which is adapted from Vainhstein's *Modern Crystallography* Vol I [?]. The arrangements depicted consist of perfectly asymmetrical, three-dimensional, chiral objects related by both proper and improper rotational axes. Note the nature of the 3D inversion operation demonstrated by the $\bar{1}$ example. The $\bar{2}$ operation is equivalent to a mirror plane perpendicular to the axis of roto-inversion.

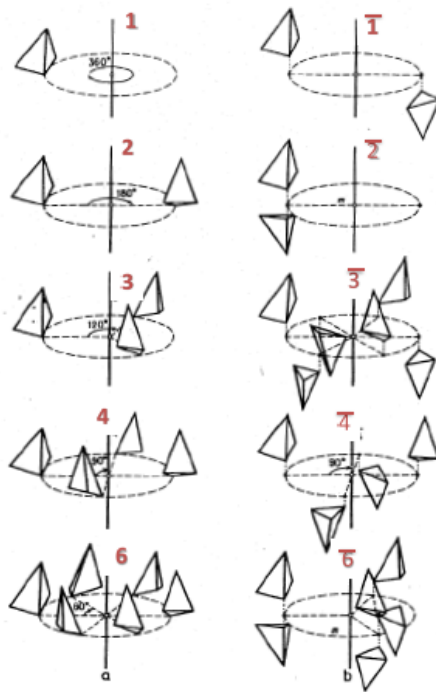


Figure 3.6: Proper Rotation Axes (2D and 3D) and Improper Roto-inversion Axes (3D only), from Vainshtein (Ref. [?])

3.2 Projections of Symmetry Elements and Point Groups

There are simpler ways of representing symmetry operations, namely through a system of **stereographic projections**. A more formal description of stereographic projections will be given in Chapter 3. The top half of Fig. 3.7 depicts a view of a body with its symmetry axis pointing out of the page and the circle representing its perimeter. The symbol in the center indicates the 2-fold rotation symmetry operation, and the two solid circles depict the 180° rotation of the body. The darkened circle in the $\bar{2}$ symmetry operation projection represents a mirror plane.

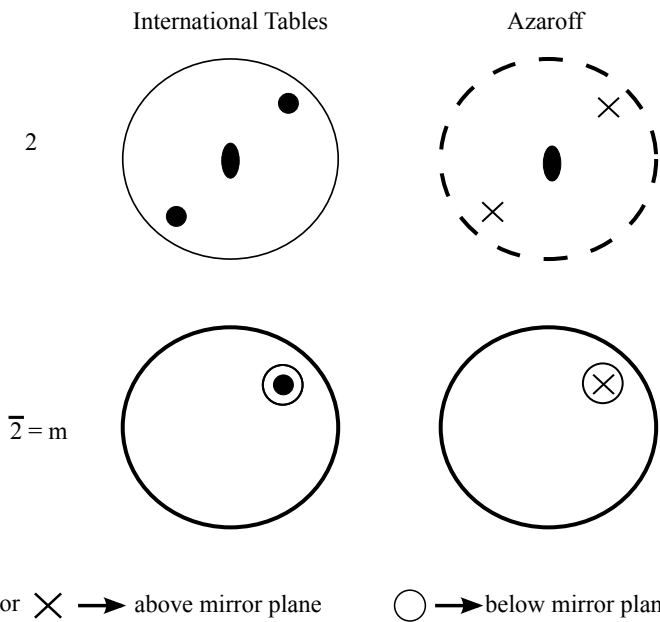


Figure 3.7: Stereographic projection representation of the 2 and the $\bar{2}$ symmetry operations.

3.2.1 Roto-inversion's Effect on Arrangement of Symmetry-equivalent Objects

Let's look at an example. The following steps break down the $\bar{3}$ symmetry operation used to generate the object in Figure 3.8:

1. Start at s_1
2. Rotate counterclockwise 120°
3. Invert to arrive at s_2
4. Rotate counterclockwise 120°
5. Invert to arrive at s_3 ,
6. Continue until you return to s_1
7. \times 's and \circ 's mark all symmetry-equivalent positions (see Fig. 3.6).

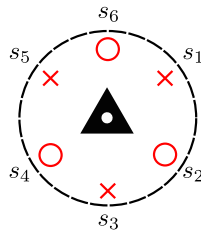


Figure 3.8: $\bar{3}$ symmetry stereographic projection. \times 's represent a geometric entity above the plane, while \circ 's represent the same geometric entity (with opposite chirality) below the plane. s_n (with integer n) represent the steps applied after each $\bar{3}$ operation (starting at s_1) until the entity returns to s_1 . For the 3D representation, see Fig. 3.6.

Certain symmetry elements can be combined to form new patterns, such as the product of a 2-fold and an inversion center shown in 3.9. This produces a 2-fold rotation axis, which is perpendicular to a mirror plane, as indicated by the darkened circle around the object.

Just like an algebraic operation, if **A** is one symmetry operation and **B** is another, they may be grouped through some operator to produce a third symmetry element or **C**.

$$\mathbf{A} \cdot \mathbf{B} = \mathbf{C}$$

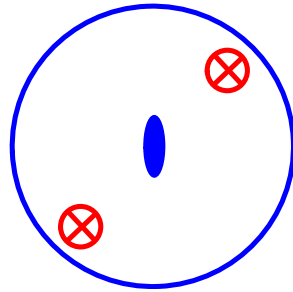


Figure 3.9: Stereographic projection of $\frac{2}{m}$ symmetry operation, which has a 2-fold perpendicular to a mirror plane. Note that $\frac{2}{m}$ is not equivalent to the $\bar{2}$ operation depicted in Fig. 3.6.

For the $2mm$ symmetry operation shown in Fig. 3.10, the mirror plane lies parallel to the rotation axis. There is also a third mirror plane that arises from this combination, as shown by the second line drawn through the center of the dashed circle.

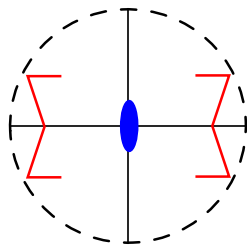


Figure 3.10: Stereographic projection of $2 \cdot m = 2mm$ point group symmetry.

Fig. 3.11 illustrates an object with symmetry that combines two rotation axes. In this case, a 3-fold rotation axis is perpendicular to a 2-fold rotation axis. Note that it does not matter whether the 3-fold or 2-fold operation is performed first, but the **32** point group symmetry is not equivalent to the **23** point group symmetry. Notice that **point group symmetry** refers to the symmetry operators acting on an object about a point at the center of the object that brings that object into self-coincidence.

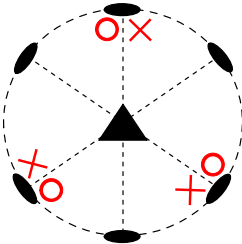


Figure 3.11: Stereographic projection of 32 symmetry, which has a 3-fold perpendicular to a 2-fold rotation axis.

As an example, the SiO_2 , quartz crystal has **32** point group symmetry. A naturally grown quartz crystal is pictured in Fig. 3.12, along with the left- and right-handed habits for this chiral crystal. Note that a chiral object cannot be superimposed onto its mirror image, while an achiral object can be superimposed onto its mirror image. In Fig. 3.13, the placement of the 3-fold and three 2-fold axes are shown for the right-handed quartz crystal habit (perfect shape).

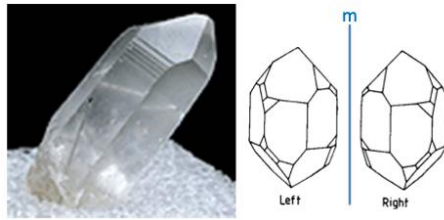


Figure 3.12: Picture of naturally grown SiO_2 , quartz crystal, along with the left- and right-handed habits for this chiral crystal. Copied from Ref. [?].

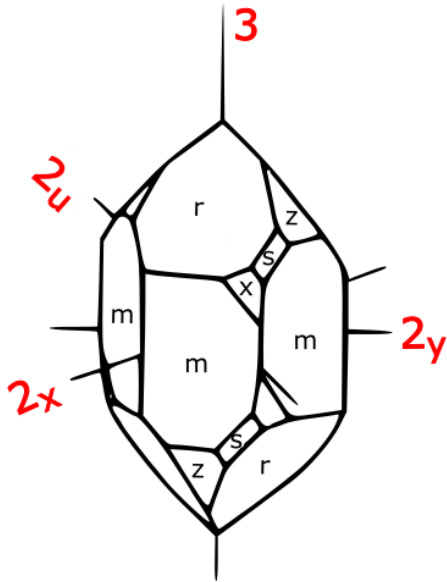


Figure 3.13: Quartz crystal habit showing 3-fold axis perpendicular to the three 2-fold axes, which are separated by 120° . Symmetry equivalent facets (faces) are labeled with the same letter.

Note how the habit is brought into self-coincidence (or is invariant to) the following symmetry operations:

$$\begin{aligned}
 g_0 &= e = 1 \\
 g_1 &= 3 \\
 g_2 &= 3^2 \\
 g_3 &= 2_X \\
 g_4 &= 2_Y \\
 g_5 &= 2_U
 \end{aligned} \tag{3.2}$$

The symmetry operations are referred to in the following way:

- ◊ g_0 is the identity operation, which is rotation about any axis by 360° .
- ◊ g_1 corresponds to rotating by 120° about the 3-fold axis.
- ◊ g_2 corresponds to rotating by 240° about the 3-fold axis in that same direction.
- ◊ g_3 corresponds to rotating by 180° about the 2_X axis
- ◊ *etc.*

Note that successive symmetry operations also bring the object into self-coincidence.

$$g_1 \cdot g_1 = g_1^2 = g_2, \quad g_1 \cdot g_4 = g_3$$

Note that g_1 and g_2 are the inverse of each other and that g_3 , g_4 and g_5 are their own inverse operation.

$$g_1 \cdot g_2 = g_0 \rightarrow g_1 = g_2^{-1} \text{ and } g_3 \cdot g_3 = g_3^2 = g_0 \rightarrow g_3 = g_3^{-1}$$

This set of symmetry elements, $g_0, g_1, g_2, g_3, g_4, g_5$ is called the **32** or **D₃** point symmetry group.

Note that the Cyclic group $C_3 = \{0, 1, 2\}$ under modulo-3 addition is directly analogous to the 3-fold rotation axes point group.

There are only 32 point symmetry groups that can be generated by combinations of the 1, 2, 3, 4, 6, $\bar{1}$, m, $\bar{3}$, $\bar{4}$, $\bar{6}$ symmetry operators. The stereographic projections of all 32 point groups are displayed in Fig. 3.14. Every crystal has a set of symmetry elements that is one of these 32 point groups or **Crystal Classes**. As described in Table 1, crystal classes are further separated into **Crystal Systems** based on minimal symmetry requirements.

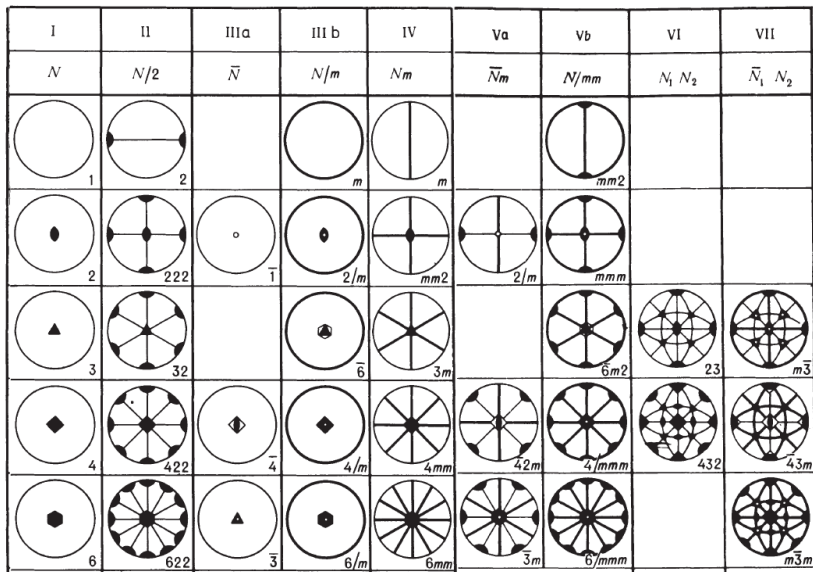


Figure 3.14: Stereographic Projections of 32 Point Groups. Copied from Ref. [?]

Table 1: Crystal Systems and Crystal Classes

Crystal System	Minimal Symmetry	Crystal Classes
Triclinic	1 (or \bar{1})	1, \bar{1}
Monoclinic	One 2 (or \bar{2})	2, m, \frac{2}{m}
Orthorhombic	Three 2's (or \bar{2})	222, 2mm, mmm
Tetragonal	One 4 (or \bar{4})	4, \bar{4}, \frac{4}{m}, 422, 4mm, \bar{4}2m, \frac{4}{m}\frac{2}{m}\frac{2}{m}
Cubic	Four 3's (or \bar{3})	23, 432, \frac{2}{m}\bar{3}, \bar{4}3m, \frac{4}{m}\bar{3}\frac{2}{m}
Hexagonal	One 3 or 6 (or \bar{3} or \bar{6})	3, \bar{3}, 32, 3m, \bar{3}\frac{2}{m}, 6, \bar{6}, 622, 6mm, \bar{6}m2, \frac{6}{m}\frac{2}{m}\frac{2}{m}

Rotation Symmetry Axes of a Cube Referring to Table 1, it might seem surprising that the minimal symmetry requirement for a cube is four 3-fold (or \bar{3}) axes instead of three 4-fold axes. As shown in Fig. 3.15, the 3-fold axes are aligned with the body diagonals of the cube.

3.3 Group Theory

Group Theory Axioms:

1. A group G consists of an operator “multiplication” and a set of elements $g_i \in G$, such that the group is **closed** under “multiplication”. $g_i \cdot g_j = g_k \in G$.

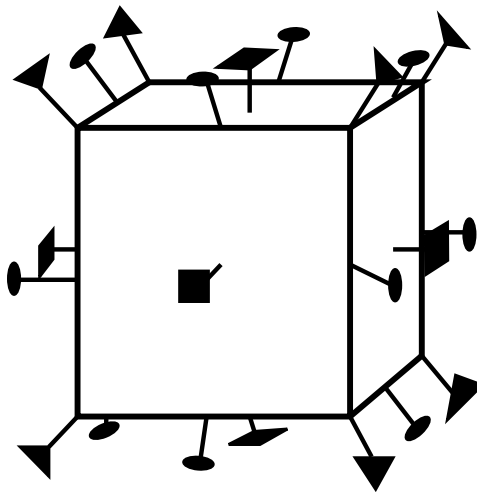


Figure 3.15: Rotation symmetry axes for a cube.

2. "Multiplication" is **associative**: $g_i \cdot (g_j \cdot g_k) = (g_i \cdot g_j) \cdot g_k$
3. There exists an **identity element** $e \in G$, such that $e \cdot g_i = g_i$
4. For any g_i there is an **inverse** $g_i^{-1} \in G$, such that $g_i \cdot g_i^{-1} = e$

Considering the above set of rules, prove to yourself that the set of integers under the addition operator is an example of an infinite group, and the cyclic group $C_3 = \{0, 1, 2\}$ under modulo-3 addition is an example of a finite group.

3.3.1 Matrix Representation of Symmetry Operations

Objects with certain symmetries remain invariant under certain rotations, reflections, inversions, and translations. Each symmetry operation element of a point group can be represented by a matrix \mathbf{A} operating on the x, y, z Cartesian coordinates of an object with that symmetry.

$$\begin{pmatrix} A_{11} & A_{12} & A_{13} \\ A_{21} & A_{22} & A_{23} \\ A_{31} & A_{32} & A_{33} \end{pmatrix} \begin{pmatrix} x_1 \\ y_1 \\ z_1 \end{pmatrix} = \begin{pmatrix} x_2 \\ y_2 \\ z_2 \end{pmatrix} \quad (3.3)$$

such that point (x_2, y_2, z_2) is symmetrically equivalent to (x_1, y_1, z_1)

The **Identity Element** is an element of every point symmetry group.

$$1 \text{ or } E \text{ or } e = \begin{pmatrix} 1 & 0 & 0 \\ 0 & 1 & 0 \\ 0 & 0 & 1 \end{pmatrix} \quad (3.4)$$

Other symmetry operation elements of the **32** point group are:

$$3 = \begin{pmatrix} -\frac{1}{2} & -\frac{\sqrt{3}}{2} & 0 \\ \frac{\sqrt{3}}{2} & -\frac{1}{2} & 0 \\ 0 & 0 & 1 \end{pmatrix} \quad \mathbf{2}_X = \begin{pmatrix} 1 & 0 & 0 \\ 0 & -1 & 0 \\ 0 & 0 & -1 \end{pmatrix} \quad (3.5)$$

$\mathbf{2}_x:$ $\begin{bmatrix} 1 & 0 & 0 \\ 0 & -1 & 0 \\ 0 & 0 & -1 \end{bmatrix} \begin{bmatrix} x \\ y \\ z \end{bmatrix} = \begin{bmatrix} x \\ -y \\ -z \end{bmatrix}$

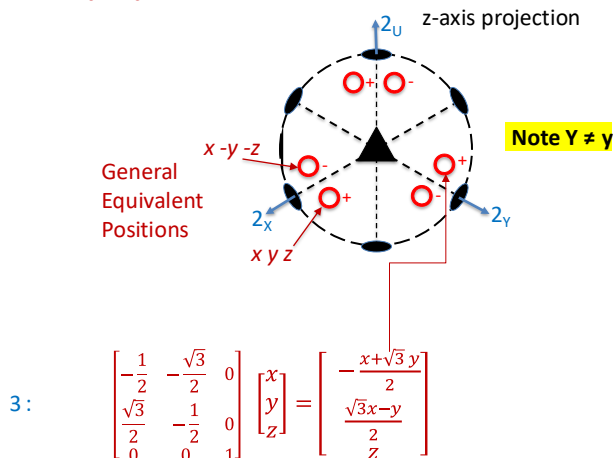


Figure 3.16: Stereographic projection of the 32 point group and symmetry equivalent points (red circles) with their xyz Cartesian coordinates generated by the $\mathbf{3}$ and $\mathbf{2}_X$ matrix operators, which intersect at 000. The z -axis points out-of-the page along the 3-fold. The x -axis points along the $\mathbf{2}_X$. The y -axis points towards approximately 5 O-Clock. A + (or -) sign indicates that the point is at a positive (or negative) z value above (or below) the plane of the paper.

Figure 3.16 illustrates how these two matrices operating on a general point xyz define the Cartesian coordinates of other symmetry equivalent points.

Practice Exercise: Generate the other three symmetry operation elements of the 32 point group, $\mathbf{2}_Y$, $\mathbf{2}_U$, and $\mathbf{3}^2$. Hint, use matrix multiplication, starting with $\mathbf{3}$ and $\mathbf{2}_x$. Show that this is a non-Abelian group; i.e., $\mathbf{3} \cdot \mathbf{2}_x \neq \mathbf{2}_x \cdot \mathbf{3}$. Show that $\mathbf{3}$ and $\mathbf{3}^2$ are inverses of each other. Show that the 2-folds are their own inverses.

Because symmetry equivalent points are equidistant from the origin, a matrix \mathbf{A} representing a point symmetry group operator is an **Orthogonal Matrix**. Therefore, $\mathbf{A}^{-1} = \mathbf{A}^T$ and $\text{Det}[\mathbf{A}] = \pm 1$. Pure rotation matrices (w/o reflection) are orthogonal matrices with $\text{Det} = +1$. This is illustrated in Fig. 3.17. Note that the symmetry operator of a mirror plane at $z = 0$ has $\text{Det} = -1$.

$$\mathbf{3} = \begin{bmatrix} -\frac{1}{2} & -\frac{\sqrt{3}}{2} & 0 \\ \frac{\sqrt{3}}{2} & -\frac{1}{2} & 0 \\ 0 & 0 & 1 \end{bmatrix} \quad \mathbf{3^2} = \begin{bmatrix} -\frac{1}{2} & \frac{\sqrt{3}}{2} & 0 \\ -\frac{\sqrt{3}}{2} & -\frac{1}{2} & 0 \\ 0 & 0 & 1 \end{bmatrix} \quad \mathbf{3 \bullet 3^2} = \begin{bmatrix} 1 & 0 & 0 \\ 0 & 1 & 0 \\ 0 & 0 & 1 \end{bmatrix}$$

$$\mathbf{m} = \begin{bmatrix} 1 & 0 & 0 \\ 0 & 1 & 0 \\ 0 & 0 & -1 \end{bmatrix} \quad x \ y \ z \rightarrow x \ y \ -z \quad \text{Det}[\mathbf{m}] = -1$$

Figure 3.17: Illustration of orthogonal matrices.

4 Crystal Lattices

4.1 Indexing within a crystal lattice

A 2D or 3D crystal is a collection of atoms periodically positioned in 2D or 3D space. This positional periodicity is mathematically described by an infinite array of imaginary points called a 2D plane lattice or a 3D space lattice (or Bravais lattice). Each lattice point has identical surroundings. A repeated unit that generates this lattice is called a unit cell. A 2D unit cell is a parallelogram defined by two non-collinear crystallographic axes **a** and **b**. A 3D unit cell is a parallelepiped defined by three non-coplanar crystallographic axes **a**, **b**, and **c**. In general, there are 6 scalar parameters (called lattice parameters) describing a 3D unit cell: the 3 lengths of the axes a , b , and c , and the angles between them α , β , γ , as illustrated in Figure 4.1. For instance, the cubic crystal system has $a = b = c$, and $\alpha = \beta = \gamma = 90^\circ$. By convention, the c -axis points along the highest rotation symmetry axis.

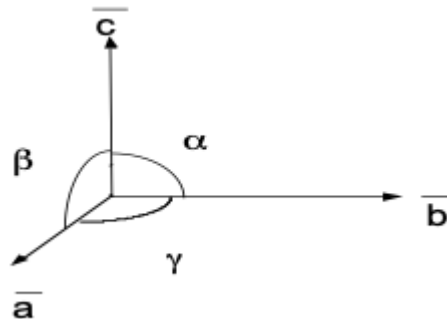


Figure 4.1: The crystallographic axes **a**, **b**, and **c** and angles separating them α , β , γ .

The crystal axes are used to specify the orientation of planes within the crystal lattice structure using **hkl Miller indices**. The following procedure is used to determine the Miller indices of a plane.

1. Determine the plane's intercepts with the crystal axes
2. Take reciprocals of the intercepts
3. Remove common factors
4. Put in (), no commas

All parallel planes have the same (hkl) Miller indices. If a plane crosses through the origin, as shown in the left axes of Figure 4.2, it can be translated to determine its intercepts. By convention, a bar over the number indicates a negative index.

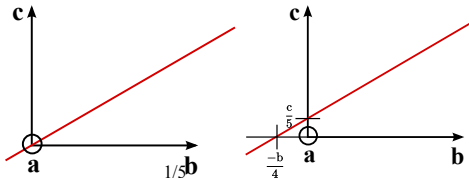


Figure 4.2: To determine the Miller indices of a plane passing through the origin, change its position, but not its direction. The red line is an edge-on view of a plane parallel to the \mathbf{a} -axis.

$$\mathbf{a}, \mathbf{b}, \mathbf{c} \text{ Intercepts: } \infty, -\frac{1}{4}, \frac{1}{5}$$

$$\text{Reciprocals: } 0, -4, 5$$

$$\text{Miller Indices: } (0\bar{4}5)$$

Miller indices: If you need an additional refresher on Miller indices, the Wikipedia page (https://en.wikipedia.org/wiki/Miller_index) is very helpful. Here, we include a reminder of the notation used to indicate planes and directions.

- ◊ **Specific planes:** We use round brackets (as [parentheses](#)) - (hkl)
- ◊ **Planes of the Form:** To indicate all planes that are crystallographically equivalent, we use curly brackets - $\{hkl\}$
- ◊ **Specific direction:** We use square brackets - $[uvw]$
- ◊ **Class of directions:** To indicate all directions that are crystallographically equivalent, we use angle brackets - $\langle hkl \rangle$

Determine the hkl indices of the plane shown in the figure below:

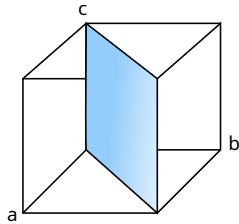


Figure 4.3: Plane in cubic unit cell

Note: The six faces of a cube are of the form (or family) $((100))$ or $\{100\}$

4.1.1 Hexagonal Prism

Indices of hexagonal prism faces are not of the same hkl form. Instead, a redundant index i is introduced to identify planes, in which $i = -(h+k)$ or $\mathbf{a}_1 + \mathbf{a}_2 = -\mathbf{a}_3$. Thus, there are only three independent indices. The four-index $(hkil)$ **Bravais-Miller** system more easily defines planes within a hexagonally structured crystal. Figure 4.4 shows indexing within a hexagonal structure using the three Miller indices. Figure 4.5 uses the a_1, a_2, a_3, c axes in the Bravais-Miller scheme.

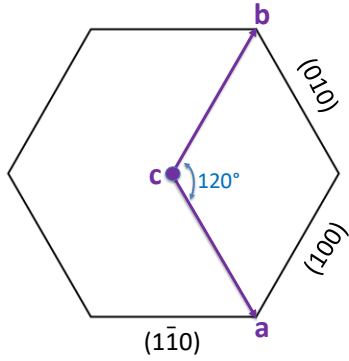


Figure 4.4: The hexagonal unit cell crystallographic axes **a**, **b** and **c** and the (hkl) Miller indices for three nonparallel faces of a hexagonal prism.

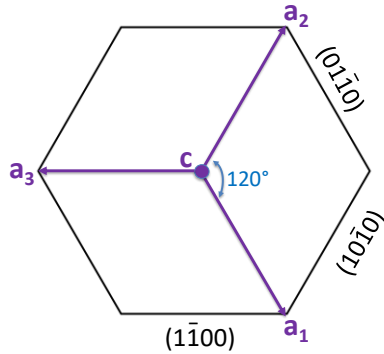


Figure 4.5: The $(hkil)$ Bravais-Miller indices for three nonparallel faces of a hexagonal prism.

By using the Bravais-Miller scheme, the symmetry equivalent faces are all of the same form $\{1\bar{1}00\}$.

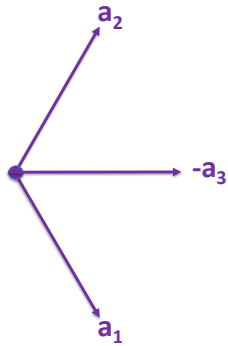


Figure 4.6: Notice that by vector addition $\mathbf{a}_1 + \mathbf{a}_2 = -\mathbf{a}_3$

4.1.2 Form

Planes (or faces) of a **form** are related by crystal symmetry but have different indices. For instance, the six square faces of a cube (100), (010), (001), ($\bar{1}00$), (0 $\bar{1}0$), and (00 $\bar{1}$), are of the form ((100)) or {100}. These planes are all related by the 4-fold rotation axes perpendicular to the cube faces. Note that a form is indicated by the indices of one plane enclosed in braces or {hkl}.

Example: Referring to the octahedron shown in Fig. 4.7, the eight faces are of the form {111}. What Crystal System does this octahedron belong to?

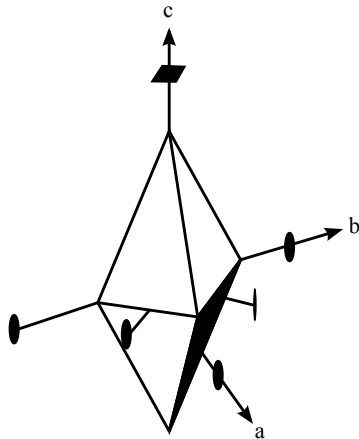


Figure 4.7: Octahedron formed by eight congruent isosceles triangles (From Azaroff Fig. 1-24 [?])

4.1.3 Direction Indices

Direction indices $[uvw]$ define a direction with respect to the unit cell axes **a**, **b**, and **c**.

$$[uvw] = u\mathbf{a} + v\mathbf{b} + w\mathbf{c} \quad (4.1)$$

Figure 4.8 demonstrates direction indices with respect to unit cell axes.

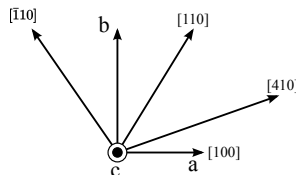


Figure 4.8: Orthorhombic unit cell example of direction indices $[uvw]$, where u, v , and w are integers of the lowest denomination.

4.1.4 Zone

Planes of a **zone** intersect at a line $[uvw]$ known as a **zone axis**, to which they are all parallel. All (hkl) planes that contain this line belong to the same zone. For a book, the spine would be the zone axis, while the pages would be planes belonging to the zone.

For instance:

- ◊ Let σ_{hkl} be the normal vector for the plane (hkl) .
- ◊ Then $\sigma_{hkl} \cdot [uvw] = 0$ if the hkl plane belongs to $[uvw]$ zone
- ◊ For cubic (and only for a cubic) unit cell $\sigma_{hkl} = c[hkl] \rightarrow hu + kv + lw = 0$
- ◊ $[010]$ is the zone axis for $(001), (100), (102), (10\bar{2})$ planes in Fig. 4.9.

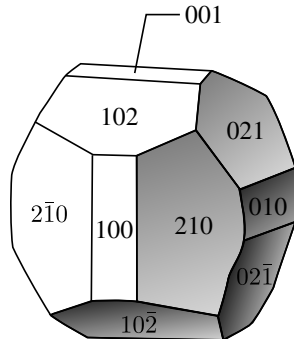


Figure 4.9: Habit with labeled planes. What is the cubic point group?

4.2 Lattices

A **crystal structure** is a periodic array of repeated, identical objects, i.e. 7's, atoms, molecules, ions, etc. Each object (or motif) has identical surroundings. Periodicity is generated by translation symmetry operators $\mathbf{t}_1, \mathbf{t}_2, \mathbf{t}_3$. A crystal structure is a lattice plus a set of atoms identically assigned to each lattice point.

The entire infinite array of objects can be described by giving the structure within the unit cell and by giving $\vec{\mathbf{t}}_1, \vec{\mathbf{t}}_2, \vec{\mathbf{t}}_3$, which defines the infinite lattice by their linear combination $n_1\mathbf{t}_1 + n_2\mathbf{t}_2 + n_3\mathbf{t}_3$.

1-D	t_1	(a)
2-D	t_1, t_2	(a,b)
3-D	t_1, t_2, t_3	(a,b,c)

Table 2: Translation symmetry operators.

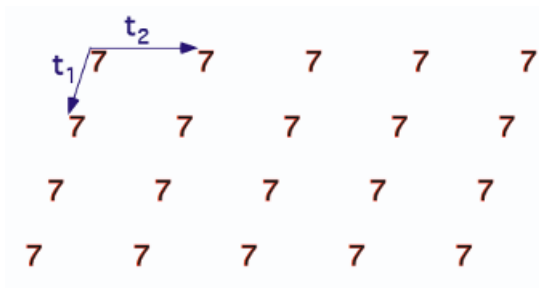


Figure 4.10: 2D periodic array of 7's defined by a single 7 at the origin and repeated by the linear combination of translation symmetry operators $n_1\mathbf{t}_1 + n_2\mathbf{t}_2$, where coefficients n_1 and n_2 are integers.

Lattice points are an imaginary set of periodic points that make up the vertices of a unit cell and are translated to create an array pertaining to the crystal's structure. Each lattice point has identical surroundings.

2-D → Plane Lattice

3-D → Space Lattice

There are five possible plane lattices, or ways to arrange points in two-dimensional space, such that each has identical surroundings. The five plane lattices, shown in Figure 4.11, include the oblique *P*-lattice, rectangular *P*-lattice, rectangular *C*-lattice, square *P*-lattice, and hexagonal *P*-lattice.

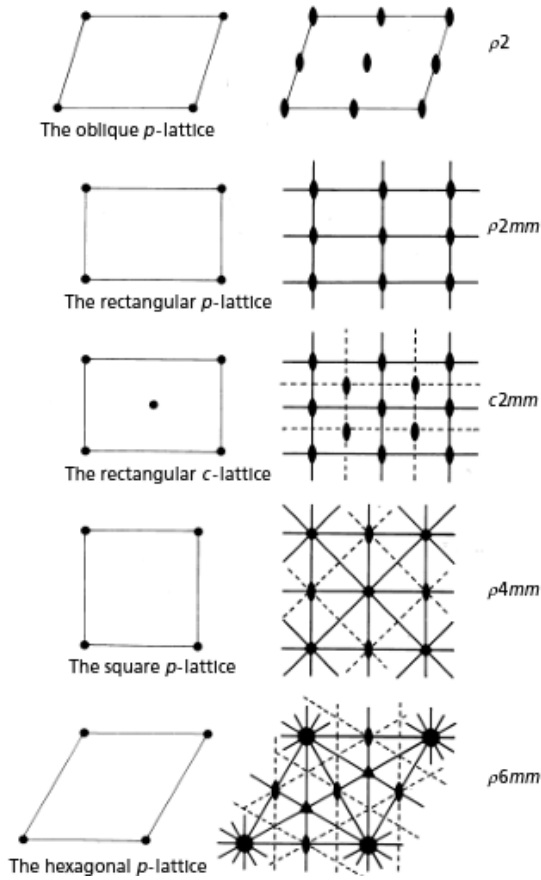


Figure 4.11: The five plane lattices are shown on the left side. An example of a plane group belonging to each plane lattice is shown on the right. (Hammond Fig. 2.4 [?])

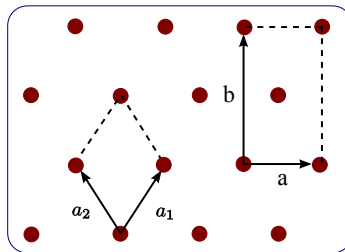


Figure 4.12: The Rectangular-C plane lattice is described by a non-primitive unit cell with 2 lattice points per unit cell: one at the corners (shared by 4 surrounding unit cells) and one at the center. The primitive unit cell for this lattice (diamond) is also shown with $a_1 = a_2$ and $\gamma \neq 90^\circ$.

Azaroff	International Tables
Parallelogram	Oblique p
Rectangular	Rectangular P
Diamond	Rectangular C
Triangular	Hexagonal P
Square	Square P

Table 3: Two different naming conventions for the five 2D plane lattices

The five types of plane lattices are grouped into **four axial systems**.

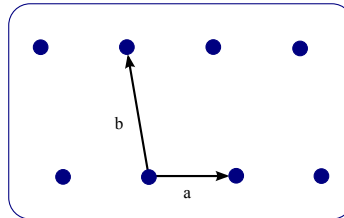
Oblique	1	$a \neq b$	$\gamma \neq 90^\circ$
Rectangular	m	$a \neq b$	$\gamma = 90^\circ$
Hexagonal	3	$a = b$	$\gamma = 120^\circ$
Square	4	$a = b$	$\gamma = 90^\circ$

Table 4: Four axial systems for 2D lattices, along with their minimal symmetry requirements and lattice vector conditions.

Note: Only 1,2,3,4,6 are consistent with translation symmetry.

4.2.1 Unit cell

A **unit cell** is defined as a small region of space chosen to represent a lattice. For 2D lattices, it is defined by cell edges \mathbf{a} , \mathbf{b} . The repeated translation of the cell by \mathbf{a} , \mathbf{b} generates the infinite lattice.

**Figure 4.13:** Unit cell edges

A **primitive unit cell** has one lattice point per cell and uses the smallest possible area to represent the lattice. A **non-primitive unit cell**, such as the rectangular-c unit cell in two dimensions, contains more than one lattice point within the unit cell and is conventionally and conveniently chosen to emphasize the symmetry of the lattice.

4.2.2 Plane Groups

Two-dimensional point symmetry is combined with two-dimensional translation symmetry to create a **plane group**, as shown in Figure 4.14.

$$A \cdot t = B \quad (4.2)$$

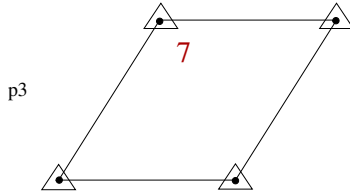


Figure 4.14: 3-fold and hexagonal translation operators are combined to create the $p3$ plane group. Using these symmetry operators, place the other 7s into this figure. Now look for additional point symmetry elements and draw them in as well.

There are 17 such **plane groups** from which any two-dimensional periodic pattern may be classified. The shorthand names of these plane groups, as shown in Figure 4.15 below, are generated by the following scheme: the “1” represents no symmetry other than translation symmetry, the integers indicate the type of rotational symmetry, the “ m ” indicates the presence of a mirror plane and the “g” stands for glide symmetry. **Glide symmetry** is a hybrid symmetry resulting from the combination of a mirror reflection followed by a translation along the mirror line direction. The first image in Figure 4.16 demonstrates a familiar mirror plane symmetry, with R’s reflected across the solid lines, while the second image shows reflection with one R translated half a lattice spacing down. The dashed lines in the second image indicate a special type of symmetry known as a reflection glide or a glide line of symmetry. The glide lines give this pattern a translational form of symmetry along the lattice rather than a simple reflection. In crystal structures, this shift in glide symmetry would only be observable in an electron microscope, which allows for observation of distances of the order of 0.5–2 Å (50–200 pm). Lastly, note that 3-fold symmetry axes do not exist in oblique, rectangular, or square lattices.

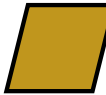
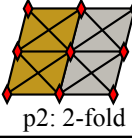
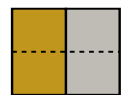
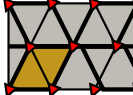
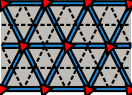
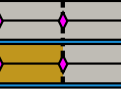
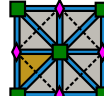
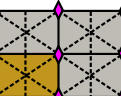
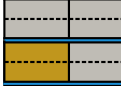
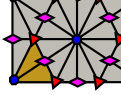
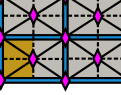
pure rotations	rotation & reflection	pure reflections
 p1: 1-fold		 pm: mirror
 p2: 2-fold		 pg: glide
 p3: 3-fold	 p3m1	 pmm: 2 mirrors
 p31m	 p31m	 pmg
 p4: four-fold	 p4m	 pgg
		Centered cells:  cm
 p6: 6-fold	 p6m	 cmm

Figure 4.15: 17 Plane Groups. Any 2D periodic patterns can be classified as one of these.

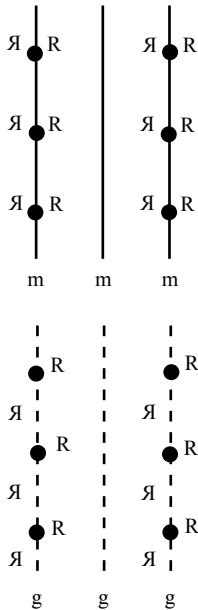


Figure 4.16: Mirror Plane and Glide Symmetry in the pm plane group at the top and the pg plane group at the bottom

4.3 Example Graphene

2D Crystal Structure

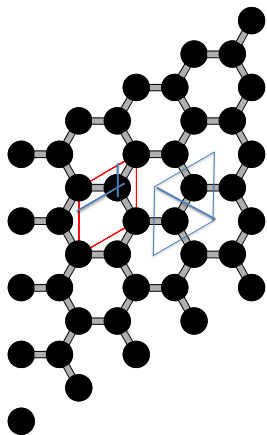


Figure 4.17: Ball-and-stick model of graphene, showing sp^2 bonded carbons in a honeycomb pattern. Identify the 2D unit cell, symmetry operators, plane lattice, and plane group.

4.3.1 Space Lattices or Bravais Lattices

Points in 3-D space can be arranged such that each has identical surroundings in 14 ways. These are divided into **7 Crystal Systems**.

Crystal System	Lattice Types		
Triclinic	P	$a \neq b \neq c$	$\alpha \neq \beta \neq \gamma$
Monoclinic	P,C	$a \neq b \neq c$	$\alpha = \gamma = 90^\circ \neq \beta$
Orthorhombic	P,I,F,C	$a \neq b \neq c$	$\alpha = \beta = \gamma = 90^\circ$
Tetragonal	P,I	$a = b \neq c$	$\alpha = \beta = \gamma = 90^\circ$
Trigonal	P,R	$a = b = c$	$\alpha = \beta = \gamma \neq 90^\circ$
Hexagonal	P	$a = b \neq c$	$\alpha = \beta = 90^\circ; \gamma = 120^\circ$
Cubic	P,I,F	$a = b = c$	$\alpha = \beta = \gamma = 90^\circ$

P: Primitive (1/cell) I:Body-Centred (2/cell) C: Base Centered (2/cell)
F: Face Centered (4/cell) R:Rhombohedral pattern in Hex. Cell (3/cell)

Table 5: 7 Crystal Systems. The number of lattice points per unit cell is listed at the bottom.

4.3.2 Positions Within the Unit Cell

The origin of a unit cell is arbitrarily chosen. By convention, it is the highest symmetry point. The position of any point in the unit cell is given by fractional translations along the \vec{a} , \vec{b} , and \vec{c} directions, written with no parentheses. Table 6 notes the positions of lattice points using this scheme.

Translation to an identical point is achieved by applying the translation symmetry operator: $\mathbf{t} = n_1\mathbf{a} + n_2\mathbf{b} + n_3\mathbf{c}$, where n_i is an integer.

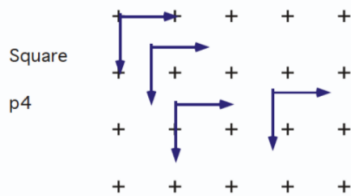


Figure 4.18: Possible locations for origin of unit cell for a square lattice

Body Centered	I	$000; \frac{1}{2}\frac{1}{2}\frac{1}{2}$
C-Centred	C	$000; \frac{1}{2}\frac{1}{2}0$
Face Centered	F	$000; \frac{1}{2}\frac{1}{2}0; \frac{1}{2}0\frac{1}{2}; 0\frac{1}{2}\frac{1}{2}$

Table 6: Lattice Point locations for non-primitive unit cells

4.3.3 Hexagonal Close-Packed Structure HCP

- ◊ At room temperature Zn, Mg, or Be have an HCP crystal structure.

Note that the HCP structure has two atoms per hexagonal-P unit cell (or two atoms per lattice point). The 000 and $\frac{1}{3}\frac{2}{3}\frac{1}{2}$ points do not have equivalent surroundings; therefore, only the 000 point qualifies as a lattice point.

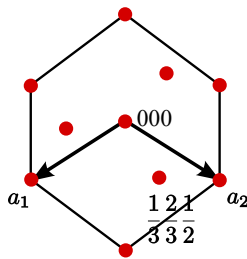


Figure 4.19: c-axis projection of HCP . The atom (red dot) at the origin is also a lattice point. The red dots located in the center of the equilateral triangles and halfway up the c-axis are not at lattice points.

4.3.4 Rhombohedral (Hexagonal)

The Hex-R lattice can be described by a primitive or by a non-primitive unit cell.

For a Rhombohedral Primitive Cell:

- ◊ 1 lattice point per unit cell at 000

For a Hexagonal R Non-Primitive Unit Cell:

- ◊ 3 lattice points per unit cell at 000, $\frac{2}{3}\frac{1}{3}\frac{1}{3}$, $\frac{1}{3}\frac{2}{3}\frac{2}{3}$

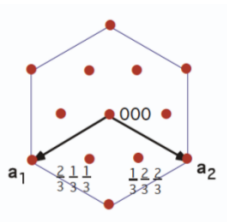


Figure 4.20: Hexagonal R Non-Primitive Unit Cell

Counting Lattice Points: 1 corner point per unit cell at 000, since 8 corners are shared with 8 neighboring unit cells.

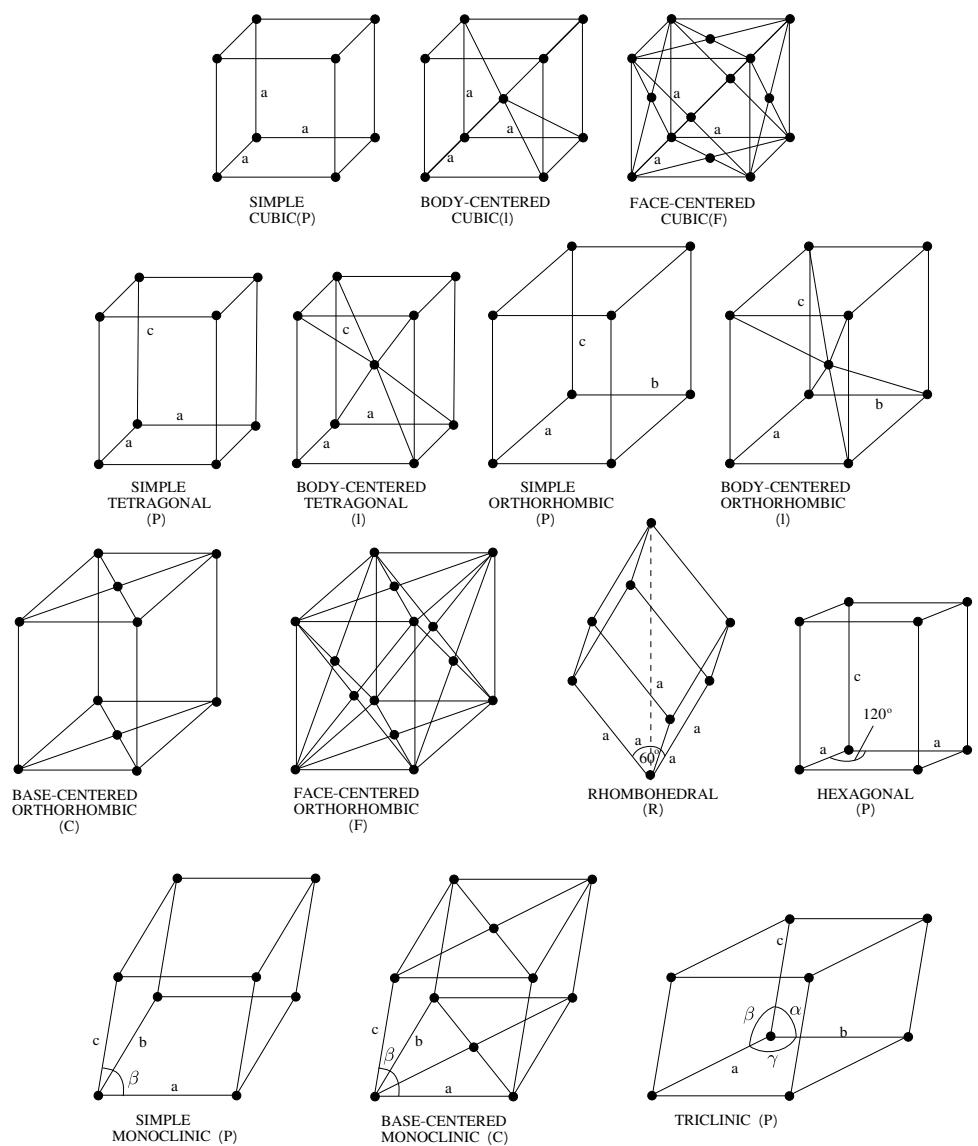


Figure 4.21: 14 Bravais Lattices. Based on Cullity and Stock (Ref. [?]).

5 Stereographic Projections

Recall the regular octahedron illustrated in Figure 5.1 exhibiting the $m\bar{3}m$ point group symmetry.

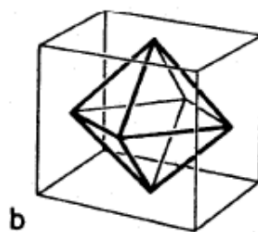


Figure 5.1: Octahedron - Cubic Crystal System

How did we position the symmetry rotation axes and mirror planes in the 2D projection of the $m\bar{3}m$ point group shown in Fig. 5.2?

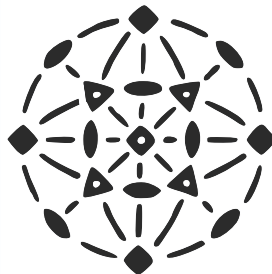


Figure 5.2: Stereographic Projection of the regular octahedron's symmetry elements, which corresponds to the $m\bar{3}m$ point group.

5.1 Poles on the Reference Sphere

Stereographic projections are a two-dimensional graphical representation of the directions of crystal planes in a three-dimensional crystal. Stereographic projections allow for easy visualization of crystallographic features and determination of the angle separating any two crystallographic directions. Looking at Figure 5.3, the normal to the (hkl) plane of the unit cell at the center of the sphere, (σ_{hkl}) , intersects the reference sphere at the hkl pole.

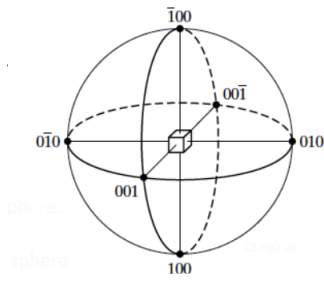


Figure 5.3: A cube at the center of a reference sphere. The (100) faces of the cube have surface normals that intersect the sphere at poles labeled 010 , etc..

Consider that all hkl planes pass through the center of the reference sphere, such as the two planes shown in Fig. 5.4. Their two surface normals form poles P_1 and P_2 . The two planes, when extended, intersect the reference sphere to form two great circles **traces**. The angle α between the two planes and their respective surface normals can be measured on the surface of the reference sphere by measuring the angle between their two traces (Angle-True). Or better yet, by measuring the partial great circle arc length between poles P_1 and P_2 . The center of a **great circle** coincides with the center of the reference sphere. All other circles on the reference sphere are referred to as **small circles**. In geography, the equator and longitudinal lines (meridians) are examples of great circles. The latitudinal lines (except the equator) are examples of small circles.

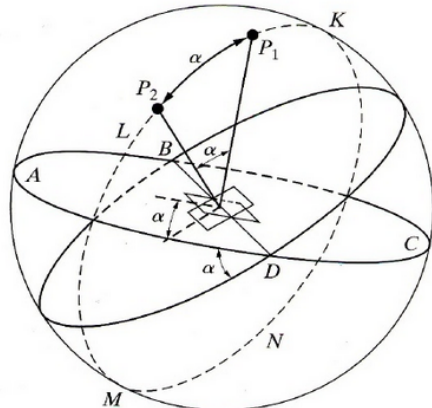


Figure 5.4: Reference Sphere with two planes passing through its center separated by angle α . Also shown are the traces, normal vectors, and poles P_1 and P_2 for the two planes.

Rather than awkwardly measuring angles between planes on the surface of the sphere, we employ an equiangular stereographic projection. Geographers, by the way, use an equal-area projection.

5.2 Projection Plane

Figure 5.5 demonstrates how a stereographic projection is constructed.

- ◊ Start with a plane at the center "C" of the reference sphere.
- ◊ A point of projection "B" is selected on the reference sphere.
- ◊ The projection plane is constructed perpendicular to diameter BCA, tangent to the sphere at point "A".
- ◊ The normal to the plane forms pole "P" on the reference sphere.
- ◊ The projection of pole P forms line BPP', which intersects the projection plane at point P'.
- ◊

Note the projections of the great circles.

- ◊ The projection of N E S W = N' E' S' W' , which is the basic circle. All projected poles lie within this basic circle.
- ◊ The projection of W A E B = W' A' E'.
- ◊ The projection of N A S B = N' A' S'.

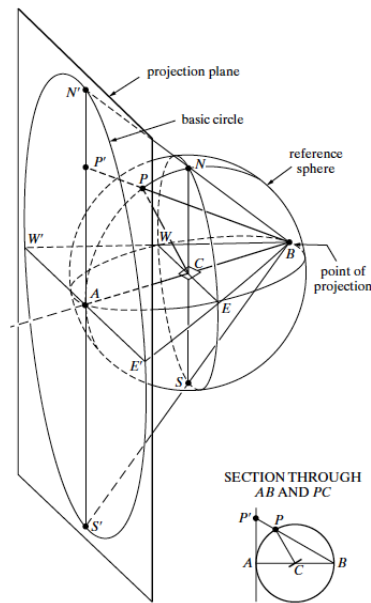


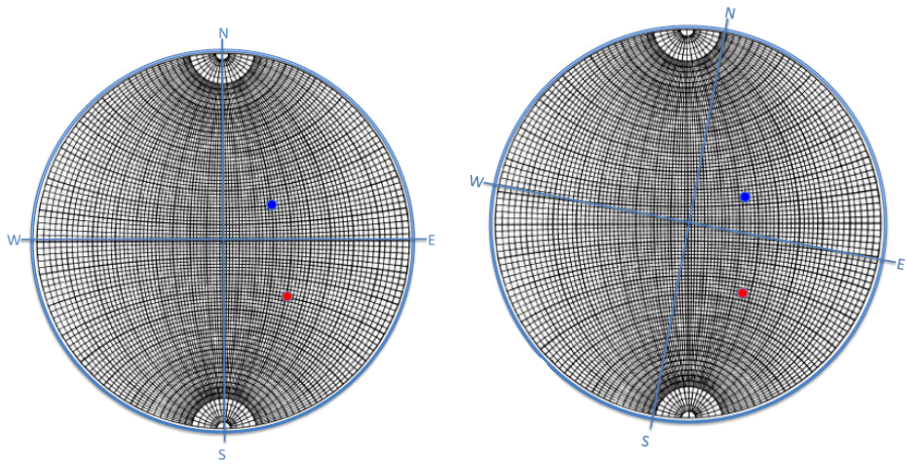
Figure 5.5: Projections onto the projection plane from poles on the reference sphere.
Copied from Cullity and Stock Fig. 2-30. [?]

5.3 Wulff Net

A Wulff Net is used to make angle measurements on the projection plane between planes using their projected poles from the reference sphere. Referring to Fig. 5.6,

the Wulff Net has a circular outer perimeter directly corresponding to the NESW basic circle shown in Fig. 5.5. The projections of other great circles appear as the EW equator and a set of longitudinal lines in 2° increments. Starting from the center of the Wulff Net and moving laterally outward, the angles increase from 0° to 90° . Angles between poles are measured along great circles (longitudinal lines, basic circle, or equator). The horizontal arcs are projections of **small circles** in 2° increments.

To find the angle between two planes, rotate the projection around until both poles lie on the same great circle, as shown in Figure 5.6.



Pole P1 at 20°N , 30°E

Pole P2 at 30°S , 40°E

Rotate until both poles lie on the same great circle $\rightarrow 50^\circ$ angle between the planes

Figure 5.6: Wulff Net

5.3.1 Cubic System StereoGrams

Figure 5.7 illustrates the (001), (110), and (111) stereographic projections of cubic system poles for low-indexed (hkl) planes superimposed on Wulff nets. That is, the pole at point A in Fig. 5.5 is the (001), (110), and (111) for these three standard projections. Looking at the stereograms, you can use the Wulff net mesh to determine the angles separating two hkl planes whose projected poles lie on the projection of a great circle that aligns with a longitude or the equator of the Wulff net. For example, from the leftmost stereogram, you should be able to estimate that the angle between the (001) and (101) planes is 45° and between (111) and (101) is 35.3° . To use the Wulff net to measure the angle between two poles whose projections do not coincide with a longitude or equator, simply rotate the Wulff net about its central axis until both poles lie on the same longitude or on the equator. This follows the principle that arcs measured along a great circle of the reference sphere are angle-true.

Recall that for the cubic system (and only for the cubic system),

- ◊ The normal vector to the (hkl) plane, $\sigma_{hkl} = c[hkl] = ha + kb + lc$.
- ◊ For the cubic system, **a**, **b**, and **c** are mutually orthogonal and $a=b=c$.
- ◊ Therefore the angle α between two planes $(h_1k_1l_1)$ and $(h_2k_2l_2)$ is:

$$\alpha = \text{ArcCos}\left[\frac{h_1h_2 + k_1k_2 + l_1l_2}{\sqrt{(h_1^2 + k_1^2 + l_1^2)(h_2^2 + k_2^2 + l_2^2)}}\right]$$

THIS FORMULA, based on the vector dot product, IS ONLY TRUE FOR CUBIC SYSTEMS. In the next section, we will introduce the reciprocal lattice, which will allow us to use vector algebra to compute the angle between two planes in any crystallographic system.

As shown in Fig. 5.7, the $[uvw]$ zone has (hkl) planes whose normals σ_{hkl} are perpendicular to $[uvw]$. These normals lie in a plane whose intersection with the reference sphere forms a trace. Looking at the middle stereogram, locate the projection of the (111) pole. The (111) plane, which is perpendicular to this pole direction, intersects the reference sphere to form a trace whose projection is the great circle that intersects the projections of the poles whose planes belong to the $[111]$ zone. These include the $(1\bar{1}0)$, $(10\bar{1})$, $(01\bar{1})$, and $(\bar{1}10)$, which belong to the $[111]$ zone.

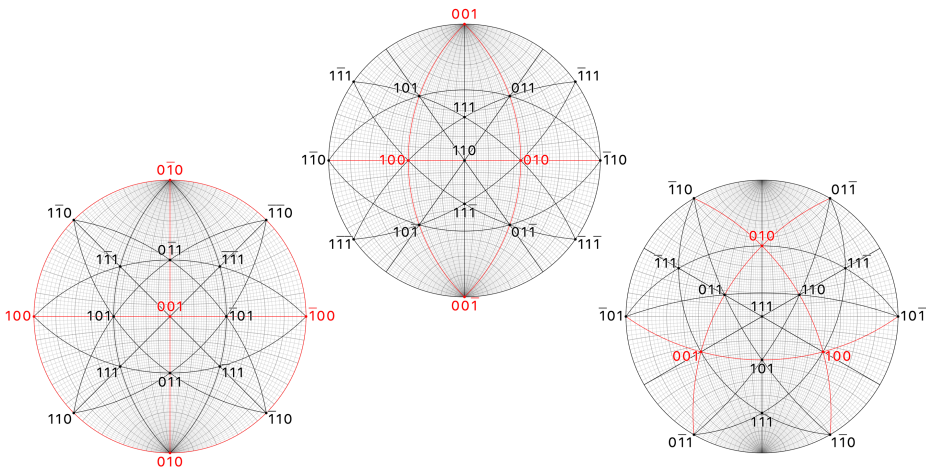


Figure 5.7: Standard (001) , (110) , and (111) projections of cubic crystal, generated by SingleCrystal Software. The lines in these stereographic projections represent zones whose hkl poles are mutually perpendicular to a $[uvw]$ zone axis. By inspection, locate the Zone Axes for each of the Zones. For example, on the leftmost stereogram, you can see that $[100]$ is the zone axis for the (010) , (011) , (001) , $(0\bar{1}1)$, and $(0\bar{1}0)$ planes.

5.4 Vector Representation of Periodic (hkl) Planes

In addition to describing the direction of an (hkl) crystal plane, we also need to describe the spatial periodicity of a set of planes in a given direction. This peri-

odicity will be referred to as the interplanar spacing or diffraction plane spacing, or **d-spacing**, (d_{hkl}). To do this, we will use vectors, where the vector direction is perpendicular to the set of (hkl) periodic planes, and the vector length is used to represent the d-spacing.

We can satisfy these two conditions for a set of (hkl) planes in a cubic system by defining a vector \bar{d}_{hkl}

with a direction [uvw] = [hkl]

and a length equal to the cubic d-spacing $d_{hkl} = \frac{a}{\sqrt{h^2+k^2+l^2}}$.

This is illustrated in Figure 5.8 for the cubic (110) and (220) planes.

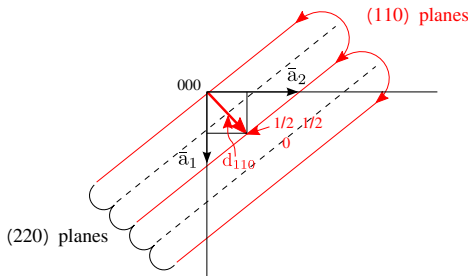


Figure 5.8: Edge-on view of (110) and (220) planes in a cubic system.

The magnitude of \bar{d}_{hkl} for the (110) and (220) planes:

$$d_{110} = \frac{a}{\sqrt{2}}$$

$$d_{220} = \frac{a}{2\sqrt{2}}$$

The direction of \bar{d}_{hkl} is $[hkl] = h\bar{a}_1 + k\bar{a}_2 + l\bar{a}_3$.

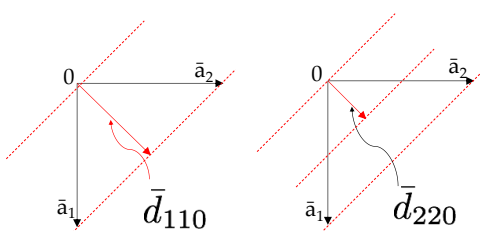


Figure 5.9: Defining vector \bar{d}_{hkl} for a cubic system.

Unfortunately, this scheme only works for cubic.

Try orthorhombic, $\alpha = \beta = \gamma = 90^\circ$

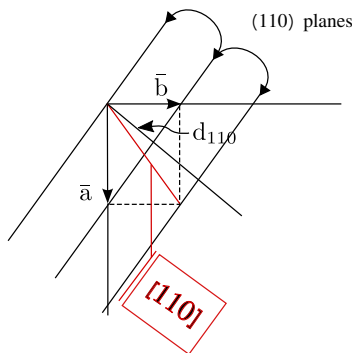


Figure 5.10: Orthorhombic example showing that the [110] direction is not perpendicular to the (110) planes.

For the orthorhombic case, the [110] vector is not perpendicular to the (110) planes. Therefore, the above definition of vector \bar{d}_{hkl} does not work in this case for defining the periodic (hkl) planes.

We need a vector representation of the (hkl) planes that works for all axial systems, not just cubic. This can be achieved in **reciprocal space**, where the spatial frequency of each set of hkl planes is represented by a reciprocal space vector. Note that just as temporal frequency has units of $1/(\text{sec})$, spatial frequency has units of $1/(\text{\AA})$.

5.5 Reciprocal Lattice Concept

Any (hkl) set of diffraction planes will be represented by a reciprocal lattice point whose coordinate is hkl , such that:

1. The vector \mathbf{r}^*_{hkl} , which starts at the origin 000 and ends at hkl , will be normal to the (hkl) planes.
2. The distance from the origin to hkl , $|\mathbf{r}^*_{hkl}| = 1/d_{hkl}$, where d_{hkl} is the interplanar spacing

Consider a monoclinic crystal with $a = 4\text{\AA}$, $b = 3\text{\AA}$, $c = 6\text{\AA}$, and $\gamma = 70^\circ$. Show the hkl reciprocal lattice points 000 , 100 , and 010 in relation to direct space axes \mathbf{a} and \mathbf{b} .

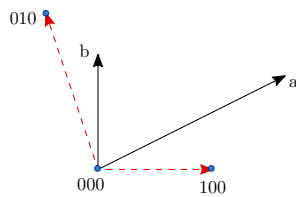


Figure 5.11: Reciprocal lattice points for a monoclinic crystal. The \bar{c} axis is perpendicular to the plane of the page. Note the placement of the reciprocal lattice origin 000 is arbitrary. The direction of \mathbf{r}^*_{100} that extends from 000 to 100 must be perpendicular to \mathbf{b} and \mathbf{c} , since by definition it is perpendicular to the (100) planes. While the length of \mathbf{r}^*_{100} is arbitrary, the ratio of the lengths is not arbitrary. In this case $\frac{r^*_{100}}{r^*_{010}} = \frac{b}{a}$.

Construct a $hk0$ reciprocal space lattice corresponding to the (hkl) planes belonging to the $[001]$ zone.

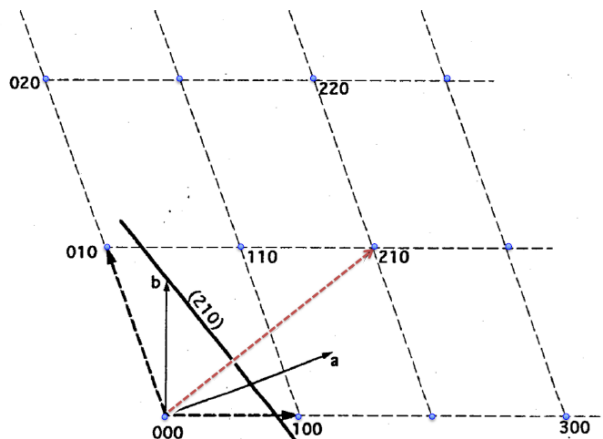


Figure 5.12: A portion of the $hk0$ reciprocal lattice in relation to direct space axes \mathbf{a} and \mathbf{b} . As prescribed, the red vector, \mathbf{r}^*_{210} , is perpendicular to the (210) plane.

The **reciprocal lattice**, which is a 3D vector representation of the direction and d-spacing of hkl periodic planes, works for any crystal system. As we will see later, a diffraction pattern from a crystal will be directly related to its reciprocal space lattice.

For any lattice in direct space defined by basis vectors $\bar{a}, \bar{b}, \bar{c}$, there is a set of reciprocal space axes $\bar{a}^*, \bar{b}^*, \bar{c}^*$, as shown in Figure 5.13, with directions and lengths determined by $\bar{a}, \bar{b}, \bar{c}$.

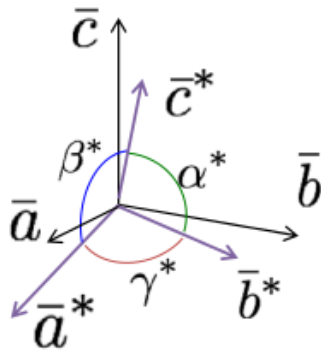


Figure 5.13: The reciprocal space axes in relation to the direct space axes that define them.

The following equations define the reciprocal space axes \mathbf{a}^* , \mathbf{b}^* , and \mathbf{c}^* for a given set of direct space axes \mathbf{a} , \mathbf{b} , and \mathbf{c} .

$$\bar{a}^* = \frac{\bar{b} \times \bar{c}}{\bar{a} \cdot (\bar{b} \times \bar{c})}$$

$$\bar{b}^* = \frac{\bar{c} \times \bar{a}}{\bar{b} \cdot (\bar{c} \times \bar{a})}$$

$$\bar{c}^* = \frac{\bar{a} \times \bar{b}}{\bar{c} \cdot (\bar{a} \times \bar{b})}$$

Note that:

- ◊ $\bar{a}^* \perp bc$ plane, $\bar{b}^* \perp ac$ plane, and $\bar{c}^* \perp ab$ plane
- ◊ $\bar{a}^* \cdot \bar{b} = 0$, $\bar{a}^* \cdot \bar{c} = 0$, $\bar{b}^* \cdot \bar{a} = 0$, $\bar{b}^* \cdot \bar{c} = 0$, $\bar{c}^* \cdot \bar{a} = 0$, $\bar{c}^* \cdot \bar{b} = 0$
- ◊ $\bar{a} \cdot (\bar{b} \times \bar{c}) = \bar{b} \cdot (\bar{c} \times \bar{a}) = \bar{c} \cdot (\bar{a} \times \bar{b}) = V$ = Volume of unit cell
- ◊ $\bar{a}^* \cdot \bar{a} = 1$, $\bar{b}^* \cdot \bar{b} = 1$, $\bar{c}^* \cdot \bar{c} = 1$ Reciprocal Relationship

Special Case: $\alpha = \beta = 90^\circ$

For $\alpha = \beta = 90^\circ$ (i.e., all but triclinic or rhombohedral)

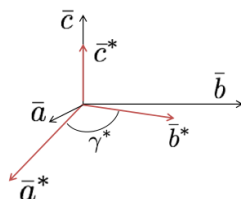


Figure 5.14: Special Case ($\alpha = \beta = 90^\circ$)

$$\bar{c}^* \parallel \bar{c}$$

$$\gamma^* = 180^\circ - \gamma$$

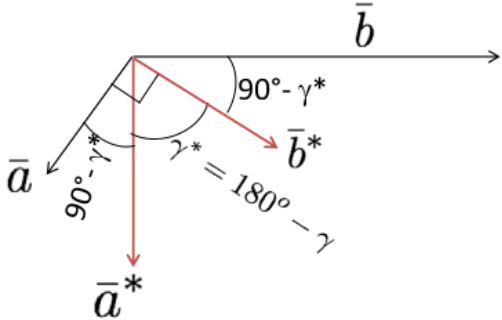


Figure 5.15: Special Case ($\alpha = \beta = 90^\circ$)

$$\gamma = 90^\circ - \gamma^* + 90^\circ - \gamma^* + \gamma^*$$

$$\gamma = 180^\circ - \gamma^*$$

5.5.1 Cartesian axial system

For $\alpha = \beta = \gamma = 90^\circ \rightarrow$ Cartesian axial system. Namely, Cubic, tetragonal, or orthorhombic

$$\bar{a}^* \parallel \bar{a}, \bar{b}^* \parallel \bar{b}, \bar{c}^* \parallel \bar{c}$$

And...

$$|\bar{b} \times \bar{c}| = bc$$

$$|\bar{a} \cdot \bar{b} \times \bar{c}| = abc = V$$

$$|\bar{a}^*| = \left| \frac{\bar{b} \times \bar{c}}{\bar{a} \cdot \bar{b} \times \bar{c}} \right| = \frac{bc}{abc} = \frac{1}{a}$$

$$a^* = \frac{1}{a}, \quad b^* = \frac{1}{b}, \quad c^* = \frac{1}{c}$$

...hence “reciprocal.”

5.6 Use of Reciprocal Lattice Vectors

The reciprocal lattice vector extends in reciprocal space from the origin 000 to the reciprocal lattice point hkl and is perpendicular to the corresponding (hkl) planes. The set of all such hkl points corresponds to the reciprocal lattice. These vectors have units of $1/\text{length}$, so a larger vector indicates smaller spacing between planes.

$$\mathbf{r}^*_{hkl} = h\bar{a}^* + k\bar{b}^* + l\bar{c}^*$$

Note: Hammond - $\mathbf{r}^*_{hkl} = \mathbf{d}^*_{hkl}$ Cullity - $\mathbf{r}^*_{hkl} = \mathbf{H}_{hkl}$

The following examples show applications of reciprocal lattice vectors in determining inter-planar relationships.

- Find the inter-planar angle ϕ between planes $(h_1k_1l_1)$ and $(h_2k_2l_2)$

i.e., find the angle between reciprocal lattice vectors \vec{r}_1^* and \vec{r}_2^* .

$$\cos(\phi) = \frac{\vec{r}_1^* \cdot \vec{r}_2^*}{r_1^* r_2^*}, \text{ where } r_n^* = |\vec{r}_n^*| = \sqrt{\vec{r}_n^* \cdot \vec{r}_n^*}$$

$$\vec{r}_1^* \cdot \vec{r}_2^* = (h_1\bar{a}^* + k_1\bar{b}^* + l_1\bar{c}^*) \cdot (h_2\bar{a}^* + k_2\bar{b}^* + l_2\bar{c}^*)$$

$$= h_1h_2a^{*2} + k_1k_2b^{*2} + l_1l_2c^{*2} + (h_1k_2 + k_1h_2)\bar{a}^* \cdot \bar{b}^* + (h_1l_2 + l_1h_2)\bar{a}^* \cdot \bar{c}^* + (k_1l_2 + l_1k_2)\bar{b}^* \cdot \bar{c}^*$$

Note: $\bar{a}^* \cdot \bar{b}^* = a^*b^* \cos(\gamma^*)$, etc.

Example: Find the angle between (111) and (110) in the cube.

$$\cos(\phi) = \frac{\vec{r}_{111}^* \cdot \vec{r}_{110}^*}{r_{111}^* r_{110}^*} = \frac{(1+1+0)a^{*2}}{\sqrt{3}a^*\sqrt{2}a^*} = \frac{2}{\sqrt{6}} \Rightarrow \phi = 35.26^\circ$$

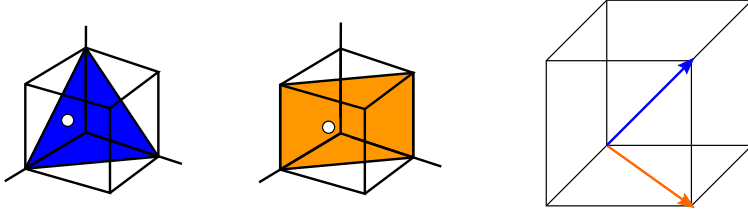


Figure 5.16: Angle between (111) and (110) in cubic unit cell.

- Find the zone axis for two intersecting planes $(h_1k_1l_1)$ and $(h_2k_2l_2)$.

Miller indices: If you need a refresher on Miller indices, the Wikipedia page (https://en.wikipedia.org/wiki/Miller_index) is very helpful. Here, we include a reminder of the notation used to indicate planes and directions.

- ◊ **Specific planes:** We use round brackets - (hkl)
- ◊ **Class of planes:** To indicate all planes that are crystallographically identical, we use curly brackets - $\{hkl\}$
- ◊ **Specific direction:** We use square brackets - $[hkl]$
- ◊ **Class of directions:** To indicate all directions that are crystallographically identical, we use angle brackets - $\langle hkl \rangle$

$$\bar{z} = [uvw] = u\bar{a} + v\bar{b} + w\bar{c}$$

Since $\bar{r}_{hkl}^* \perp (hkl)$ plane, $\bar{r}_{hkl}^* \perp \bar{z}$ for any (hkl) belonging to the zone \bar{z}

$$\bar{z} \cdot \bar{r}_1^* = uh_1 + vk_1 + wl_1 = 0$$

$$\bar{z} \cdot \bar{r}_2^* = uh_2 + vk_2 + wl_2 = 0$$

Solve simultaneous equations for u, v, w

$$u = k_1 l_2 - l_1 k_2$$

$$v = l_1 h_2 - h_1 l_2$$

$$w = h_1 k_2 - k_1 h_2$$

2 equations and 3 unknowns \rightarrow uvw determined to within a scale factor

Example: What is the zone axis (or edge formed by) for $(\bar{1}10)$ and (010) ?

$$u = (1)(0) - (0)(1) = 0$$

$$v = (0)(0) - (-1)(0) = 0$$

$$w = (-1)(1) - (1)(0) = -1$$

$$\bar{z} = [uvw] = [00\bar{1}] \text{ or } [001] = \bar{c}-\text{axis}$$

Equivalent to doing vector cross-product:

$$\bar{r}_{\bar{1}10}^* \times \bar{r}_{010}^*$$

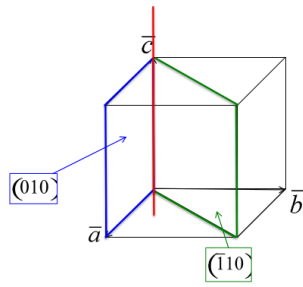


Figure 5.17: Zone axis for $(\bar{1}10)$ & (010)

3. Find d-spacing d_{hkl}

Use $|\bar{r}_{hkl}^*| = r_{hkl}^* = \frac{1}{d_{hkl}}$

$d_{hkl} = \perp$ distance between 2 \parallel planes with intercept differences = $\frac{a}{h}, \frac{b}{k}, \frac{c}{l}$

$$r_{hkl}^* = \sqrt{\bar{r}_{hkl}^* \cdot \bar{r}_{hkl}^*}$$

$$r_{hkl}^{*2} = h^2a^{*2} + k^2b^{*2} + l^2c^{*2} + 2hk\bar{a}^* \cdot \bar{b}^* + 2hl\bar{a}^* \cdot \bar{c}^* + 2kl\bar{b}^* \cdot \bar{c}^*$$

For $\alpha = \beta = \gamma = 90^\circ$, $\bar{a}^* \cdot \bar{b}^* = \bar{a}^* \cdot \bar{c}^* = \bar{b}^* \cdot \bar{c}^* = 0$

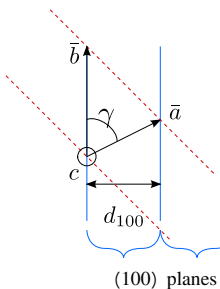


Figure 5.18: d_{100} spacing

Note: $\bar{a}^* \cdot \bar{b}^* = a^*b^* \cos(\gamma^*)$

$$\text{For Orthorhombic - } d_{hkl} = \frac{1}{r_{hkl}*} = \frac{1}{(\frac{h^2}{a^2} + \frac{k^2}{b^2} + \frac{l^2}{c^2})^{1/2}}$$

$$\text{For Cubic - } d_{hkl} = \frac{a}{(h^2+k^2+l^2)}$$

Monoclinic

$$(\alpha = \beta = 90^\circ) \quad a = 4\text{\AA}, \quad b = 3\text{\AA}, \quad c = 6\text{\AA}, \quad \gamma = 70^\circ$$

$$r_{100}^* = a^* = \frac{1}{d_{100}} \neq \frac{1}{4\text{\AA}} \quad d_{100} = a^{*-1} \quad a^* = ? \neq \frac{1}{a} \text{ since } \gamma \neq 90^\circ$$

$$\text{Use } \bar{a}^* \cdot a = 1 \rightarrow a \cdot a \cos(\frac{\pi}{2} - \gamma) = 1$$

$$a^* = \frac{1}{a \sin(\gamma)} = \frac{0.250}{0.94} = 0.266\text{\AA}^{-1} \quad \therefore d_{100} = a \sin(\gamma) = 3.759\text{\AA} \neq 4\text{\AA}$$

$$\text{Likewise, } b^* = \frac{1}{b \sin(\gamma)} = \frac{0.333}{0.94} = 0.355\text{\AA}^{-1} \quad \therefore d_{010} = b \sin(\gamma) = 2.819\text{\AA}.$$

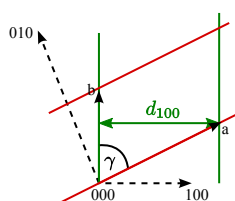


Figure 5.19: Monoclinic d_{100} spacing. The green lines are an edge-on view of the (100) planes. The red lines are for the (010) planes.

Note: For monoclinic, $\frac{a^*}{b^*} = \frac{b}{a}$ $c^* = \frac{1}{c} = \frac{1}{6}\text{\AA}^{-1}$ since $\bar{c} \parallel \bar{c}^*$

4. For every Direct Space Lattice, there is a uniquely defined Reciprocal Space Lattice.

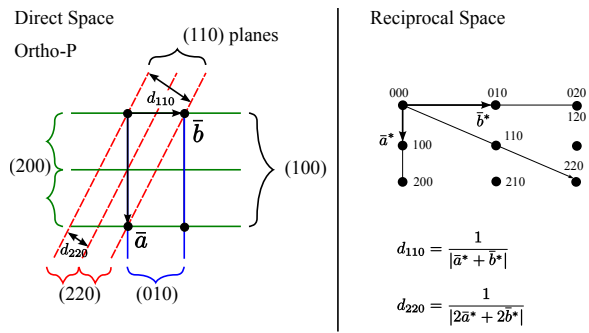


Figure 5.20: Direct vs Reciprocal Space for Ortho-P. Both lattices are Ortho-P with an inverted aspect ratio. Namely, $\frac{a^*}{b^*} = \frac{b}{a}$.

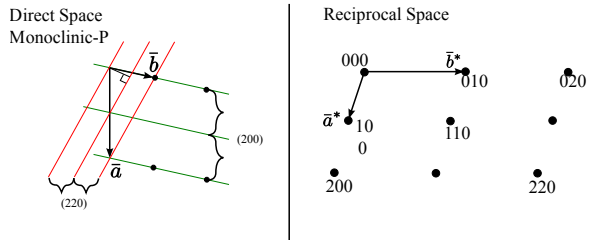


Figure 5.21: Direct vs. Reciprocal Space for Monoclinic-P. Both are Monoclinic-P with $\frac{a^*}{b^*} = \frac{b}{a}$.

5. Cell axis transformations (primitive \rightarrow non-primitive)

e.g. Rhombohedral ($\alpha = \beta = \gamma = 60^\circ$) \rightarrow FCC

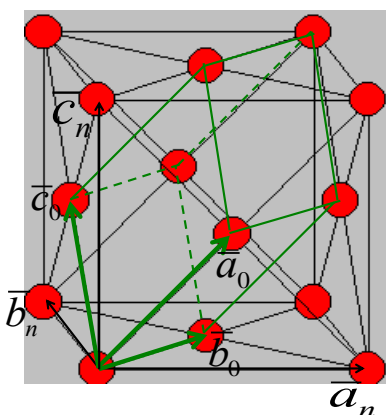


Figure 5.22: FCC lattice with outlined in green rhombohedral-P unit cell axes \bar{a}_0 , \bar{b}_0 , and \bar{c}_0 .

Let the old rhombohedral unit cell axes be $\bar{a}_0, \bar{b}_0, \bar{c}_0$

The new FCC unit cell axes $\bar{a}_n, \bar{b}_n, \bar{c}_n$ are related to the old by the following three linear equations:

$$\bar{a}_n = u_1 \bar{a}_0 + v_1 \bar{b}_0 + w_1 \bar{c}_0$$

$$\bar{b}_n = u_2 \bar{a}_0 + v_2 \bar{b}_0 + w_2 \bar{c}_0$$

$$\bar{c}_n = u_3 \bar{a}_0 + v_3 \bar{b}_0 + w_3 \bar{c}_0$$

In matrix form, this is written as:

$$\begin{pmatrix} \bar{a}_n \\ \bar{b}_n \\ \bar{c}_n \end{pmatrix} = \begin{pmatrix} u_1 & v_1 & w_1 \\ u_2 & v_2 & w_2 \\ u_3 & v_3 & w_3 \end{pmatrix} \begin{pmatrix} \bar{a}_0 \\ \bar{b}_0 \\ \bar{c}_0 \end{pmatrix}$$

Matrix of transformation

By inspection of Fig. 5.22, we see that the FCC basis vectors are linear combinations of the rhombohedral basis vectors as follows:

$$\bar{a}_n = \bar{a}_0 + \bar{b}_0 - \bar{c}_0$$

$$\bar{b}_n = -\bar{a}_0 + \bar{b}_0 + \bar{c}_0$$

$$\bar{c}_n = \bar{a}_0 - \bar{b}_0 + \bar{c}_0$$

Transformation Matrix: $\begin{pmatrix} 1 & 1 & -1 \\ -1 & 1 & 1 \\ 1 & -1 & 1 \end{pmatrix}$

The Determinant of this transformation matrix is

$$\begin{vmatrix} 1 & 1 & -1 \\ -1 & 1 & 1 \\ 1 & -1 & 1 \end{vmatrix} = 4 \rightarrow V_n = 4V_0$$

The determinant value corresponds to the fact that the FCC non-primitive unit cell has 4 lattice points per unit cell and, therefore, has four times the volume of the rhombohedral unit cell.

We can also use this formalism for transforming $(h_0 k_0 l_0) \leftrightarrow (h_n k_n l_n)$.

Since the inter-planar spacing and direction are the same, a particular set of planes will have equivalent reciprocal lattice vectors: $\bar{r}_{h_0 k_0 l_0}^* = \bar{r}_{h_n k_n l_n}^*$.

$$h_0 \bar{a}_0^* + k_0 \bar{b}_0^* + l_0 \bar{c}_0^* = h_n \bar{a}_n^* + k_0 \bar{b}_n^* + l_n \bar{c}_n^*$$

take dot product with $\bar{a}_n = u_1 \bar{a}_0 + v_1 \bar{b}_0 + w_1 \bar{c}_0$

$$(u_1 \bar{a}_0 + v_1 \bar{b}_0 + w_1 \bar{c}_0) \cdot (h_n \bar{a}_n^* + k_0 \bar{b}_n^* + l_n \bar{c}_n^*) = h_n$$

$$\begin{aligned} h_n &= u_1 h_0 + v_1 k_0 + w_1 l_0 \\ k_n &= u_2 h_0 + v_2 k_0 + w_2 l_0 \\ l_n &= u_3 h_0 + v_3 k_0 + w_3 l_0 \end{aligned} \rightarrow \begin{pmatrix} h_n \\ k_n \\ l_n \end{pmatrix} = \begin{pmatrix} u_1 & v_1 & w_1 \\ u_2 & v_2 & w_2 \\ u_3 & v_3 & w_3 \end{pmatrix} \begin{pmatrix} h_0 \\ k_0 \\ l_0 \end{pmatrix}$$

Therefore, the same transformation matrix that was used for the axes is also used for the indices.

Old Rhombohedral \rightarrow New FCC example

$$\begin{pmatrix} h_n \\ k_n \\ l_n \end{pmatrix} = \begin{pmatrix} 1 & 1 & -1 \\ -1 & 1 & 1 \\ 1 & -1 & 1 \end{pmatrix} \begin{pmatrix} h_0 \\ k_0 \\ l_0 \end{pmatrix}$$

$$\begin{aligned} h_n &= h_0 + k_0 - l_0 \\ k_n &= -h_0 + k_0 + l_0 \\ l_n &= h_0 - k_0 + l_0 \end{aligned}$$

Note that $h_n + k_n = 2k_0$, is an even integer and $k_n + l_n = 2l_0$, is also an even integer.

Therefore, h_n, k_n, l_n must all be even or must all be odd integers. i.e., FCC reciprocal lattice points have "unmixed" hkl Miller indices.

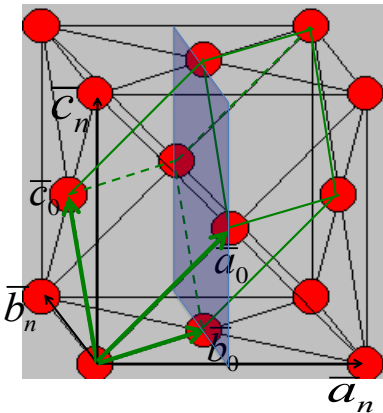


Figure 5.23: Rhombohedral indexed (110) plane in an FCC lattice.

Let's put this transformation matrix to work on the purple plane drawn in Fig. 5.23. Based on the plane's intercepts with the rhombohedral axes, $(h_0 k_0 l_0) = (110)$. Transformation of the (110) plane in the rhombohedral structure to its (hkl) in the face-centered cubic structure.

$$(110)_R = (???)_{FCC} \rightarrow \begin{pmatrix} h_n \\ k_n \\ l_n \end{pmatrix} = \begin{pmatrix} 1 & 1 & -1 \\ -1 & 1 & 1 \\ 1 & -1 & 1 \end{pmatrix} \begin{pmatrix} 1 \\ 1 \\ 0 \end{pmatrix} = (200)$$

This checks out, since the plane intercepts the FCC **a**-axis at $\frac{1}{2}$ and is parallel to both the **b** and **c** axes.

In Figure 5.24 below, a non-primitive orthorhombic-C unit cell is illustrated, with the **c**-axis pointing out of the page. The transformation of its lattice from direct space to reciprocal space is shown in Figure 5.25. Notice that the \mathbf{a}^* and \mathbf{b}^* axes only reach halfway to the first lattice point in their respective directions. This is due to the organization of lattice planes in the **a** and **b** directions of the direct space. For instance, going vertically in the **a** direction of Figure 5.24, the first set of planes appears halfway between the lattice spacing. The planes that follow in this **a** direction appear at the same spacing. Thus, this set of (200) planes within the Orthorhombic-C unit cell can represent the fundamental period of planes in the **a** direction. The same analysis can be done in the **b** direction, yielding the (020) fundamental period of planes. From this, the first point in the reciprocal space appears at 200 in the \vec{a}^* direction and 020 in the \vec{b}^* direction. Note that in the **c** direction, which is not shown, the first plane is found at (001), due to the base-centered structure.

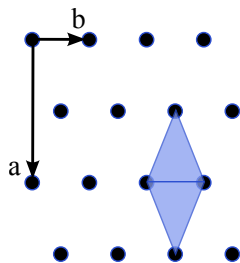


Figure 5.24: Orthorhombic-C

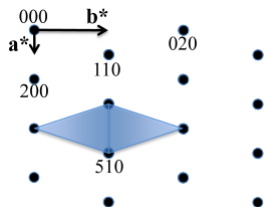


Figure 5.25: Reciprocal Lattice $l=0$ layer

Note that the original, direct space lattice and the reciprocal space lattice have a similar shape, with an inverted aspect ratio in the reciprocal lattice. Furthermore, they are both base-centered and have a similar primitive unit cell, which is monoclinic. The missing base-centered reciprocal lattice points (e.g., 010, 100, 210, etc.) result from using a non-primitive unit cell in direct space for the transformation. Had the primitive cell been used, all allowed reciprocal lattice points, corresponding to allowed (hkl) Bragg diffraction planes, would be present. Anytime a non-primitive unit cell is used to describe the lattice, there will be missing hkl reciprocal lattice points.

A c-axis projection of the FCC unit cell showing the **a** and **b** axes is illustrated in Figure 5.26 below. The filled circles represent the lattice points in the plane of the paper, and the open circles with the $\frac{1}{2}$ label represent lattice points half a lattice

spacing above the plane. The dashed lines indicate the set of (110) planes within this unit cell. The transformation from the FCC direct space lattice to reciprocal space generates a BCC lattice, as shown in Figure 5.27, and vice versa. Note that the (100) planes are missing since the fundamental period of planes is (200) in the a direction. This reasoning can be applied to other missing reciprocal space points, using the fundamental period of planes in the direct space FCC lattice.

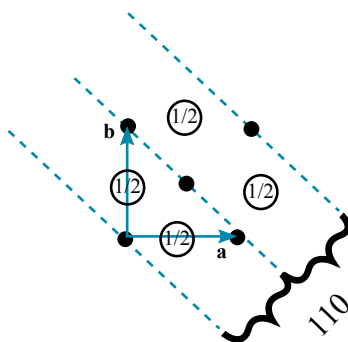


Figure 5.26: FCC unit cell lattice points

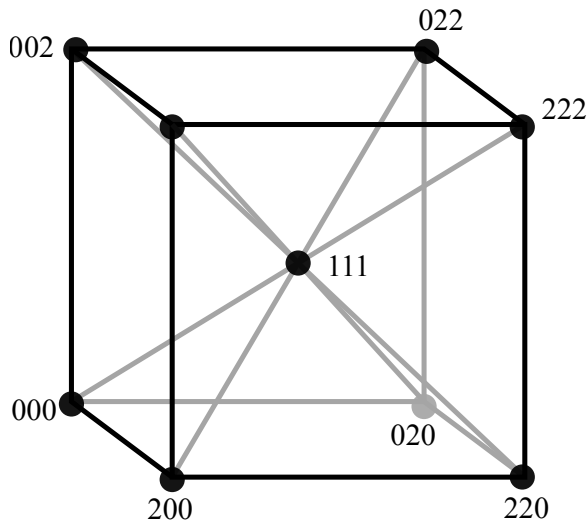


Figure 5.27: Reciprocal Lattice - hkl unmixed (all even or all odd)

6 Representative Crystal Structures

When discussing 2D symmetry in Chapter 4, we found that the 5 plane lattices can be combined with point symmetry operators (plus glide) to produce a total of 17 plane groups. Perhaps more to the point, any 2D periodic pattern found or produced in our universe can be described by one of these 17 plane groups. In 3D, there are 14 Bravais lattices that, when combined with the 32 point symmetry groups, can only produce a list of 230 possible space groups from which all 3D crystals can be described.

6.1 Crystal Structure Examples

For 3D crystal structures, an identical atom or a fixed arrangement of atoms (ions, molecules) is found at each Bravais lattice point. This could be 1000's of atoms, such as in a protein crystal. We will start simple with one or two atoms per lattice point.

For the case of one atom per lattice point, we can look at the simple metal crystal structures of body-centered cubic (BCC) (space group: $I\bar{m}\bar{3}m$) shown in Fig. 6.1 and face-centered cubic (FCC) (space group: $Fm\bar{3}m$) shown in Fig. 6.2. One can find the crystal structures for each element online at www.webelements.com. There, you will find that solid argon is also FCC and that polonium (Po) is the only element with a cubic-P crystal structure $Pm\bar{3}m$.

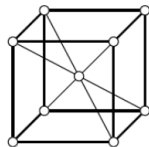


Figure 6.1: Body-centered cubic (BCC or cubic-I) crystal structure with one atom per lattice point. Examples of BCC metals include: α -Fe, Cr, Mo, V, and W. The number of nearest neighbors or coordination number CN = 8.

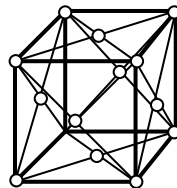


Figure 6.2: Face-centered cubic (FCC or cubic-F) crystal structure with one atom per lattice point. Examples of FCC metals include: γ -Fe, Cu, Pb, Ni, Au, Pt, and Ag. CN = 12.

Unlike the examples in Figures 6.1 and 6.2, the hexagonal close-packed structure has two identical atoms per lattice point. These two atoms are considered to be the motif or repeating object within the hexagonal-P lattice.

Figure 6.3 shows four different representations of a hexagonal close-packed structure with two hexagonal close-packed structure atoms per unit cell - one atom at 000 and one atom at $\frac{2}{3}\frac{1}{3}\frac{1}{2}$ or $\frac{1}{3}\frac{2}{3}\frac{1}{2}$. The atoms in Figure 6.3(b) correspond to the nine atoms illustrated in Figure 6.3(a). The association of two atoms with a single lattice point is represented by the dashed lines connecting the pairs. Furthermore, (c) and (d) show more of a hexagonal representation of the HCP atomic structure with the stacking of atomic planes in a periodic arrangement.

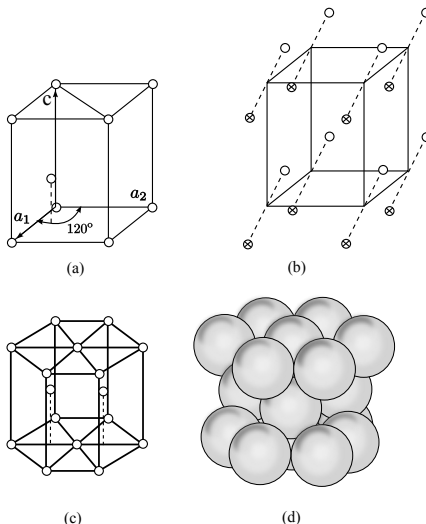


Figure 6.3: Hexagonal close-packed (HCP) crystal structure (Space Group $P6_3/mmc$) with two identical atoms per hexagonal-P lattice site. Examples of HCP metals include: Zn, Mg, Zr, Ti, and Be. CN = 12.

The FCC crystal structure is as close-packed as the HCP structure, though its relation to the HCP structure is not immediately apparent. Figure 6.4 demonstrates the stacking of FCC (111) planes in a hexagonal pattern, similar to the (0002) HCP planes stacking. One distinction between the two is that the HCP layer stacking occurs in an ABAB pattern in the \bar{c} or [001] direction, and the layer stacking for FCC occurs in an ABCABC pattern in the [111] directions. This is illustrated in Figures 6.5 and 6.7 below.

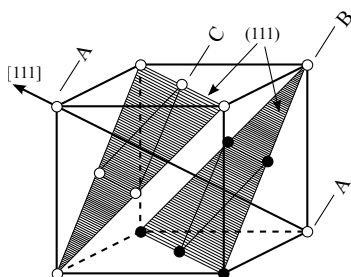


Figure 6.4: Face-centered cubic (111) planes.

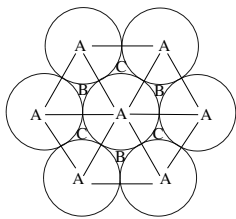


Figure 6.5: Stacking of (111) planes in FCC.

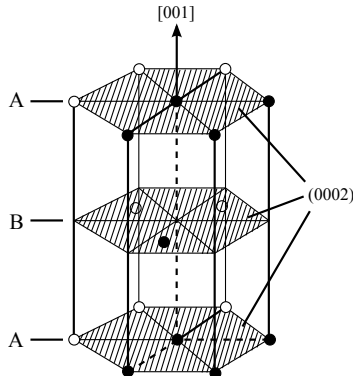


Figure 6.6: Hexagonal close-packed planes.

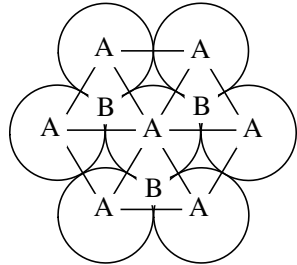


Figure 6.7: Stacking of (0002) planes in HCP.

There are other examples of crystal structures with two atoms per lattice point. The first example, shown in Figure 6.8, is the diamond crystal structure seen in other atoms besides carbon, such as silicon and germanium. In the examples following Figure 6.8, compounds consisting of two unlike atoms follow unique arrangement characteristics. For instance, if a compound's structure consists of atoms A and B, the structure of A atoms must possess the same symmetry elements of the crystal as a whole. Namely, a symmetry operation characteristic of the entire crystal, when performed on a given A atom, must bring it into coincidence with another A atom. Furthermore, body-centering, face-centering, and base-centering translations, if present, should begin and end on like atoms. An example of this is detailed above in Figure 6.11.

Diamond Structure

Example: C, Si, Ge

4 C atoms at 000 + face-center translations (fct)

4 C at $\frac{1}{4}\frac{1}{4}\frac{1}{4}$ + fct

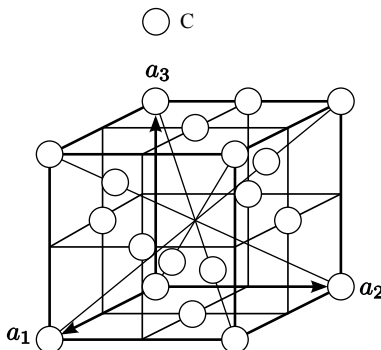


Figure 6.8: The Diamond crystal structure (Space Group $Fd\bar{3}m$) has an atom at each FCC lattice site plus a second same type atom displaced by $\frac{1}{4}\frac{1}{4}\frac{1}{4}$ from each FCC lattice site.

Zinc Blend

The face-centered cubic zinc blend structure in Fig. 6.9 can be likened to the diamond structure in Figure 6.8 above, but the atoms at 000+fct (S) are now different from those at the second set of positions - $\frac{1}{4}\frac{1}{4}\frac{1}{4}$ + fct (Zn).

Example: GaAs, ZnS

4 S at 000+fct

4 Zn at $\frac{1}{4}\frac{1}{4}\frac{1}{4}$ + fct

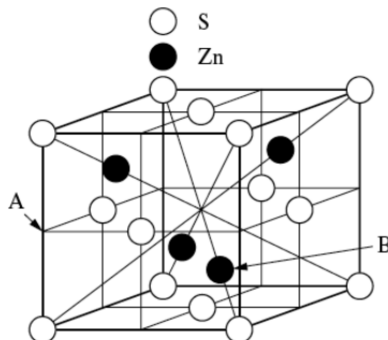


Figure 6.9: The Zinc Blend crystal structure (Space Group $F\bar{4}3m$) has an atom at each FCC lattice site plus a second different type of atom displaced by $\frac{1}{4}\frac{1}{4}\frac{1}{4}$ from each FCC lattice site.

The **CsCl structure** illustrated in Figure 6.10 below is common to compounds such as CsBr, NiAl, ordered β -brass, and ordered CuPd. Though it appears to be a body-centered cubic structure at first glance, the body-centering translation $\frac{1}{2}\frac{1}{2}\frac{1}{2}$ connects two unlike atoms rather than the required self-coincidence of a single atomic element. Therefore, the structure is simple cubic (Cubic-P), and one may think of the Cs^+ cation at 000 and the Cl^- anion at $\frac{1}{2}\frac{1}{2}\frac{1}{2}$ as being related to the single lattice point at 000.

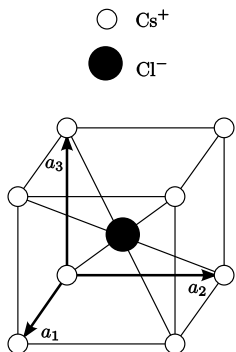


Figure 6.10: CsCl structure (Space Group $Pm\bar{3}m$) is Cubic-P

In the NaCl or rock salt crystal structure of Figure 6.11 below, the sodium cations are at FCC sites. When face-centering translations are applied to the chlorine anions $(\frac{1}{2}\frac{1}{2}\frac{1}{2})$, all chlorine atom positions are mapped. In addition, a 90° rotation about the fourfold rotation axis at [010] brings the chlorine atoms into self-coincidence.

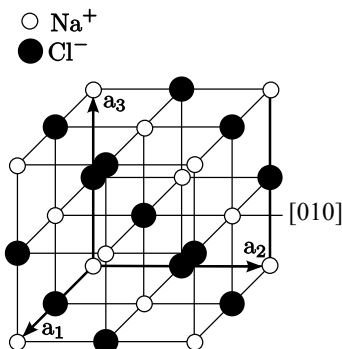


Figure 6.11: NaCl (common to KCl, CaSe, PbTe,etc.)

6.2 Voids in FCC

The simple metal FCC structure shown in Fig. 6.2 has two types of voids: octahedral and tetrahedral voids that naturally arise from the arrangement of atoms in its crystal lattice.

Octahedral voids are located at $\frac{1}{2}\frac{1}{2}\frac{1}{2} + fct$ in the FCC structure. There is one located at the center of the unit cell and one at the center of each of the unit cell

edges. Since there are twelve edges and each edge is shared with four other unit cells, this yields three edge octahedral voids per unit cell, in addition to the one at the center. Thus, there are a total of four octahedral voids per unit cell. The space labeled “A” in Figure 6.12 is an octahedral hole in the structure, which is surrounded by 6 sulfur atoms. In Figure 6.11, note that Cl^- in NaCl is octahedrally surrounded by Na^+ .

The Zn atom at $\frac{3}{4} \frac{3}{4} \frac{1}{4}$, marked “B” in Figure 6.12, is surrounded by four S atoms at the corners of a tetrahedron. This is known as a **tetrahedral void** in the structure, as the Zn atom is surrounded by a tetrahedral structure of sulfur atoms. In the zinc blend structure, as well as in other FCC-structured crystals, there are a total of eight tetrahedral voids per unit cell. For the zinc blend structure, however, only half of these tetrahedral sites are occupied by Zn atoms, which is illustrated more clearly in Figure 6.9.

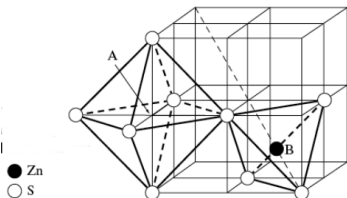


Figure 6.12: Portion of the zinc blend structure

6.3 Atomic Sizes and Coordination

When picturing atoms within a crystal structure, atoms in ionic or metallic crystals have non-directional bonding and can be represented by a simplified hard sphere structure, with atomic spheres in direct contact with one another. For a monoatomic metal, the maximized packing of equal-sized spheres leads to close-packing HCP or FCC with CN=12. For an AB ionic compound crystal, the packing of two different-sized spheres of opposite charge leads to CN = 8, 6, or 4, depending on the disparity of the spherical sizes. This number of nearest neighbors (coordination number or CN) is specific to a given crystal structure. The radius of a given atomic element is generally considered to be constant regardless of conditions such as phase or presence in a solution. The size of an atom may also be deduced from its **coordination number** (CN), or number of nearest neighbors specific to its crystal structure. The Cs and Cl atoms in the simple cubic structure, for instance, have a coordination number of 8, as shown below. Ex.: CsCl

Structure - Cubic P (not BCC)

Cs^+ at 000 \rightarrow CN=8

Cl^- at $\frac{1}{2} \frac{1}{2} \frac{1}{2}$ \rightarrow CN=8

○ Cs⁺

● Cl⁻

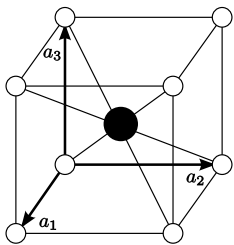


Figure 6.13: CsCl

Using the hard sphere model for atoms, along with the placement of atoms in the unit cell of a given structure and known atomic radii, the lattice constant of a crystal structure may be determined. The following procedure demonstrates the evaluation of the lattice constant “*a*” in CsCl using known ionic radii:

$$r_{Cs^+} = 1.69 \text{ \AA} \quad r_{Cl^-} = 1.81 \text{ \AA}$$

The body diagonal of a cube = $\sqrt{3}a = 2r_{Cs^+} + 2r_{Cl^-}$

$$\text{and therefore } a = \frac{2}{\sqrt{3}}(r_{Cs^+} + r_{Cl^-}) = 4.04 \text{ \AA}.$$

Note that the nearest neighbors experience an attractive force due to their opposite charges, and the second-nearest neighbors experience a repulsive force due to their like charges. Therefore, if the two ionic sizes become more disparate than those of CsCl, then the packing changes to a NaCl structure. NaCl structure:

4 Na⁺ at 000 + fct CN=6 (octahedral surroundings)

4 Cl⁻ at $\frac{1}{2}\frac{1}{2}\frac{1}{2}$ + fct CN=6 (octahedral surroundings)

fct \equiv face-center translations $\equiv \{(000), (\frac{1}{2}\frac{1}{2}0), (\frac{1}{2}0\frac{1}{2}), (0\frac{1}{2}\frac{1}{2})\}$

$$r_{Na^+} = 0.95 \text{ \AA} \quad r_{Cl^-} = 1.81 \text{ \AA}$$

If the NaCl structure were like “CsCl” structure,

$$\text{then } a = \frac{2}{\sqrt{3}}(r_{Na^+} + r_{Cl^-}) = 3.19 \text{ \AA}$$

Therefore, the NaCl CN=8 structure would not bond since the Cl⁻-Cl⁻ distance $a = 3.19 \text{ \AA} < 2r_{Cl^-} = 3.62 \text{ \AA}$

In other words, for the CN=8 CsCl structure, the distance of the required lattice parameter would be greater than the available distance of two radii of the larger ions that make up the lattice parameter “*a*”. Thus, there is a critical or minimum radius ratio for which cation-anion contact is established in the CsCl structure.

$a > 2r_>$, where $r_>$ = radius of larger ion & $r_<$ = radius of smaller ion

$$\therefore \text{Limit } a = 2r_> \rightarrow \frac{2}{\sqrt{3}}(r_< + r_>) = 2r_>$$

$$\text{Radius Ratio} \equiv \frac{r_<}{r_>} = \sqrt{3} - 1 = 0.732$$

This radius ratio rule is different for various crystal structures, as shown in Table 7 below. Deviation from the radius ratio rule indicates a shift from ionic to covalent bonding. Ex. Zinc blend structure: $r_{Zn^{2+}} = 0.6\text{\AA}$ $r_{S^{2-}} = 1.80\text{\AA} \rightarrow \frac{r_-}{r_>} < 0.33$

Crystal Structure	CN	Radius Ratio Rule	Example
CsCl	8	$0.732 < \frac{r_-}{r_>} < 1$	CsCl, CsBr
NaCl	6	$0.414 < \frac{r_-}{r_>} < 0.732$	KCl, NaCl
Wurtzite or Zinc Blend	4	$\frac{r_-}{r_>} < 0.414$	ZnS, GaAs

Table 7: Radius Ratio Rules

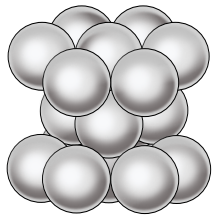


Figure 6.14: Close-packed structure

What about HCP and FCC close-packed structures? For the HCP structures, the coordination number is 12. An ionic crystal cannot have this coordination number because there would be an equal number of anions and cations surrounding each ion.

7 Introduction to Diffraction

Since the early 20th century, the experimental method of X-ray diffraction from crystals has played a crucial role in determining crystal structures. This section will outline the essential concepts of X-ray diffraction, including the properties of X-rays and Braggs' Law.

7.1 X-ray

An **X-ray** is an electromagnetic wave, similar to light, but of a much shorter wavelength. As illustrated in Figure 7.1 below, an X-ray plane wave with wavelength λ traveling in direction (i.e., \vec{k}) has an electric field (\vec{E}) perpendicular to its propagation direction and a magnetic field (\vec{H}) perpendicular to its electric field. A plane wave has a constant phase within a plane perpendicular to the propagation direction, labeled as the Poynting vector \mathbf{S} in Figure 7.1. The magnetic field will be ignored within this text because it has a much weaker interaction with matter.

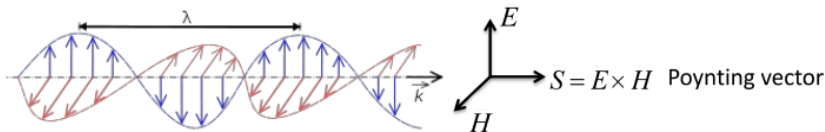


Figure 7.1: Frozen-in-time electromagnetic wave with oscillating E-field perpendicular to magnetic field.

The following equation models the oscillation of the electric field in space and time as a transverse plane wave traveling in the x-direction, with an amplitude of \bar{E}_0 that has the E-field \bar{E} polarized in the y-direction:

$$\bar{E} = \bar{E}_0 \cos\left[\frac{2\pi}{\lambda}(x - vt)\right], \text{ where } \lambda = \text{wavelength}, v = \text{velocity traveling in x-direction}$$

$$\text{Let } \bar{E}_0 = E_0 \hat{j}$$

After a time, t has elapsed, the wave has been phase shifted to the right by $x' = vt$.

7.2 Interference

Interference occurs when two or more **coherent**, or same wavelength, waves are superimposed. If two interfering waves are in phase, then constructive interference occurs, as illustrated in Figure 7.2. The superposition of two identical traveling waves that are out of phase, as shown in Figure 7.3, produces a null vector.

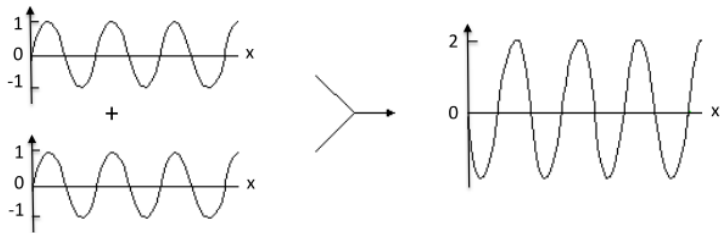


Figure 7.2: Constructive interference between 2 identical traveling waves that are perfectly in-phase.

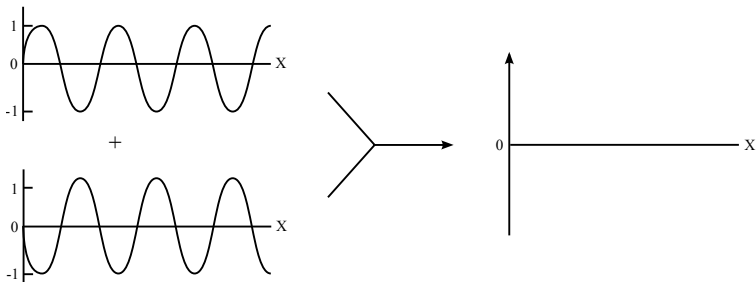


Figure 7.3: Complete destructive interference occurs by the superposition of two identical traveling waves that are perfectly out-of-phase.

(1800) Young's two-slit experiment

Young's two-slit experiment, as illustrated in Figure 7.4 below, is a classic example of the interference of light waves and resulting diffraction patterns.

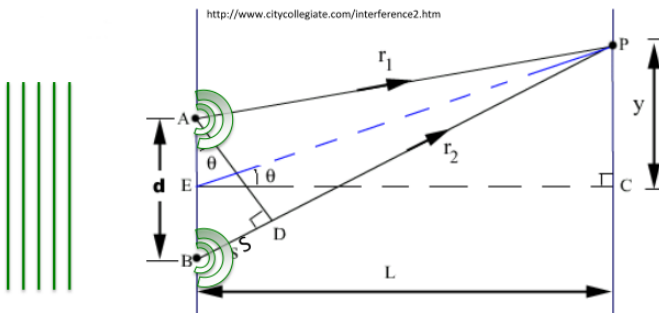


Figure 7.4: Young's two-slit experiment.

In Young's experiment, a plane light wave of wavelength λ traveling to the right with an "in-phase" wavefront parallel to the grating produces two coherent circular waves emanating from the 2 slits at A and B. The two waves will add up in phase at point P on a screen if the path length difference, $s = BD$, is an integer multiple of the wavelength λ .

$$s = d \sin \theta = n\lambda \rightarrow \text{interference maxima at } y$$

To produce an interference fringe pattern of dark, destructive interference and bright constructive interference spots, $d \approx \lambda$

If $d < \lambda$, $\sin \theta = \frac{n\lambda}{d} > 1 \rightarrow$ impossible

If $d \gg \lambda$, $\sin \theta = \frac{\lambda}{d} \rightarrow$ too small to separate n=1 max. from the direct beam

Note that Young's 2-slit experiment proved that light was a wave. Einstein later proved that light could also act as a quantum particle. This mysterious wave-particle duality principle is observed over the entire spectrum of electromagnetic radiation.

7.3 X-ray Diffraction History

In 1912, Max von Laue, a young Assistant Professor in Munich, was inspired by the PhD thesis work of Ewald, who was working in the Sommerfeld Lab at the University of Munich. Ewald's thesis derived the theoretical expressions describing the scattering of waves from a periodic array of dipole oscillators. Laue realized that Ewald's discovery was directly related to the scattering of waves from a crystal's periodic structure and collaborated with Friedrich and Rongten's (discoverer of X-rays) student Knipping to explore this idea. Their experiment demonstrated an X-ray diffraction pattern from a crystal and proved that X-rays were waves with a wavelength on the order of a d-spacing within a crystal.

Later that same year, W.L. Bragg, excited by the Laue discovery, worked with his father to develop a simpler picture to explain X-ray diffraction.

7.4 How does X-ray diffraction work?

First, consider the reflection of a plane wave from a plane of atoms, as represented by a horizontal line in Figure 7.5. Note that the atoms do not have to be evenly spaced within the plane.

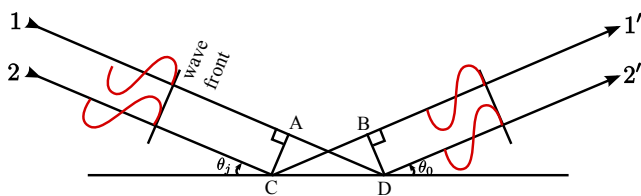


Figure 7.5: Reflection from a plane of atoms

A plane wave is represented by rays 1 & 2 in phase at AC in Figure 7.5, and also reflecting in phase. The path length difference of rays 1-1' and rays 2-2' is equal if and only if $AD = BC$, and by trigonometry, this can only occur when the incident angle is equal to the outgoing angle.

Since path lengths will be equal for all rays under this specular reflection condition, constructive interference will occur when the outgoing angle equals the angle of incidence. This is known as the **Law of Reflection**.

$$AD = CB \rightarrow \theta_i = \theta_o$$

Conversely, if $\theta_o \neq \theta_i$ the sum of all waves cancels each other out to produce destructive interference.

Scattering from two planes

Second, consider the reflection from a set of equally spaced atom planes as illustrated in 7.6.

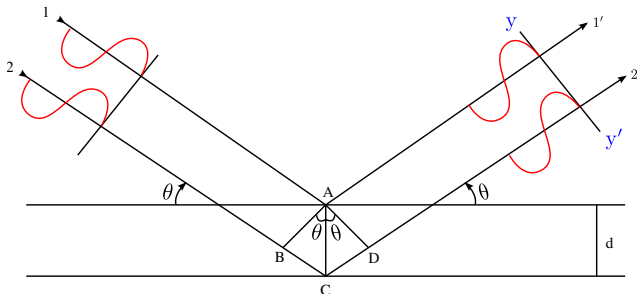


Figure 7.6: Reflection from a set of equally spaced atom planes

We use the Law of Reflection and some high school geometry to realize that

$$BC = CD = d \sin \theta. \quad (7.1)$$

Here, we would like to know when the scattering from both planes will result in constructive interference. If the path difference, $\delta = BCD$ of rays 1 and 2, is equal to an integer multiple of the wavelength ($n\lambda$, where n is an integer), then the scattered waves $1'$ & $2'$ are in-phase at yy' . If the angle of incidence were tilted down slightly, then the waves would no longer be in phase, and the conditions would no longer allow for constructive interference. Applying the geometric relationship below yields **Braggs' law**. This states the essential condition necessary for diffraction to occur.

$$n\lambda = 2d \sin \theta \quad (7.2)$$

n - order of reflection, number of wavelengths in the path difference between rays scattered by adjacent planes

If θ is slightly different from the Bragg condition, each successive ray $1', 2', 3', \dots$ will be slightly phase-shifted with respect to the previous ray as illustrated in Figure 7.7. The amplitudes of the waves would sum to zero since every plane will have another plane at some depth, which will scatter out of phase by 180° .

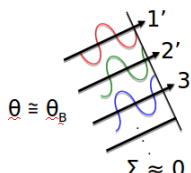


Figure 7.7: Successive phase shifts of reflected rays when $\theta_i \neq \theta_B = \sin^{-1}(\frac{n\lambda}{2d})$.

What about the “n” in $n\lambda = 2d \sin \theta$?

The “n” value, or order of reflection, may take on any integral value as long as $\sin \theta$ does not exceed one in Braggs’ law equation. For fixed values of d and λ , various n values (n=1,2,3...) correspond to different angles of incidence ($\theta = \theta_1, \theta_2, \theta_3...$) at which diffraction may occur.

For a first-order reflection (n=1) the path length and phase difference of the scattered waves 1' and 2' in Figure 7.6 would differ by one wavelength. For a second-order reflection (n=2) the path length and phase difference of the scattered rays would differ by two wavelengths. Thus, the waves scattered by all the planes of atoms are completely in phase, leading to constructive interference.

1st order n=1 $\rightarrow \delta = \lambda$ between consecutive planes spaced by “d”

2nd order n = 2 $\rightarrow \delta = 2\lambda$ between consecutive planes spaced by “d”

Another way of looking at the reflection order:

$$\lambda = 2 \frac{d}{n} \sin \theta \quad \frac{d}{n} = \frac{d_{hkl}}{n} = d_{nhnknl}$$

where hkl corresponds to the 1st order or fundamental reflection planes. Thus, the Bragg equation may be rearranged in the following form, in which the “n” term is dropped, and the d_{hkl} does not need to be the lowest set of indices for a given plane (i.e., $d_{hkl}=110, 220$, etc.):

$$\lambda = 2d_{hkl} \sin \theta \text{ or } \lambda = 2d \sin \theta_{hkl}$$

If the diffracted intensity is plotted as a function of $\sin \theta$, peaks corresponding to crystallographic planes will be visible as shown in Figure 7.8.

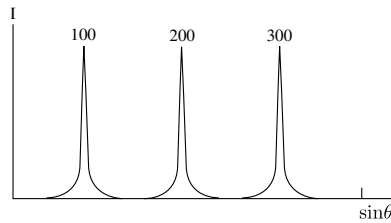


Figure 7.8: Diffracted intensity

Now, consider diffraction from NaCl (111), for which a two-dimensional representation is shown in Figure 7.9 below.

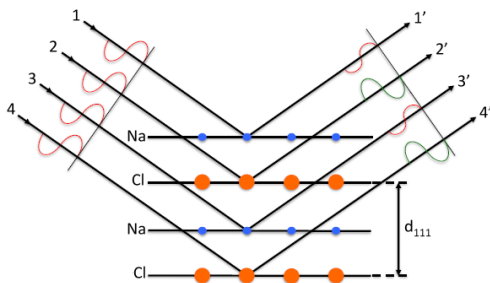


Figure 7.9: Bragg diffraction from the (111) planes of a NaCl crystal, where the alternating Na and Cl planes are equally spaced and scattering counter phase to each other.

The (111) diffraction condition ($\theta = \theta_{111}$) allows for constructive interference from the 1' and 3' waves and the 2' and 4' waves, as their path length difference measures exactly one wavelength. Note that rays 1'&3' from Na^+ are in phase with each other, but 180°out of phase with rays 2'&4' from Cl^- .

If Na and Cl were equal in scattering strength, then this would lead to complete destructive interference and 0 intensity. Due to the number of electrons in the two atomic species, which are the primary source of scattering in atoms, the scattering strength is not equal. Therefore, a small diffraction intensity peak will be observed for $\theta = \theta_{111}$ as shown in Figure 7.10.

For $\theta = \theta_{222}$, the overall path length becomes longer and all rays 1',2',3',4' from all planes Na^+ and Cl^- are in phase. This leads to constructive interference and higher intensity peaks shown in Figure 7.10. Note that this is a simplified model, which solely accounts for the path length difference effect in scattering from different planes that are not identical to each other. Other effects will be discussed later in the text.

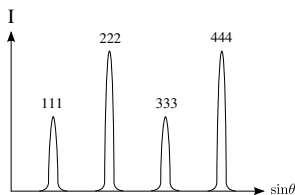


Figure 7.10: NaCl diffraction peaks

Observing the Bragg angles tells us about unit cell dimensions, namely the d-spacing between planes, which can be used to derive the lattice constant. Furthermore, observing relative intensities as shown in the NaCl structure for different θ_{hkl} tells us about the structure within the unit cell. Namely, there was a pair of ions (Na^+ and Cl^-) associated with an FCC lattice point.

On the other hand, for a simple FCC metal, the (111),(333), ... peaks would not have been weak.

Hint: Look for weak and absent reflections to determine the atomic arrangement within the unit cell.

7.5 Absent (or forbidden) Reflections

Figure 7.11 below shows a side-view projection of the (100) planes in a simple FCC metal. The white circles represent atoms that are half a lattice spacing out of the plane of the page.

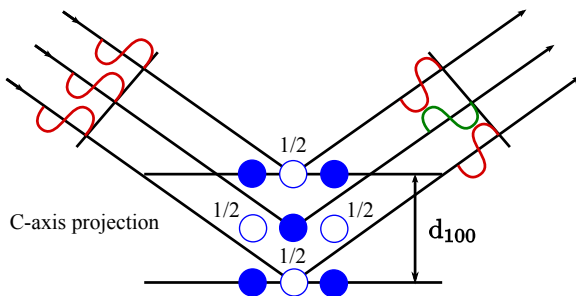


Figure 7.11: The (100) Bragg diffraction condition from an FCC metal crystal.

The plane of atoms halfway between the (100)-marked planes will scatter at 180° out of phase, canceling out the waves reflecting at the (100) planes. Therefore, the $\theta = \theta_{100}$ Bragg diffraction condition leads to perfect destructive interference, and the (100) reflection is absent or not allowed. For simple cubic, the atoms halfway between the planes would not be present. However, at the (200) Bragg condition, all (200) planes scatter in phase, and the (200) reflection would be observed. This reinforces the fact that in an FCC structure, the following conditions are true:

- ◊ (200), (400), (600), etc. allowed.
- ◊ (100), (300), (500), etc. forbidden
- ◊ $\therefore hkl$ all even or hkl all odd (unmixed) for FCC

How would Bragg diffraction show that a crystal is cubic? i.e., not orthorhombic

Realize that for the cubic structure, the following relationship between the d-spacing of the (110) and (100) planes is true: $\frac{\sin \theta_{100}}{\sin \theta_{110}} = \frac{d_{110}}{d_{100}} = \frac{1}{\sqrt{2}}$.

By determining the reflection angle for the (100) and (110) planes and then taking the ratio of the sines, the cubic structure can be confirmed if it is equal to $\frac{1}{\sqrt{2}}$.

This same procedure may be used to determine if a crystal structure is FCC. Since (110) and (100) are forbidden for FCC, then (220) and (200) can be used instead.

8 Absorption/Emission

8.1 Spectrometers

The following three X-ray sources will be discussed in this text:

- ◊ X-ray tube e.g., Cu target
- ◊ Radioactive Source e.g., Fe^{55}
- ◊ Synchrotron e.g., e^- storage ring

An X-ray tube contains three vital components: a source of electrons, a high voltage to accelerate these electrons, and a metal target on which these highly accelerated electrons will collide. Figure 8.1(a) below illustrates the cross-section of an **X-ray tube**. This consists of an evacuated glass casing that insulates the anode at one end from the cathode. The cathode is a tungsten filament, and the anode is a water-cooled block of copper that also contains the desired target metal at one end (Cu, Mo, Cr, Ag, or W). A lead of the high-voltage transformer, detailed in Figure 8.1(b) is connected to the filament and the other to the ground. The anode target is grounded. In operation, the filament is heated with a current and emits electrons (thermal emission) that are accelerated to the target via the electrostatic potential. Around the filament is a metal focusing cup, which is kept at a high negative voltage close to that of the filament and tends to focus the electrons on a focal spot on the target. X-rays are emitted from this focal spot in all directions and escape through the beryllium window in the tube.

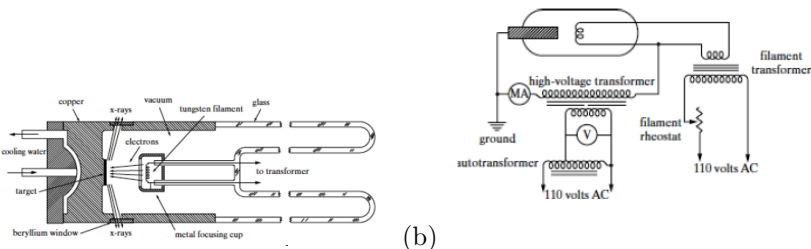


Figure 8.1: (a) Schematic cross-sectional view of an X-ray tube. (b) Electrical circuitry for passing current through W filament that is held at a high negative potential. Copied from Cullity and Stock Ref. [?]

Figure 8.2, below illustrates an X-ray radiation spectrum produced by an X-ray tube source.

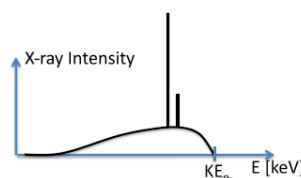


Figure 8.2: X-ray radiation spectrum from an X-ray tube.

8.2 Bremsstrahlung Radiation

Bremsstrahlung radiation is the continuous smooth part of the X-ray spectrum from an X-ray tube shown in Figure 8.2. This occurs due to the deceleration or braking of electrons in the target. The acceleration (or deceleration) of any charge q , an electron in this case, generates electromagnetic radiation.

Figure 8.3 illustrates a charge q , with acceleration in the \bar{a} direction. If you look in the α direction relative to its acceleration vector, you will observe electromagnetic radiation at point P, whose distance from charged particle q is indicated by \bar{r} . The electric field vector \bar{E} of this radiation points in the transverse direction to the propagation direction \bar{r} . The following formula yields the magnitude of the electric field generated by the accelerated charge:

$$|\bar{E}| = \frac{q \sin \alpha}{4\pi \epsilon_0 c^2 r} \quad (8.1)$$

The following relationships for the electric field also hold true:

- ◊ $\bar{E} \perp \bar{r}$ (transverse wave)
- ◊ $\bar{E} \perp (\bar{a} \times \bar{r})$

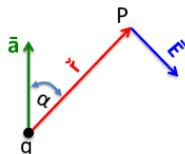


Figure 8.3: Radiation from an accelerated charge

In the case of X-ray tube Bremsstrahlung radiation, the electrons are accelerated from the tungsten filament cathode to the grounded anode. Electrons accelerating in the negative \bar{z} direction as illustrated in Figure 8.4 create an azimuthally symmetric dipole radiation field. In Figure 8.4, the angle θ is the complement of the angle α in Figure 8.3. Note that the magnitude of \bar{r} does not change, and θ is the factor that affects the intensity of the generated \bar{E} field. Because the intensity is proportional to the magnitude of the electric field squared, it is also proportional to $\sin^2 \alpha$ or $\cos^2 \theta$. This is consistent with what is observed in Figure 8.4 and the three-dimensional representation in Figure 8.5, since the intensity at a minimum when θ is 90° and at a maximum when θ goes to 0° .

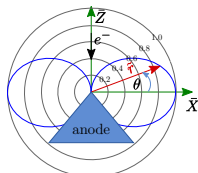


Figure 8.4: Intensity of \bar{E} field with varying θ . There is a node in the X-ray radiation field along the azimuthal z-axis. The maximum lies in the xy plane.

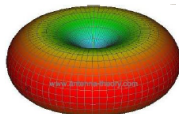


Figure 8.5: Azimuthally symmetric $\cos^2\theta$ dipole radiation field.

$$\sin \alpha = \cos \theta$$

$$I \propto |\vec{E}|^2 \propto \cos^2 \theta$$

Max intensity $\perp \hat{z}$

8.3 Synchrotron Radiation

Synchrotron radiation occurs when electrons are accelerated in a curved path by a magnetic field. The electron experiences centripetal acceleration in the radial direction, producing a dipole radiation pattern of the same toroidal shape as illustrated in Figures 8.4 and 8.5. The minimum intensity is observed in the radial direction and maximized perpendicular. However, there is an extreme relativistic effect due to the electron's speed being nearly up to the speed of light, such that the dipole radiation field is distorted in the lab frame of reference, creating an extremely narrow cone of radiation in the forward direction of the electron's tangential velocity.

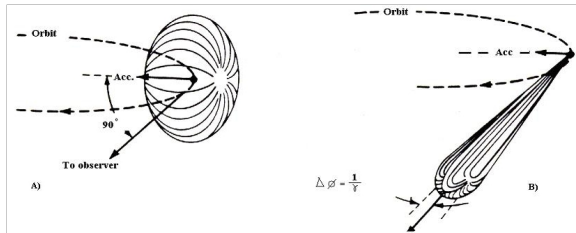


Figure 8.6: (A) Dipole radiation field due to centripetal acceleration of a charged particle. (B) Relativistic effect on dipole radiation field.

Recall that Bremsstrahlung radiation is white, or polychromatic, radiation resulting from decelerating electrons following inelastic collisions with target atoms. The kinetic energy analysis of this process is as follows:

The maximum energy loss is the electron's kinetic energy (KE) at the vacuum-target interface when the electron loses all of its energy from one inelastic collision.

$$\Delta E_{Max} = KE_{e^-} = \frac{1}{2}mv^2 = h\nu = \frac{hc}{\lambda}$$

This maximum photon energy for Bremsstrahlung radiation, by the de Broglie relationship $\frac{hc}{\lambda}$, is directly related to the minimum wavelength generated by the X-ray tube. Note that this is a maximum case, and the range of energies will be anywhere from this maximum value to zero. This maximum kinetic energy is, therefore, directly related to the set potential of the X-ray tube, as shown below.

$$KE [\text{keV}] = V [\text{kV}]$$

I.e., if the X-ray tube high voltage, $HV = 50 \text{ kV} \rightarrow \text{Max photon energy} = 50 \text{ keV}$

The maximum photon energy in the continuous Bremsstrahlung spectrum will show 50 keV at its maximum, along with lower values.

de Broglie wavelength relationship: $\lambda = \frac{hc}{E} \rightarrow \lambda[\text{\AA}] = \frac{12.40}{E[\text{keV}]} \rightarrow \text{short wavelength limit } \lambda_{SWL}[\text{\AA}] = \frac{12.40}{V[\text{kV}]}$

Therefore, the Bremsstrahlung spectrum will contain a continuum of wavelengths showing an intensity pattern and a short wavelength limit (SWL) corresponding to the maximum available energy. This is because wavelength and energy are inversely proportional. Figure 8.7 below shows a radiation spectrum from a copper X-ray tube for various set potentials (25 kV, 20 kV, 15 kV, etc.). The smooth curve indicates the continuous or Bremsstrahlung radiation curve, with the short wavelength limit (SWL) corresponding to the leftmost point on a given curve. The spikes are indicative of characteristic radiation, which will be discussed next.

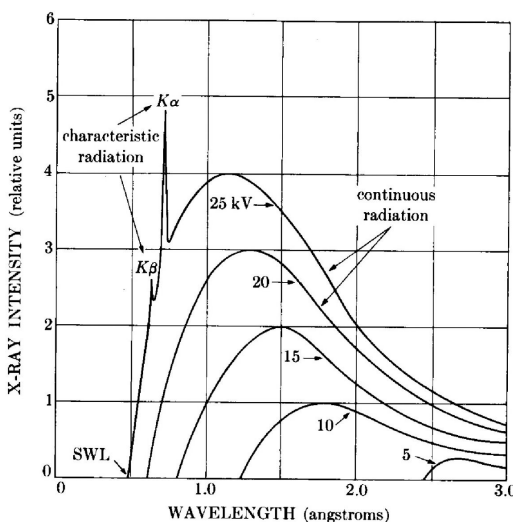


Figure 8.7: Bremsstrahlung radiation spectrum from Cu tube at different high voltage settings. Copied from Cullity and Stock Ref. [?]

Note: for $V=20 \text{ kV} \rightarrow \lambda_{SWL} = 0.62 \text{\AA}$

The integrated intensity, or area under the curves in Figure 8.7, is proportional to the voltage of the X-ray cubed multiplied by the atomic number of the target and the current through the filament. Therefore, since each X-ray tube is rated for a given maximum power (e.g., 3 kW), one would typically increase the voltage rather than the current to maximize the integrated intensity.

$$I \propto V^3 Z_{\text{target}} i$$

The following is a log-scale comparison of the spectra from different synchrotrons. Notice the Bremsstrahlung spectrum near the bottom of the plot.

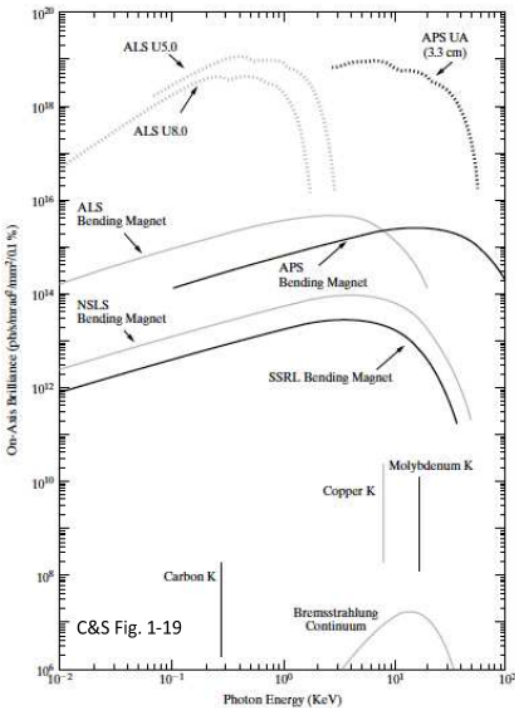


Figure 8.8: On-Axis Brilliance vs Photon Energy (KeV) for various synchrotron sources compared to an X-ray tube spectrum. Copied from Cullity and Stock Ref. [?]

8.4 Characteristic Spectrum

Raising the voltage on an X-ray tube above a certain critical value for a given target metal yields sharp, narrow intensity peaks, or **fluorescent lines** superimposed on the continuous radiation spectrum. The **characteristic spectrum** consists of several of these fluorescent lines (i.e., K, L, M, etc.) that are specific to the target in use. For fluorescent lines from the target to occur, the electron beam must possess enough kinetic energy to overcome the binding energy of an inner core electron and knock it out of its atom. The transition of a higher energy electron to fill this hole results in the production of an X-ray, which is characteristic of the given target element. Figure 8.9 illustrates these fluorescent peaks on a continuous background radiation spectrum for a copper target sample at 30 kV.

$$\text{For fluorescence: } KE_{e^-} = eV \geq W_K (\text{or } \geq W_L)$$

where KE_{e^-} is electron energy & W_k or W_L is the binding energy of target electrons.

Typically, the K fluorescence lines comprised of $K\alpha_1$, $K\alpha_2$ and $K\beta_1$ are useful in X-ray diffraction because of the much higher intensity in these peaks compared to

the Bremsstrahlung background. The $K\alpha_1$ and $K\alpha_2$ lines, referred to as the **$K\alpha$ doublet**, have very close wavelengths and are sometimes treated as a single line. In addition, the subscript in the $K\beta_1$ is usually dropped. The K indicates the principal quantum number "n" of the 1s hole that is being filled by the transition of an outer electron to fill this hole. A useful diagram of the electron energy states for copper is shown in Figure 8.10, with different principal energy levels ($n=1=K$ and $n=2=L$) followed by an integer number that indicates the sub-shell within a given energy level (i.e., L_1 , L_2 , etc.). When an electron in the K shell is knocked out, the ion is left in a high-energy state. This target metal atom (ion) transitions to its ground state when a higher-energy electron, such as one from the L shell or the M shell, drops down to fill the 1s core hole. Filling a K hole with an L-shell electron is more probable than filling it with an M-shell electron, thereby yielding a higher $K\alpha$ (corresponding to the L shell transition) intensity peak relative to the $K\beta$ (corresponding to the M shell transition) intensity peak. Note that the K X-ray fluoresc

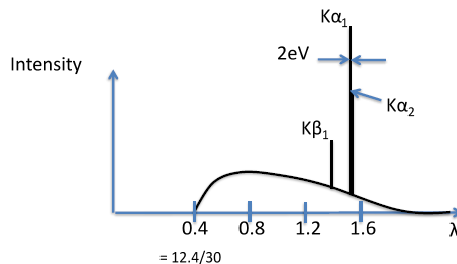


Figure 8.9: Cu characteristic spectrum at 30 kV. Note that the short wavelength limit is at 0.4 Å due to this 30 keV accelerated electron beam.

In Figure 8.9 above, note that the intensity of the $K\alpha$ peak is one hundred times stronger than the background radiation curve. Furthermore, the $K\alpha$ doublet differ in intensity by a factor of two, and the $K\alpha_1$ and $K\beta_1$ differ by approximately a factor of five.

$$\frac{I_{K\alpha}}{I_{Cont}} \approx 100$$

$$\frac{I_{K\alpha_1}}{I_{K\alpha_2}} = 2 \quad \frac{I_{K\alpha_1}}{I_{K\beta_1}} \approx 5$$

The arrows in Figure 8.10 below demonstrate the $K\alpha_1$ $K\alpha_2$ and $K\beta_1$ transitions, with their lengths representing the difference in the energies of the two states. This energy difference also equals the energy of the outgoing fluorescent photon. Note that an arrow does not go from the 1s to the 2s electron energy state. Because the electron originally in the 1s state has an orbital angular momentum of $l = 0$ and the angular momentum of the photon is 1, the transition needs to be a p to s to conserve angular momentum. The 1s and 2s states do not differ in angular momentum by 1, thus the transition has a very low probability for producing fluorescent radiation.

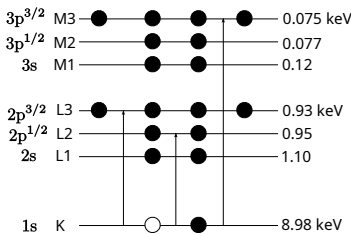


Figure 8.10: Copper electron energy levels showing a K hole, which can transition to the L_3 , or L_2 , or M_3 level to produce a $K\alpha_1$, $K\alpha_2$, or $K\beta_1$ XRF photon.

Note that in Figure 8.10, there are twice the number of electrons in the L_3 state than in the L_2 state. Due to this, the $K\alpha_1$ electron transition from the L_3 energy level to the K energy level is twice as likely to occur as the $K\alpha_2$ transition from the L_2 energy state to the K energy state. This is consistent with the double intensity of the $K\alpha_1$ fluorescence peak relative to the $K\alpha_2$ fluorescence peak shown above. The following calculations based on the conservation of energy determine the characteristic $K\alpha$ and $K\beta$ fluorescence energies for a copper target and their corresponding wavelengths:

$$E_{\gamma} \quad \lambda$$

$$E_{K\alpha_1} = W_K - W_{L_3} = 8.05 \text{ keV}, 1.540 \text{\AA}$$

$$E_{K\alpha_2} = W_K - W_{L_2} = 8.03 \text{ keV}, 1.544 \text{\AA}$$

$$E_{K\beta_1} = W_K - W_{M_3} = 8.19 \text{ keV}, 1.392 \text{\AA}$$

$$(\lambda = \frac{hc}{E} \rightarrow \lambda [\text{\AA}] = \frac{12.4}{E[\text{keV}]})$$

A measured X-ray spectrum from a Mo rotating anode is shown in Fig. 8.11.

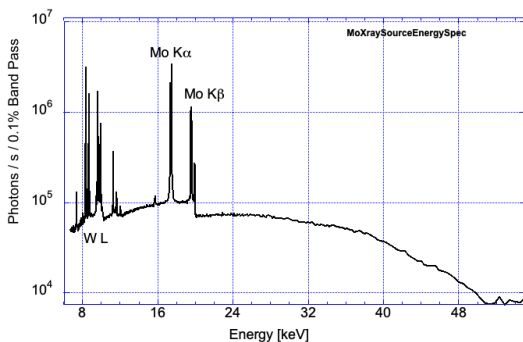


Figure 8.11: X-ray spectrum from a Mo rotating anode operating at 50 KV and 40 mA that was collected by a $\theta - 2\theta$ scan of a Si(220) monochromator crystal. The W L XRF lines between 7.5 and 12 keV are due to a surface layer of W deposited on the Mo surface of the anode from the W filament. These can be removed by surface polishing.

8.5 Auger Effect

The **Auger effect** is a non-radiative process that competes with the radiative X-ray emission process to fill an inner electron-hole (core hole). Rather than producing a photon, this process ejects an electron known as an **Auger electron**. An energy level diagram for Auger electron emission from a copper atom is illustrated in Figure 8.12. This process involves three discrete electron energy levels: the first is the K energy level of the core hole, the second is the L_1 or higher energy level from which an electron drops down to fill the K-hole, and the last is the L_3 energy level from which the Auger electron is emitted. Based on energy conservation, the kinetic energy of the Auger electron, therefore, is equal to the difference between its binding energy and the energy difference between the L_1 and K energy levels involved in the filling of the electron-hole.

Energy analysis, where E_e is the energy of the Auger electron:

$$E_e = W_K - W_{L_1} - W_{L_3}$$

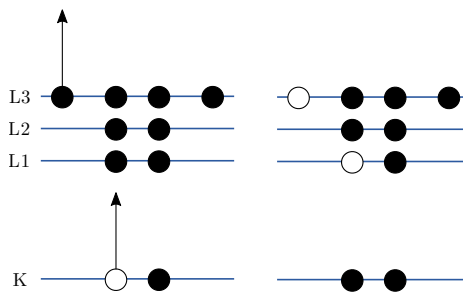


Figure 8.12: Cu KL_1L_3 Auger process.

$$E_e = 8.98 - 1.10 - 0.93 = 6.95 \text{ keV}$$

Recall that the Auger effect and radiative fluorescence are two processes that compete to fill a K-electron hole. If the **fluorescence yield**, or the probability of filling a K-electron hole via X-ray emission, is ω_k , then the probability of filling an electron K-hole via the Auger effect is $1 - \omega_k$. This Auger emission probability is very high for a low atomic number. For germanium with atomic number 32, there is an equal probability of filling the 1s or K electron-hole by either the non-radiative or radiative processes. Elements with an atomic number lower than germanium (i.e., $Z < 32$) will favor the Auger effect over a radiative process for filling a K hole.

Fluorescence yield: ω_k = probability for K hole being filled by radiative process

$$\text{K Auger Probability} = 1 - \omega_k$$

The curve labeled “K” in Figure 8.13 below shows this relationship, in which a higher atomic number corresponds to a higher fluorescence yield probability for filling a K hole. The L-hole electron fluorescence probability is also shown in this diagram as the line labeled “L.”

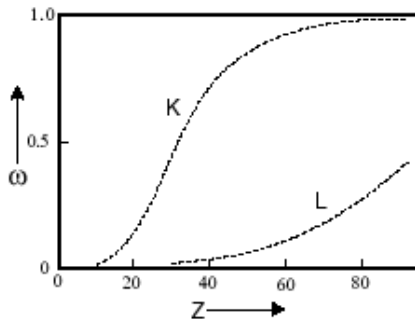


Figure 8.13: Fluorescence yield vs atomic number

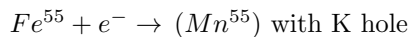
Note that because electrons cannot travel through air very easily like X-rays, the Auger spectrometer is located inside a vacuum chamber. Furthermore, Auger electron spectroscopy is much more surface-sensitive than X-ray fluorescence spectroscopy. Auger electron spectroscopy is primarily used as a surface science technique, where, for example, it can be used to determine the level of surface contamination by low-Z elements like C and O down to a level of 0.01 monolayers.

8.6 Radioactive Source

Besides X-ray tubes and synchrotrons, another X-ray source comes from radioactive isotopes such as Fe^{55} , which exhibits a high probability of undergoing electron capture. In this nuclear process, a proton in the nucleus combines with the 1s electron, creating a neutron and a neutrino.



Notice the conservation of charge, baryon number, and lepton number in this process. The atomic species is now manganese with an electron hole in its K energy level. Following this, the manganese can emit a $K\alpha_1$ XRF photon in filling the K hole with an L_3 level electron as shown in Figure 8.14. The observed XRF spectrum will be characteristic of manganese.



Example:

Fe^{55} Electron Capture

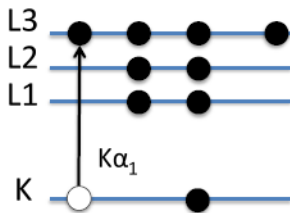
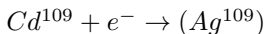


Figure 8.14: $K\alpha$ fluorescence in manganese following Fe^{55} electron capture

$$E_\gamma = W_K - W_{L3} = 5.90 \text{ keV} \leftarrow K\alpha_1$$

The isotope Cd^{109} undergoes a similar process, whereby electron capture leads to its conversion into Ag^{109} , and characteristic fluorescence lines of Ag may be observed by XRF spectroscopy.



8.7 X-ray Absorption

When X-rays pass through a material, part of the intensity is transmitted, and part is absorbed. The attenuation of the incident X-ray intensity is directly related to the traversed distance of the X-ray through the material. Referring to the diagram in Figure 8.15, if an X-ray of **incident intensity** I_o impinges on a slab of material of known composition and passes through a distance dx , the fractional drop in the **transmitted intensity** $-dI_x/I$ is proportional to this fractional distance traversed.

$$I_{absorbed} = I_o - I_x$$

I_o = incident intensity

I_x = transmitted intensity

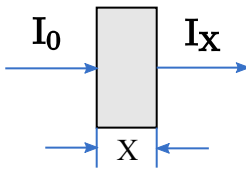


Figure 8.15: Drop in X-ray intensity over distance x through material

The constant of proportionality relating the absorbed intensity to the distance traversed is μ , or the **linear absorption coefficient**.

In differential form: $\frac{-dI}{I} = \mu dx$, μ = linear absorption coefficient

$$\int_{I_0}^{I_x} \frac{dI}{I} = - \int_0^x \mu dx \rightarrow \ln(I_x) - \ln(I_0) = -\mu x$$

Exponential Relationship:

$$I_x = I_0 e^{-\mu x}$$

The plot in Figure 8.16 below shows this exponential relationship, in which the incident intensity I_x decays at a rate of μ times the distance x through the material.

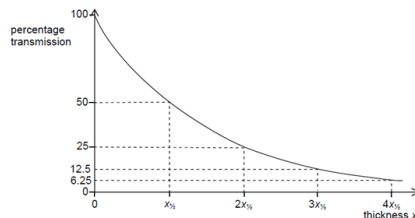


Figure 8.16: Transmitted intensity vs thickness traversed

The linear absorption coefficient is directly proportional to the density of the material; thus, the quantity $\frac{\mu}{\rho}$, called the **mass absorption coefficient**, is constant for a given material regardless of its state of matter. The $\frac{\mu}{\rho}$ value for a given atom is normally listed in tables rather than listing various μ values for various compounds or elements and accounting for structure or density factors. Furthermore, the mass absorption coefficient is a function of the atomic number of the element as well as the energy of the X-ray. The energy dependence is because there is a critical energy above which the X-rays can overcome the binding energy of the electrons in the atoms of the material and emit a photoelectron. Thus, there is a much higher probability of X-ray absorption above this critical energy, leading to a higher μ value. Furthermore, there is a certain distance at which the initial intensity I_0 is divided by a factor of e . This distance is equal to $\frac{1}{\mu}$, which is referred to as the **absorption length**.

$$\mu \propto \rho \rightarrow \frac{\mu}{\rho} \text{ constant of material, independent of state (solid, liquid, gas)}$$

$$\frac{\mu}{\rho} = f(Z, E_\gamma) \equiv \text{mass absorption coefficient}$$

$$\mu^{-1} = \text{absorption length}$$

For chemical compounds or mixtures, the mass absorption coefficient of the substance is the weighted average of the mass absorption coefficient of its constituent elements. A general formula for this is shown below. As a useful example, the mass absorption coefficient for air is calculated in Table 8, using tabulated mass absorption coefficients of nitrogen, oxygen, and argon along with their respective weight percents in air.

$$\frac{\mu}{\rho} = \sum_{i=1}^n w_i \left(\frac{\mu}{\rho} \right)_i, \quad w_i = \text{weight fraction}$$

Mass absorption coefficient for mixture of n elements with individual weight fractions, w_i , and mass absorption coefficients, $(\frac{\mu}{\rho})_i$.

Example: Air = 76% N_2 + 23% O_2 + 1.3% Ar

i	w_i	$(\frac{\mu}{\rho}) \frac{cm^2}{g}$	$w_i \times (\frac{\mu}{\rho})_i$
N_2	0.76	7.14	5.53
O_2	0.23	11.0	2.53
Ar	0.013	120.0	1.56
		(C&S Appendix 8)	

$$@ \text{STP } \rho_{Air} = 0.0013 \text{ g/cm}^3, \mu_{Air} = 0.0124 \text{ cm}^{-1}, \frac{1}{\mu} = 81 \text{ cm}$$

Table 8: Calculation of the X-ray mass absorption coefficient in Air at $E_\gamma=8.05$ keV (Cu $K\alpha$)

From these calculations, it is determined that a copper $K\alpha$ (8.05 keV) X-ray beam is attenuated to $\frac{1}{e} = 0.37 = \frac{I_x}{I_0}$ after traveling through 81 cm of air. Figures 8.17 and 8.18 below plot the linear absorption coefficients and X-ray transmission for beryllium as a function of the photon energy. Recall that a thin beryllium foil is used as an X-ray tube vacuum seal/window.

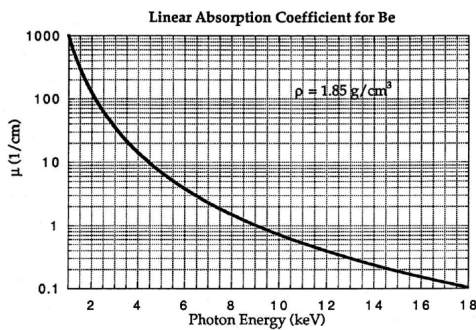


Figure 8.17: Beryllium linear absorption coefficient as a function of X-ray energy. Used https://henke.lbl.gov/optical_constants/atten2.html to calculate $1/\mu$.

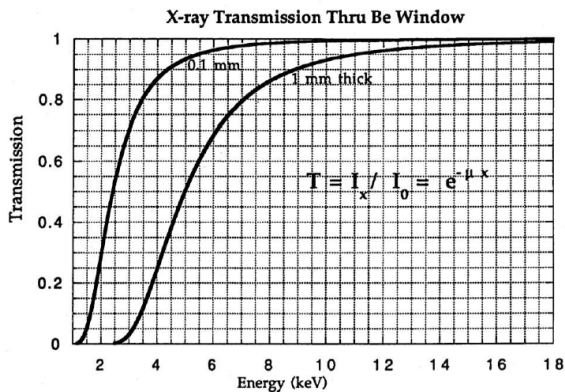


Figure 8.18: X-ray Transmission through a Be window of 0.1 and 1.0 mm in thickness. Output from https://henke.lbl.gov/optical_constants/filter2.html.

8.8 X-ray Transmission Filters

As previously shown, the spectrum from an X-ray tube yields several fluorescent lines, such as the characteristic $K\alpha$ and the $K\beta$. Some applications require that an X-ray beam be monochromatic, so that the $K\beta$ fluorescence is significantly reduced compared to the $K\alpha$ fluorescence. This more monochromatic spectrum may be achieved by using a metal foil filter that preferentially reduces the intensity of the $K\beta$ in the X-ray spectrum compared to the $K\alpha$. Note that absorption filters cannot be used to remove the unwanted $K\alpha_2$ component from the $K\alpha$ radiation. Figure 8.19 below shows a basic setup of a nickel foil filter used in a copper X-ray tube.

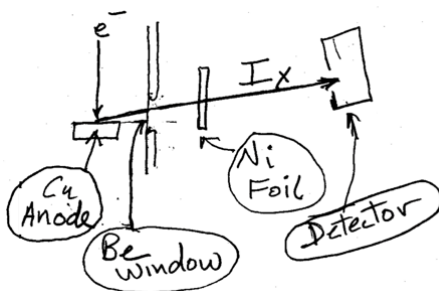


Figure 8.19: Ni foil filter and Cu X-ray tube

Transmission filters make use of the X-ray absorption edge of a particular element. In the second plot of Figure 8.20 below, the absorption edge for nickel can be observed. This discontinuity corresponds to the energy required to eject an inner core electron from an atom of the filter material. At energies just below this edge, the $\frac{\mu}{\rho}$ mass absorption coefficient is significantly less than the mass absorption coefficient at energies slightly above the edge. This translates into higher transmission for X-rays with energies below the absorption edge line on the energy axis. By this process, the initial X-ray spectrum, plotted as I_o at the top of the figure, undergoes a significant reduction in the intensity of the $K\beta$ line as shown in the final plot of transmitted intensity, I_x . Note that the high-energy background radiation is also significantly reduced in the final plot.

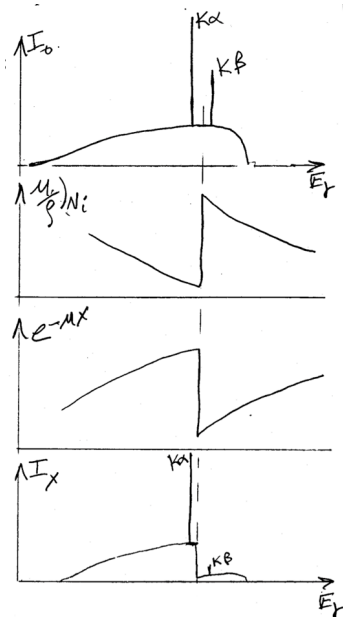


Figure 8.20: How a Ni transmission filter affects the spectrum from a Cu anode X-ray tube.

Recall the X-ray transmission intensity formula, $I_x = I_0 e^{-\mu x}$. For an 8 mil Ni Filter (1 mil = 0.001" = 25.4 μm), the intensity of the $K\alpha$ fluorescence is five hundred times greater than the $K\beta$ fluorescence. Recall that without a filter, the $K\alpha$ transmitted intensity was five times greater than the $K\beta$ intensity.

$$8 \text{ mil (0.8 mils = } 20 \mu m) \text{ Ni Filter: } \frac{I(K\alpha)}{I(K\beta)} = 500$$

In general, a filter with an atomic number that is one less than the target metal in the X-ray tube is used, and the thickness X is chosen such that $\frac{I_{K\alpha}}{I_{K\beta}} = \frac{1}{500}$. This Z-1 relationship is utilized so that the absorption edge lies just above the desired $K\alpha$ and below the $K\beta$ to be filtered. The mass-absorption law $I_x = I_0 e^{-(\mu/\rho)\rho x}$ may be used to calculate the thickness of the filter.

Generally, use a $Z - 1$ filter:

Cu \rightarrow Ni Filter

Ag \rightarrow Pd Filter

Mo \rightarrow Zr \leftarrow (Z-2)

A thicker filter will better suppress the $K\beta$ component, but this will also result in unwanted suppression of the $K\alpha$ component. Thus, it is useful to follow the $\frac{1}{500}$ intensity ratio.

Figure 8.21 below illustrates a general absorption spectrum for an atom by plotting the log of the mass absorption coefficient against increasing energy. Note the presence of the absorption edge previously discussed, which is labeled as the “K-edge.”

In addition to the K-edge, other discontinuity spikes corresponding to the L electron shell binding energies are present. The location of the K-edge and its associated K-branch, further to the right on the energy axis, is due to the fact that this is the innermost electron shell and, therefore, has the highest binding energy for a given atomic element.

The overall absorption, labeled $\left(\frac{\mu}{\rho}\right)_{tot}$ is equal to the addition of the absorption from the different electron energy level branches, i.e., $\left(\frac{\mu}{\rho}\right)_K$, $\left(\frac{\mu}{\rho}\right)_{L_1}$, etc. Note that $\left(\frac{\mu}{\rho}\right)_i$ increases as the cube of atomic number, Z, and decreases as $1/E^3$. For instance, if the X-ray energy is increased from 10 keV to 20 keV, the X-ray absorption will decrease by an eighth if there are no edges between 10 and 20 keV. Furthermore, if the atomic species Z is increased by a factor of two from, say, Mg to Cr, then the mass absorption coefficient will increase by a factor of eight. Since the mass absorption coefficient $(\frac{\mu}{\rho})$ is inversely proportional to the cube of the energy, it follows that it is directly proportional to the wavelength cubed. These relationships are summarized in Figure 8.21 below.

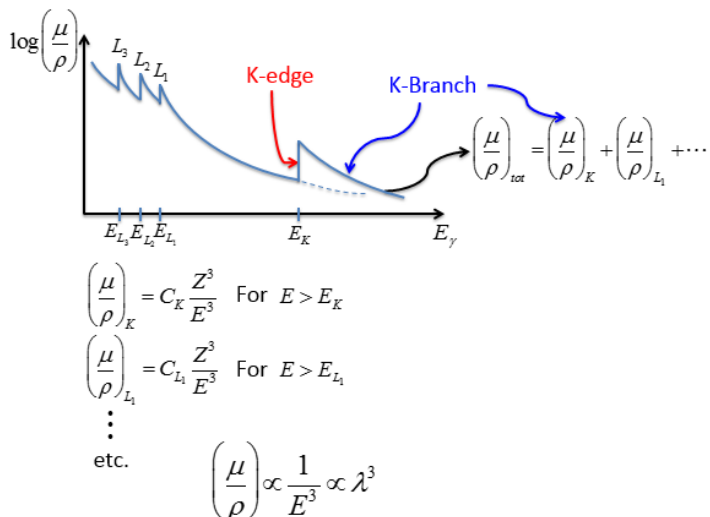


Figure 8.21: An atomic X-ray absorption spectrum.

8.9 Photoelectric effect

X-ray absorption is dominated by the **photoelectric effect**. This quantum effect has the atom ejecting one of its core electrons with a kinetic energy of

$$E_{e^-} = h\nu - W_i,$$

where $h\nu$ is the photon energy and W_i is the binding energy of the core electron. Of course, as explained earlier and discovered by Einstein, this can occur only if $h\nu > W_i$. The photoelectric effect for a K or 1s electron is illustrated in Figure 8.22 below.

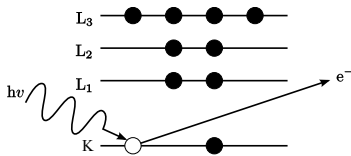


Figure 8.22: Photoelectric effect

In addition to the conservation of energy, the angular momentum in this process is conserved. That is, the incident photon's intrinsic angular momentum is $l = 1$, the 1s electron's angular momentum is 0, and when combined, produces an emitted photoelectron with $l = 1$ angular momentum. As illustrated in Fig. 8.23, if the polarization of the absorbed photon is along the z-axis, then conservation of angular momentum as a vector causes the angular distribution of the emitted photoelectron to be described by the p_z quantum state. That is, there is a high probability that the emitted electron will be detected along the z-axis and a minimal probability of its emission in the xy-plane. This is observed with angle-resolved photoemission studies of 1s electrons excited by linearly polarized X-rays.

Overall, the photon having angular momentum $l = 1$ leads to the dipole selection rule for electronic transitions where $\Delta l = \pm 1$.

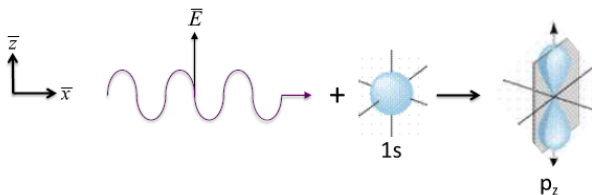


Figure 8.23: Conservation of angular momentum as a vector quantity in the 1s photoelectric effect.

8.10 X ray scattered by an electron

Classical Thomson scattering is a wave phenomenon in which an X-ray interacts with an electron, causing an acceleration of the electron due to the X-ray's oscillating electric field. (The effect of the X-ray's magnetic field on the electron's acceleration is negligible.) This idea is illustrated in Figure 8.24 below.

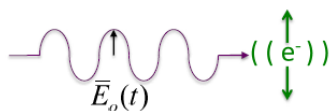


Figure 8.24: Thomson Scattering

As discussed earlier, for Bremsstrahlung and synchrotron radiation, the acceleration of a charge generates electromagnetic radiation. The oscillating \bar{E} field of the

incoming X-ray is given by the equation: $\bar{E}_0(t) = \bar{E}_0 \cos[2\pi(x - vt)/\lambda]$. The force on this electron is given by its charge multiplied by the incident electric field.

$$\bar{F} = -e\bar{E} = m_e\bar{a} \quad (8.2)$$

Therefore, the acceleration of the electron is given by the following equation:

$$\bar{a}(t) = \frac{-e\bar{E}_0(t)}{m_e} \quad (8.3)$$

This oscillating electron emits electromagnetic radiation in all directions as a scattered wave. The wavelength of this scattered wave λ_s is equal to the wavelength of the incident X-ray wave λ_0 . Therefore, this type of scattering is coherent, or elastic.

$$\begin{array}{c} \text{Oscillating E-field } \bar{E}_0(t) = \bar{E}_0 \cos[2\pi(x - vt)/\lambda] \\ \downarrow \\ \text{Oscillating Charge Particle } (e^-) \\ \downarrow \\ \text{E-M Radiation (oscillating fields) } \lambda_s = \lambda_0 \end{array}$$

8.11 Theory for Radiation Generating by Accelerated Charge

The electric field generated by an accelerated charge q at a given position \bar{R} away from the charge is illustrated in Figure 8.25 below. The acceleration vector is indicated as \bar{a} in the vertical direction, with the \bar{R} position being at angle α relative to the charge q 's acceleration vector.

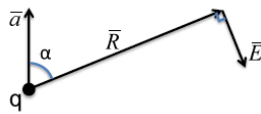


Figure 8.25: E-field at \bar{R} generated by the acceleration of charge q .

1. Direction of the electric field: $\bar{E} \perp \bar{R}$ and in-plane of \bar{R} and \bar{a}
2. Magnitude of the electric field: $|\bar{E}| = \frac{1}{4\pi\epsilon_0} \frac{qa \sin \alpha}{c^2 R} = \frac{1}{4\pi\epsilon_0} \frac{e^2}{m_e c^2} \frac{E_0 \sin \alpha}{R}$ Note that the electric field weakens as you increase the distance R from the charged particle.

$$|\bar{E}| = r_e \frac{E_0 \sin \alpha}{R}, \text{ where } r_e = 2.818 \times 10^{-5} \text{ \AA} \text{ is the Classical } e^- \text{-radius}$$

$$r_e = \frac{1}{4\pi\epsilon_0} \frac{e^2}{m_e c^2}$$

The classical **Thomson scattering** equation, as shown below, gives the intensity of the scattered X-rays from the electron as the square of the magnitude of the electric field generated by the oscillating electron. Note that the intensity is a maximum in

the direction perpendicular to the acceleration $\alpha = 90^\circ$ and is zeroed out along the acceleration direction.

$$I_e \propto |\bar{E}|^2 = E_0^2 \frac{r_e^2}{R^2} \sin^2 \alpha \quad (8.4)$$

$$\frac{I_e}{I_0} = \frac{r_e^2}{R^2} \sin^2 \alpha$$

I_e = Intensity of scattered X-rays from one e^- at \bar{R}

I_0 = Intensity of incident X-rays

$$I = \frac{c}{4\pi} |\bar{E}|^2 \equiv [energy \cdot area^{-1} \cdot time^{-1}]$$

Why do we ignore the Thomson scattering from the (charged) nucleus?

Relative to the scattering of electrons, the scattering intensity from protons in the nucleus of an atom is negligible, as shown in the following ratio:

$$\frac{I_p}{I_e} = \left(\frac{m_e}{m_p}\right)^2 = 3 \times 10^{-7}.$$

9 Scattering

X-rays interact very weakly with matter compared to electron and ion beams, making them the ideal angstrom wavelength probe for in situ atomic-scale structural analysis of buried structures. We have already discussed the photoelectric effect that leads to the absorption of an X-ray photon particle by an atom that becomes ionized by emitting a core photoelectron. Now, we will discuss the wave-like properties of X-ray scattering from electrons that lead to interference effects sensitive to the electron spatial distribution in materials. We will start with X-ray waves scattering from a single electron, and then escalate to two electrons, then to an electron "wave-function" cloud surrounding an atomic nucleus, then to atoms positioned within a unit cell, to a small single crystal with many unit cells, and finally to polycrystalline materials.

9.1 X-ray Scattering & Polarization

Consider an incident X-ray traveling in the \hat{x} direction and scattered from an electron " e^- " positioned at the origin "O" as shown in Figure 9.1 below. Since it is a transverse-wave, the incident X-ray, propagating in direction $\hat{s}_0 = \hat{x}$, has an electric field polarized in a direction that lies in the y - z plane. We can, therefore, decompose this electric field \bar{E}_0 with two orthogonal vector components: one in the \mathbf{y} -direction (\bar{E}_{0y}) and one in the \mathbf{z} -direction (\bar{E}_{0z}).

$$\bar{E}_0 = E_{oy}\hat{y} + E_{oz}\hat{z} \quad (9.1)$$

Note that the scattering angle 2θ is the complement of the angle α used in the Thomson scattering equation described at the end of the previous chapter and illustrated in Figure ???. Keep in mind that E-fields are complex with amplitudes and phases. See Appendix XXX for a mathematical review of complex functions.

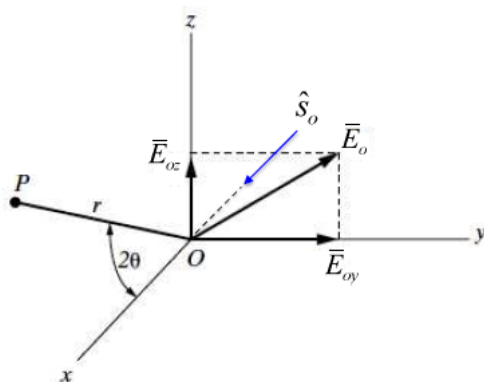


Figure 9.1: Incident X-ray traveling in \hat{x} direction, scattering from an electron at the origin, with the scattered X-ray traveling in the \mathbf{x} - \mathbf{z} scattering plane. The E-field of the incident X-ray, \bar{E}_0 , is separated into \mathbf{y} and \mathbf{z} components, \mathbf{E}_{oy} and \mathbf{E}_{oz} .

For an unpolarized incident X-ray beam from an X-ray tube, each photon is polarized in a fixed direction in the \mathbf{y} - \mathbf{z} plane. Still, on average, the electric field is taken to be evenly distributed in the $\hat{\mathbf{y}}$ direction and in the $\hat{\mathbf{z}}$ direction. Thus, each vector component equals half of the total electric field. Recall that the magnitude of the field dotted with its complex conjugate is proportional to the intensity of the wave.

$$I_o \propto |\bar{E}_0 \cdot \bar{E}_0^*| = |E_{oy}|^2 + |E_{oz}|^2 \quad (9.2)$$

For an unpolarized beam, it follows that the intensity of X-rays polarized in the $\hat{\mathbf{y}}$ direction is equal to the intensity polarized in the $\hat{\mathbf{z}}$ direction and half of the total intensity.

$$|E_{oy}|^2 = |E_{oz}|^2 = \frac{1}{2}|E_o|^2 \rightarrow I_{oy} = I_{oz} = \frac{1}{2}I_o \quad (9.3)$$

The following procedure determines the scattered intensity I_e at the position P in the \mathbf{x} - \mathbf{z} scattering plane in Figure 9.1 above. Point P is displaced by \bar{r} from the electron at O.

We first consider the σ **polarization case**, where the electric field is totally polarized in the $\hat{\mathbf{y}}$ direction and, therefore, perpendicular to the \mathbf{x} - \mathbf{z} scattering plane.

$\bar{E}_0 = E_o \hat{\mathbf{y}}$ (σ **polarization case**, $\bar{E}_0 \perp$ scattering plane)

Here, $\alpha = \frac{\pi}{2}$, thus yielding maximum intensity as expected by the $\sin^2 \alpha$ factor in the classical Thomson scattering equation.

$$I_e^\perp = I_o \frac{r_e^2}{R^2} \quad (9.4)$$

Secondly, we consider the π **polarization case**, where the electric field is totally polarized along the $\hat{\mathbf{z}}$ direction and parallel to the \mathbf{x} - \mathbf{z} scattering plane:

$\bar{E}_0 = E_o \hat{\mathbf{z}}$ (π **polarization case**, $\bar{E}_0 \parallel$ scattering plane)

Here, $\alpha = \frac{\pi}{2} - 2\theta$, yielding an intensity that varies depending on the scattering angle 2θ .

$$I_e^\parallel = I_0 \frac{r_e^2}{R^2} \cos^2 2\theta$$

Figure 9.2 below plots this $\cos^2 2\theta$ relationship with a varying 2θ value that is present in the intensity function for the π polarization case.

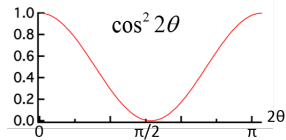


Figure 9.2: Scattered intensity dependence on scattering angle for π -polarization case.

Unpolarized X-rays, e.g., characteristic radiation from an X-ray tube, can be treated as being half σ -polarized and half π -polarized. To obtain the total scattered intensity at P, sum the intensities of the σ polarized and π polarized components.

$$I_e = \frac{1}{2} I_e^\perp + \frac{1}{2} I_e^\parallel = I_0 \frac{r_e^2}{R^2} \left(\frac{1+\cos^2 2\theta}{2} \right)$$

↑polarization factor

Note that this relationship is independent of λ and dependent on $\frac{1}{R^2}$.

At $2\theta = 0$ (forward scattering) and $R=1$ cm

$\frac{I_e}{I_0} = \frac{r_e^2}{R^2} = (2.818 \times 10^{-13})^2 = 7.94 \times 10^{-26}$ ← very weak, an extremely small fraction of the incident beam's intensity

At $2\theta = \frac{\pi}{2}$

$\frac{I_e}{I_0} = \frac{1}{2} \left(\frac{I_e}{I_0} \right)_{2\theta=0}$ only σ polarized X-rays are scattered in the $2\theta = \frac{\pi}{2}$ direction.

9.1.1 Barkla

British researcher Charles Barkla performed a double scattering experiment to prove that scattering at $\frac{\pi}{2}$ produces a polarized beam. In this experiment, as shown in Figure 9.3 below, unpolarized X-rays, along the \hat{x} -direction, scatter from a small particle at O. A very small fraction of those scattered X-rays travel along $-\hat{z}$ direction and rescatter from another small particle at P. To prove that this 90° scattered beam along the $-\hat{z}$ direction is polarized in the \hat{y} -direction, an X-ray photon counting detector at Q is rotated around the \hat{z} -axis in the \hat{x}' - \hat{y}' plane. As shown in Figure ??, Barkla measured the scattered intensity as a function of angle ϕ and found that it varied as $\cos^2 \phi$. The intensity pattern of this rescattered beam matches the intensity pattern expected for incident X-rays polarized in the \hat{y} -direction, thus proving that $\frac{\pi}{2}$ scattering produces a polarized beam. Essentially, in this experiment, we have an X-ray polarizer at O and an X-ray polarimeter at Q.

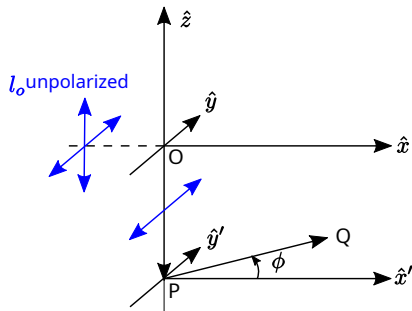


Figure 9.3: Barkla's experiment to prove that scattering at 90° produces a polarized X-ray beam.

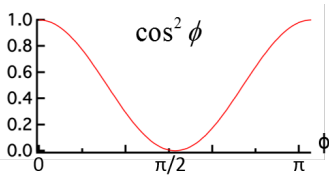


Figure 9.4: Referring to the previous figure, this is the normalized scattered intensity at Q as a function of ϕ .

9.2 Thomson Scattering by two electrons

Recall the Thomson scattered intensity from a free electron:

$$I_e = I_0 \frac{r_e^2}{R^2} \left(\frac{1 + \cos^2 2\theta}{2} \right) \text{ unpolarized X-ray beam}$$

$$r_e = 2.818 \times 10^{-13} \text{ cm}$$

Note: λ independent & $\frac{1}{R^2}$ dependent

As shown in Figure 9.5 below, we can define the following parameters:

\bar{S}_0 \equiv incident direction unit vector

\bar{S} \equiv scattered direction unit vector

2θ = scattering angle

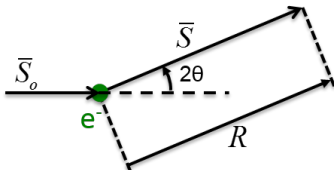


Figure 9.5: Define $\bar{S}_0, \bar{S}, 2\theta$

Reminiscent of Young's 2-slit interference experiment, let's now consider the scattering from 2 free electrons, one at the origin and one at \bar{r} , as shown in Figure 9.6 below.

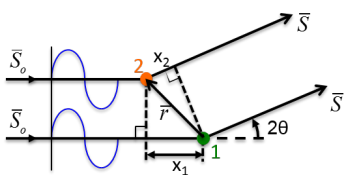


Figure 9.6: Scattering of a plane wave from two free electrons.

Due to the path-length difference, $|x_1| - |x_2|$ the two scattered waves will have a phase difference $\delta = (x_1 + x_2) \frac{2\pi}{\lambda}$ in the far field.

Where $x_1 = \bar{r} \cdot \bar{S}_0$, and $x_2 = \bar{r} \cdot \bar{S}$

$$\text{Equivalently, } \delta = -\frac{2\pi}{\lambda}(\bar{S} - \bar{S}_0) \cdot \bar{r}$$

Note that in the forward scattering direction, as shown in Figure 9.7 below $\bar{S} = \bar{S}_0$, the scattering angle $2\theta = 0$ and, therefore, the phase difference $\delta = 0$. This implies that for an incident plane wave scattering from a collection of electrons, the scattered X-rays in the forward direction are all in phase and, therefore, have perfect constructive interference.

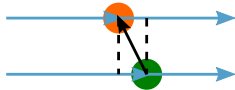


Figure 9.7: Scattering of a plane wave from two electrons in the forward direction.

Referring again to Figure 9.6, the scattered E-field traveling waves from each electron at R in the \bar{S} direction are represented by the following equations:

$$\bar{E}_1(R, t) = \bar{E}_1 \cos \left[\frac{2\pi R}{\lambda} - \omega t \right] = \bar{E}_1 \cos \phi \quad (9.5)$$

$$\bar{E}_2(R, t) = \bar{E}_2 \cos \left[\frac{2\pi R}{\lambda} + \delta - \omega t \right] = \bar{E}_2 \cos(\phi + \delta) \quad (9.6)$$

Note that the second electron's scattered wave has a phase shift δ added into its cosine function. Since the detector is at a distance much greater than the distance between the two electrons, the amplitudes of the electric fields scattered from both electrons are taken to be equal. Furthermore, the cosine factors of the equations may be converted using Euler's formula.

$$\begin{aligned} E_2 &= E_1 \leftarrow R \gg r \\ \text{use } e^{i\phi} &= \cos \phi + i \sin \phi \\ e^{i(\phi+\delta)} &= e^{i\phi} e^{i\delta} \end{aligned}$$

At the detector, the total scattered field equals the sum of the scattered E-fields from each electron. Note that Euler's formula is used instead of the cosine terms in the first line below. The intensity is determined by dotting the total field, labeled $\bar{\epsilon}$ below, by its complex conjugate $\bar{\epsilon}^*$. Recall that the scattered intensity from one electron was simply E^2 . Now for 2 electrons, this E^2 is modified to account for the fact that the electrons are at two different positions and a certain 2θ angle that leads to scattered waves with phase difference δ . Notice that if $\delta = 0, 2\pi$ or $2n\pi$, then the two scattered waves are perfectly in phase and produce four times the scattered intensity as compared to scattering from a single electron. On the other hand, if δ is an odd multiple of π , or $(2n+1)\pi$, then the two scattered waves are completely out of phase, and no intensity is detected. Of course, there are instances in between, such as $\delta = \frac{\pi}{2}$, in which the intensity is in between these two extremes.

$$\bar{\epsilon}(\bar{R}, t) = \bar{E}_1 e^{i\phi} + \bar{E}_2 e^{i\phi} e^{i\delta} = \bar{E}_1 e^{i\phi} (1 + e^{i\delta}) \quad (9.7)$$

$$I \propto |\bar{\epsilon}|^2 = \bar{\epsilon} \cdot \bar{\epsilon}^* = E_1^2(1 + e^{i\delta})(1 + e^{-i\delta}) = E_1^2(2 + e^{i\delta} + e^{-i\delta}) = 2E_1^2(1 + \cos\delta) \quad (9.8)$$

$$|\bar{\epsilon}|^2 = 4E_1^2 \text{ for } \delta = 0, 2\pi, \dots \rightarrow x_1 + x_2 = -\bar{r} \cdot (\bar{S} - \bar{S}_o) = n\lambda$$

$$|\bar{\epsilon}|^2 = 0 \text{ for } \delta = \pi, 3\pi, \dots$$

$$|\bar{\epsilon}|^2 = 2E_1^2 \text{ for } \delta = \pm\frac{\pi}{2}, \dots$$

Therefore, due to interfering waves, the scattered intensity from two electrons increases from 0 to 4x that from one electron.

9.2.1 Thomson scattering from N electrons

The total E-field is the sum of the fields generated by each of the two electrons.

$$\bar{\epsilon}_{Total} = \bar{\epsilon}_1 + \bar{\epsilon}_2 = e^{i\phi}(\bar{E}_1 e^{i\delta_1} + \bar{E}_2 e^{i\delta_2}) \quad (9.9)$$

$$\text{where } \phi = \frac{2\pi R}{\lambda} - \omega t .$$

Here, we are setting the phase of scattered wave 1 to zero: $\delta_1 = 0$

Where R is the distance to the detector, and r is the distance between the electrons. Since $R \gg r \rightarrow E_2 = E_1 = E$

In general, for N free electrons, the total electric field generated is the sum of the scattered E-fields from all of the electrons. This is based on the superposition principle, in which the sum of the individual forces yields an equivalent total force. The detector “sees” the sum of all of these individual electric force fields, having equal amplitude but individual phase factors resulting from varying positions and 2θ angles. Recall that only in the forward direction will each phase be equal to zero.

$$\bar{\epsilon}_{tot} = \sum_{n=1}^N \bar{\epsilon}_n = \bar{E}_e e^{i\phi} \sum_n e^{i\delta_n} \quad (9.10)$$

Thus, the total intensity is equal to the square of the magnitude of this total electric field. In the equation below, the first factor before the summation equals the scattered intensity from one electron. This is abbreviated as I_e seen in the second line below.

$$I_{tot} \propto |\bar{\epsilon}_{tot}|^2 = E_e^2 \left| \sum_{n=1}^N e^{i\delta_n} \right|^2 = \frac{r_e^2}{R^2} \left(\frac{1 + \cos 2\theta}{2} \right) \left| \sum_{n=1}^N e^{i\delta_n} \right|^2 \quad (9.11)$$

$$I_{tot} = I_e \left| \sum_{n=1}^N e^{i\delta_n} \right|^2 \quad (9.12)$$

If the scattered direction $2\theta = 0$, then the total intensity will be the intensity of one electron times N^2 , where N is the total number of electrons. The intensity of the scattered wave is N^2 times, rather than N times, the scattered intensity from an individual electron because of the interference of coherently scattered waves (waves

of equal wavelength). Furthermore, if the 2θ angle is not zero, then the intensity is less than N^2 .

$$2\theta = 0 \rightarrow \frac{I_{tot}}{I_e} = N^2, 2\theta \neq 0 \rightarrow \frac{I_{tot}}{I_e} \leq N^2$$

Note that if the scattered waves have slightly different wavelengths $\lambda_n > \lambda_0$, this is called modified or incoherent scattering. The waves will not interfere, and the intensity will be affected by a factor of N as opposed to N^2 in classical Thomson scattering. $\rightarrow (I_{tot})_{mod} = N(I_e)_{mod}$. This incoherent scattering, which competes with coherent scattering, will be discussed in the next section.

9.2.2 X-ray Scattering from an atom with Z electrons in spherically symmetrical distributions

According to quantum mechanics, the electrons involved in scattering are not at discrete points in space but have a probability distribution that describes their location around an atom's nucleus. This probability of finding an electron in a given shell is given by a wave function. This is pictorially represented by an electron cloud rather than set electron locations, as illustrated in Figure 9.8 below. The electron density in a given atom, therefore, is the sum of the individual probability densities of its Z electrons. Thus, the sum is equal to the sum of each electron's wave function multiplied by the wave function's complex conjugate, as shown below.

$$\rho_{atom} = \sum_1^Z \rho_e = \sum \psi_e \psi_e^* \quad (9.13)$$

H-like wave function $\rho_e = |\psi_e|^2$.

9.2.3 Defining Atomic Scattering Factor

In Figure 9.8 below, an incident X-ray plane wave, represented by the blue arrow pointing to the right and positioned to the left of the red electron cloud, is incident on some differential volume at position \bar{r} with electron density $\rho(\bar{r})$.

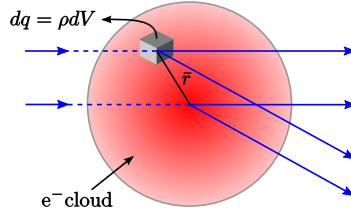


Figure 9.8: Scattering from e^- cloud

The **atomic scattering factor** f , is defined as the ratio of the magnitude of the scattered E-field amplitude from an atom as compared to the scattered E-field amplitude from one single electron according to Thomson scattering.

$$f = \frac{E_{atom}}{E_{e^-}} \quad (9.14)$$

The atomic scattering factor is calculated using the following integral: It sums the scattering contributions from each differential volume while accounting for phase differences ($e^{i\delta} = e^{i\frac{2\pi}{\lambda}(\bar{S}-\bar{S}_0)\cdot\bar{r}}$) over the entire atomic volume.

$$f = \int_{atom} \rho(\bar{r}) e^{i\frac{2\pi}{\lambda}(\bar{S}-\bar{S}_0)\cdot\bar{r}} dV \quad (9.15)$$

Recall that for N electrons, the magnitude of the electric field scattered in the forward direction should equal N, since there is no phase shift between the scattered waves. This is consistent with the formula above, as the $e^{i\delta}$ factor, where δ is the phase shift, goes to one, and therefore $f = Z$ at $2\theta = 0$. The atomic scattering factor is dictated by the 2θ scattering angle describing the phase shift between scattered waves from multiple points within the electron cloud.

Essentially, as waves scattered by the atom's electrons become more out of phase (i.e., as 2θ increases), the atomic scattering factor decreases (f decreases) due to the partially destructive interference in scattered waves. In addition to the 2θ angle, the atomic scattering factor depends on the wavelength. At a fixed 2θ value, for instance, a decrease in wavelength will make pathlength differences larger relative to the wavelength, thus causing a greater degree of destructive interference between scattered waves.

9.2.4 Calculating the Atomic Scattering Factor

Figure 9.9 below illustrates an incident X-ray plane wave in the \bar{S}_0 direction, interacting with an atom at O and scattering in the \bar{S} direction. The following formula may be used to calculate the amplitude of the scattering for one electron: $f_e = \int \rho_e e^{i\frac{2\pi}{\lambda}(\bar{S}-\bar{S}_0)\cdot\bar{r}} dV$

Here, ρ_e describes the electron distribution, and the exponential factor calculates the relative phase of the scattered wave from different positions \bar{r} within the electron cloud. We will assume spherical symmetry $\rightarrow \rho(\bar{r}) = \rho(r)$.

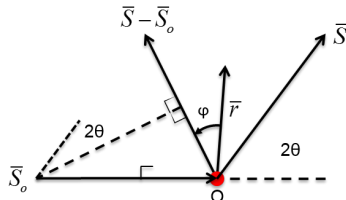


Figure 9.9: Vectors and angles used for calculating the atomic scattering factor by integration in spherical coordinates.

$$(\bar{S} - \bar{S}_0) \cdot \bar{r} = |\bar{S} - \bar{S}_0| |\bar{r}| \cos \phi = 2 \sin \theta r \cos \phi$$

Note: $\int_0^\pi e^{iqr \cos \phi} \sin \phi d\phi$ can be integrated by parts.

$$\text{Let } u = qr \cos \phi \rightarrow \frac{du}{d\phi} = -qr \sin \phi$$

$$\phi = 0 \rightarrow u = qr$$

$$\phi = \pi \rightarrow u = -qr$$

$$\begin{aligned} \Rightarrow \int_0^\pi e^{iqr\cos\phi} \sin\phi d\phi &= -\frac{1}{qr} \int_{-qr}^{qr} e^{iu} du \\ &= -\frac{1}{qr} \left[\int_{-qr}^{qr} \cos u du + i \int_{-qr}^{qr} \sin u du \right] = -\frac{2\sin(qr)}{qr} \end{aligned}$$

Let $q = 4\pi \sin \theta / \lambda$ (Azaroff $q \equiv k$)

$$f_e = 2\pi \int_{r=0}^{\infty} \int_{\phi=0}^{\pi} \rho(r) e^{iqr\cos\phi} r^2 \sin\phi d\phi dr \quad (9.16)$$

$$f_e = 4\pi \int_{r=0}^{\infty} \rho(r) r^2 \frac{\sin qr}{qr} dr \quad (9.17)$$

for a spherically symmetrical electron cloud distribution.

Example: Lithium

Suppose that the subshell electron densities for a neutral lithium atom of atomic number $Z=3$ and electron configuration $(1s^2 2s^1)$ are given by the following hydrogen-like expression:

$$\rho_e(r) = \frac{e^{(-2r/a)}}{\pi a^2}, \quad (9.18)$$

where for the two K electrons, $a_K = 0.20\text{\AA}$, and for the one L electron, $a_L = 1.60\text{\AA}$

The scattering factor for each electron may be calculated from the following equation:

$$f_e = 4\pi \int_0^{\infty} \frac{e^{-(2r/a)}}{\pi a^2} r^2 \frac{\sin qr}{qr} dr = \frac{1}{\left[1 + \left(\frac{2\pi a \sin \theta}{\lambda}\right)^2\right]^2} \quad (9.19)$$

Furthermore, lithium's total atomic scattering factor is obtained by summing the scattering factors of the two electrons in its K shell and the one electron in its L shell. $f_{Li} = 2f_{eK} + f_{eL}$. Note that the electron scattering factors for lithium are decreasing as a function of $\frac{\sin \theta}{\lambda} = \frac{1}{2d}$ in Figure 9.11 below. This describes the intra-atomic interference effect.

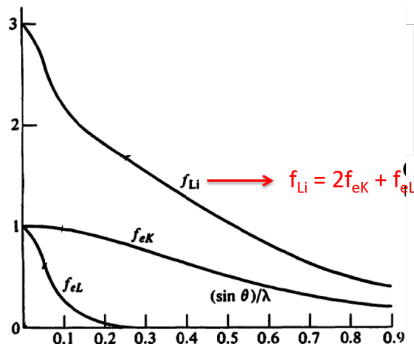


Figure 9.10: Li atomic scattering factor as a function of $\frac{\sin \theta}{\lambda}$.

Fortunately, we do not need to make this laborious quantum calculation to analyze X-ray scattering data. The atomic scattering factors for all atomic and many ionic species are tabulated as a function of $\frac{\sin \theta}{\lambda}$ in the International Tables for Crystallography Volume C [?] and in Cullity and Stock [?] Appendix 10. Or one can go to the website <https://lampx.tugraz.at/hadley/ss1/crystaldiffraction/atomicformfactors/formfactors.php> to find the parameterized formula for calculating f as a function of $q = \frac{4\pi \sin \theta}{\lambda}$.

9.3 Compton Scattering

Compton scattering, also known as modified or incoherent scattering, is the quantum effect in which scattered waves have lost energy due to inelastic scattering and, therefore, have a slightly larger wavelength than their incident X-ray wavelength. This occurs when X-rays scatter from loosely bound electrons and may be explained by considering the incident beam to be comprised of a stream of photons of energy $\hbar\omega_0$, as illustrated in Figure 9.11 below. When one of these photons strikes a loosely bound electron that is initially at rest, energy and momentum are transferred from the photon to the electron. Due to this transfer of energy and momentum, the inelastically scattered X-ray photon has lower energy and, therefore, a larger wavelength, thus making this scattering incoherent and preventing interference effects.

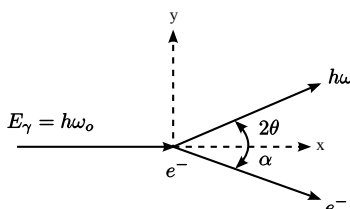


Figure 9.11: Compton Scattering diagram showing incident photon traveling in x-direction, Compton scattered photon in x-y plane at angle 2θ , and Compton scattered electron in x-y plane at angle α .

The following equations combine the laws of conservation of energy and momentum in the photon-electron collision to yield a function of the change in wavelength of

the Compton-scattered X-ray with respect to the scattering angle. 2θ . Note that the theory of Compton scattering expresses the energy and momentum of the photons and electrons in relativistic values. These relativistic values are necessary because the scattered photons are massless, and the energy transferred to the electron is measured relative to its rest energy.

Conservation of energy:

$$\hbar\omega_0 = \hbar\omega + \frac{1}{2}m_e v_e^2 \text{ assuming initial } e^- \text{ at rest}$$

Conservation of momentum

$$\frac{\hbar\omega_0}{c} = \frac{\hbar\omega}{c} \cos 2\theta + m_e v_e \cos \alpha \leftarrow x \text{ direction}$$

$$0 = \frac{\hbar\omega}{c} \sin 2\theta - m_e v_e \sin \alpha \leftarrow y \text{ direction}$$

$$\text{Eliminate } \alpha \text{ and } v_e, \lambda = \frac{2\pi c}{\omega}, \text{ and } \hbar = \frac{h}{2\pi}$$

$$\lambda - \lambda_0 = \Delta\lambda = \frac{h}{m_e c} (1 - \cos 2\theta)$$

$$\Delta\lambda(\text{\AA}) = 0.0243(1 - \cos 2\theta)$$

Note that the change in wavelength in the forward direction is 0, and the change in wavelength in the backward direction $2\theta = 180^\circ$ is about 0.05 \AA .

$$\Delta\lambda = 0 \text{ at } 2\theta = 0^\circ$$

$$\Delta\lambda = 0.0486 \text{ \AA} \text{ at } 2\theta = 180^\circ$$

The change in wavelength may be related to the change in energy by the following equations:

$$\lambda - \lambda_0 = \Delta\lambda = \frac{h}{m_e c} (1 - \cos 2\theta) \quad \Delta E = \frac{E_\gamma^2 (1 - \cos 2\theta)}{m_e c^2 + E_\gamma (1 - \cos 2\theta)}$$

where $m_e c^2 = 511 \text{ keV}$ (electron rest mass energy)

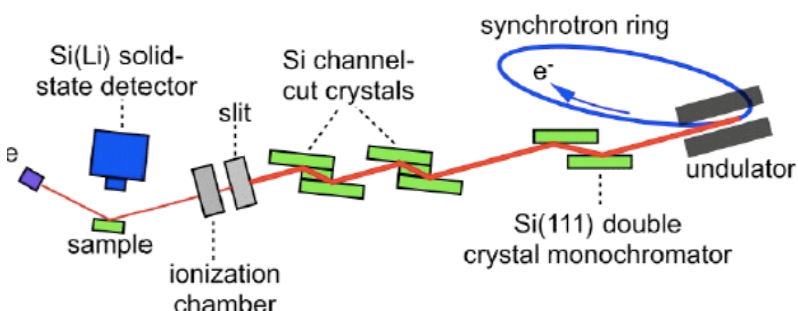


Figure 9.12: Synchrotron undulator setup for monochromatic X-ray beam scattering from the sample with an energy-dispersive solid-state detector collecting the X-ray spectrum.

Ex: If $2\theta = 90^\circ$ $E_\gamma = 18.5 \text{ keV}$ $\Delta E = 0.65 \text{ keV}$

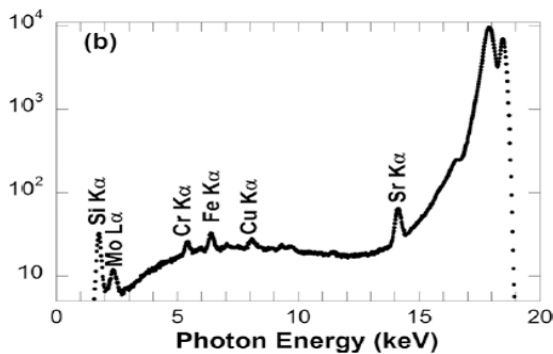


Figure 9.13: The X-ray spectrum collected by the solid-state detector in the previous figure. The sample is 1/2 monolayer of Sr on Si(001). The highest energy peak at 18.5 keV is from elastically scattered X-rays. The peak 0.65 keV below that in energy is from Compton scattered X-rays.

Note that Compton scattering will not occur if the change in energy is less than the binding energy for the electron. i.e., $\Delta E < E_B$.

For hydrogen, a one-electron atom, the total intensity according to the Thomson scattering equation is equal to the summed intensities of the modified (Compton) and unmodified scattered wave.

$$I_e = I_{unmod} + I_{mod} \quad (9.20)$$

$$I_e = I_0 \left(\frac{r_e}{R}\right)^2 \sin^2 \alpha \rightarrow \text{Thomson}$$

$$I_{unmod} = \text{Coherent} \rightarrow \text{Bragg} \quad I_{mod} = \text{Incoherent} \rightarrow \text{Compton}$$

$$1 = \frac{I_{unmod}}{I_e} + \frac{I_{mod}}{I_e} \text{ in electron units}$$

$$1 = f_e^2 + (I_{eu})_{mod} \Rightarrow (I_{eu})_{mod} = 1 - f_e^2$$

The modified, or Compton scattering, and the unmodified, vary in opposite ways with respect to $\frac{\sin \theta}{\lambda}$, as shown in Figure 9.14 below.

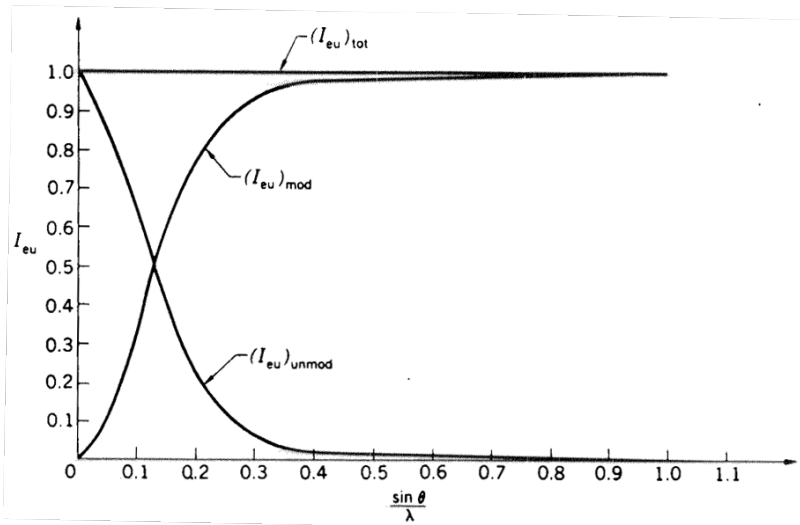


Figure 9.14: Modified, unmodified, and total scattered intensities from a hydrogen atom with 1 electron.

The scattered intensity for atoms with atomic numbers greater than one, such as lithium ($Z=3$), varies from the simple hydrogen model shown above. Again, the modified scattering intensity for each electron is given by $1 - f_e^2$. Recall that no interference effects can occur for incoherent scattering due to wavelength variations after collisions; thus, the total incoherent scattering intensity is simply given by the sum of the incoherent scattering intensities of the individual electrons.

$$(I_{eu})_{mod} = 2(1 - f_e^2)_K + (1 - f_e^2)_L = Z - \sum_n (f_e)_n^2 \quad (9.21)$$

Furthermore, the unmodified scattering intensity from an individual atom is equal to the square of the atomic scattering factor since $f = \frac{E_{atom}}{E_e}$, and the intensity is the square of the magnitude of the electric field. Recall that for coherently scattered waves, the most efficient scattering is in the forward direction, where $f = Z$. Since the unmodified intensity varies as f^2 , the intensity in electron units (eu) will be less than or equal to Z^2 . Furthermore, the modified scattering intensity will be less than or equal to the atomic number of a given element. For lighter elements and short wavelengths, the modified scattered intensity becomes more significant relative to the total scattered intensity.

$$(I_{eu})_{unmod} = f^2 \leq Z^2 \quad (9.22)$$

$$(I_{eu})_{mod} \leq Z \leftarrow \text{significant for low } Z \text{ and low } \lambda$$

Figure 9.15 below demonstrates the relationship between scattered intensities and $\frac{\sin \theta}{\lambda}$ for atoms with $Z > 1$.

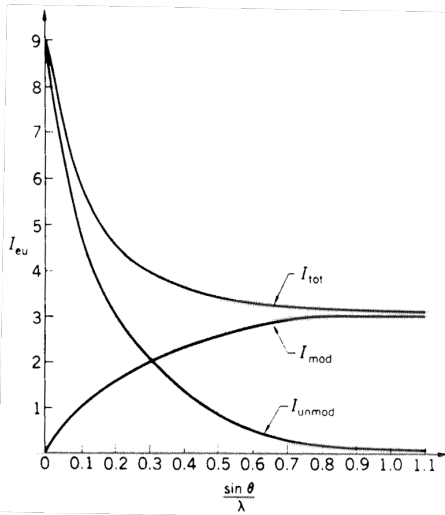


Figure 9.15: Modified, unmodified, and total scattered intensities from an atom with $Z > 1$. This is the case for Li with $Z=3$.

9.3.1 Anomalous Dispersion

Classical Thomson scattering, which treats electrons as being free (unbound), has no wavelength dependence. However, there is a quantum effect that causes the atomic scattering factor to be affected by the energy of the photon, which translates into a λ dependence of f .

Anomalous dispersion is a phenomenon that occurs when the X-ray's photon energy is close to the energy of the absorption edge for a given element. In other words, the frequency of the incoming photon is close to the natural frequency for a bound electron within the atom, causing a resonance effect that changes the scattered intensity. When this effect is considered, the following wavelength-dependent formula gives the atomic scattering factor:

$$f = f_o \left(\frac{\sin \theta}{\lambda} \right) + \Delta f'(\lambda) + i \Delta f''(\lambda) \quad (9.23)$$

$f_o \rightarrow$ Atomic form factor

$$f_o(\bar{q}) = \int_{atom} \rho(\bar{r}) e^{i\bar{q} \cdot \bar{r}} d\bar{r} \quad (9.24)$$

scattering factor is Fourier transform of atom's electron distribution.

$$\bar{q} = \frac{2\pi}{\lambda} (\bar{S} - \bar{S}_o) \quad (9.25)$$

is the scattering vector with magnitude

$$q = \frac{4\pi \sin \theta}{\lambda} \quad (9.26)$$

The f_o term is what was previously taken to be the atomic scattering factor, and the $\Delta f'$ and $i\Delta f''$ correction terms account for the anomalous dispersion effect. The latter two terms depend on the element and the wavelength of the incident X-ray.

If the frequency of the incident X-ray beam is much greater than the natural resonance frequency of the electron (i.e., if the energy of the X-ray is much greater than the binding energy for a K shell electron), the scattered wave will be π out of phase with respect to the incident wave, similar to the π phase lag in Thomson scattering by free electrons. However, if the energy of the incident beam is close to the electron's binding energy, the scattered wave will deviate from this π phase shift with respect to the incident wave. If the incident photon energy is near the K-edge of an atom, the in-phase waves scattered from the K electrons destructively interfere with the out-of-phase X-rays scattered from outer electrons.

9.3.2 Honl's Correction Factors

As shown in Figure 9.16 below, the Δf real component is 180° out of phase with the normally scattered radiation, f_o , and affects the amplitude of the wave. Furthermore, the $\Delta f''$ imaginary component is 90° out of phase with respect to f_o and affects the phase of the scattered wave from the atom.

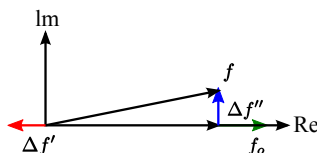


Figure 9.16: Honl's correction terms as viewed in the complex plane.

Figure 9.17 below demonstrates the effect of increasing energy on the $\Delta f'$ and $\Delta f''$ corrections. Note that the $\Delta f''$ imaginary component becomes highly positive, slightly above the absorption edge. Conversely, the real $\Delta f'$ component becomes largely negative close to the absorption edge. This proximity to the absorption edge indicates that the frequency of the incident wave is close to the electron's natural frequency. Since the absorption edge is characteristic of a given element, the correction factors in $f = f_o + \Delta f' + i\Delta f''$ can give chemical sensitivity to the X-ray scattering process. These $f_o, \Delta f', \Delta f''$ terms are tabulated in the International Tables for Crystallography[?]. One can go online to https://henke.lbl.gov/optical_constants/asf.html and find the energy dependence for the real and imaginary parts of the atomic scattering factor in the forward direction. In addition, since the intensity is proportional to ff^* - the scattering factor times its complex conjugate - the scattered intensity may be manipulated by using a synchrotron radiation source with a tunable E_γ , or wavelength of the incident X-ray beam.

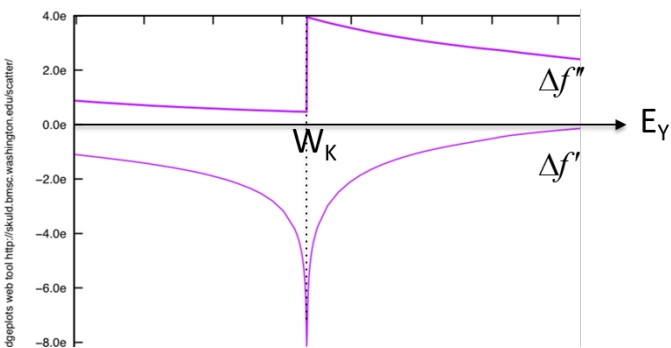


Figure 9.17: Anomalous dispersion corrections to the atomic scattering factor as a function of incident X-ray energy near the binding energy for the 2 K electrons.

If the incident X-ray is not close to the absorption edge for an element, i.e., E_K or E_L , etc., then the correction factors will be negligible with respect to f_o . In this course, we will ignore anomalous dispersion effects unless specifically stated.

9.3.3 X-ray Scattering by Many Atoms

For one atom, the scattered E-field amplitude is

$E_a = fE_e = fE_o \frac{r_e}{R} \sin \alpha \sin \alpha = 1$ for σ -polarized case; $\sin \alpha = \cos 2\theta$ for π -polarized case

Elastic Coherent Scattering $\rightarrow f$

$$r_e = 2.818 \times 10^{-13} \text{ cm}$$

$$f = f_o \left(\frac{\sin \theta}{\lambda} \right) \rightarrow \Delta f' = \Delta f'' = 0$$

$$f_o(0) = ?$$

For unpolarized \bar{E}_o , $E_{ox} = E_{oz} = \frac{E_o}{\sqrt{2}}$

10 Kinematical Scattering Theory

Based on the superposition principle, kinematical scattering theory adds up the scattered E-field waves and ignores the possibility of these scattered waves rescattering before reaching the detector. Because X-ray scattering from an atom is such a weak interaction, this simplification accurately describes scattering from collections of atoms, including the case when they are assembled into a single crystal, as long as it is small compared to the extinction length, measured in microns. Dynamical scattering theory, which solves Maxwell's equations for a periodic electron density, is the rigorous but more difficult to apply theory that works for small and large perfect single crystals. We will use kinematical scattering theory.

We first consider the scattering of an incident plane wave by a collection of N atoms, as shown in Figure 10.1 below. Note that the incident direction is described by unit vector \bar{S}_0 and the scattered direction is described by unit vector \bar{S} .

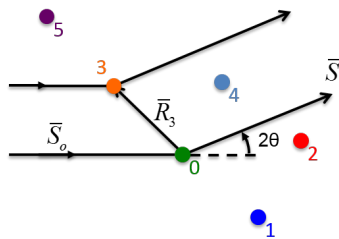


Figure 10.1: Scattering from a collection of atoms. The scattered waves in direction \bar{S} are considered parallel since the detector is very much further away than the interatomic distances R_m .

If we consider the scattering from atoms “0” and “3,” their scattered wave vectors will be parallel and of the same wavelength, but the scattered waves will in general not be in phase with each other due to a separation between the two atoms, indicated by \bar{R}_3 . The difference between the incident unit vector, \bar{S}_0 , and the scattered unit vector, \bar{S} , dotted with the distance between the two atoms yields this extra path length, as shown in the following expression:

$$\text{Extra path length } \bar{R}_m \cdot (\bar{S} - \bar{S}_0)$$

We now introduce the **scattering vector**, which is a measure of spatial frequency.

$$\bar{Q} = \frac{\bar{S} - \bar{S}_0}{\lambda} = \bar{k} - \bar{k}_0, \quad (10.1)$$

$\bar{k}_0 = \bar{S}_0/\lambda$ is the incident wave vector and $\bar{k} = \bar{S}/\lambda$ is the scattered wave vector. The magnitude of $Q = 2\sin\theta/\lambda$, where θ is one-half of the scattering angle 2θ . As an alternative, we will sometimes use $\bar{q} = 2\pi\bar{Q}$.

$\bar{Q} \cdot \bar{R}_m$ is the path length difference in units of the wavelength and

$2\pi\bar{Q} \cdot \bar{R}_m$ is the phase of the wave scattered by the m^{th} atom relative to the wave scattered by the atom at the origin 0.

When $\bar{Q} \cdot \bar{R}_m = n$, there is perfect constructive interference between the waves scattered by m^{th} atom and the atom at the origin.

10.1 Scattering from N atoms

The following equation sums each individual E-field to get the total scattered E-field by N atoms. The exponential factor keeps track of the phase of each wave for all of the atoms:

$$\frac{E_{Total}}{E_e} = \sum_{m=0}^{N-1} f_m e^{2\pi i \bar{Q} \cdot \bar{R}_m} \quad (10.2)$$

Note that f_m is the amplitude of the scattered wave from the m^{th} atom, which will be the same for all atoms of the same type and distinct for different atoms. The summed complex fields are normalized by the scattering amplitude that is expected from one electron according to classical Thomson scattering- $\frac{E_{Total}}{E_e}$.

$f_m = f$, If all atoms are the same type, otherwise they can be different.

10.1.1 Scattered Intensity from N Atoms

The scattered intensity in electron units, or the scattered intensity of N atoms as compared to the scattered intensity of a single electron is given by the following equation:

$$I_{(eu)} = \left| \frac{E_{Total}}{E_e} \right|^2 = \left[\sum_{m=0}^{N-1} f_m e^{2\pi i \bar{Q} \cdot \bar{R}_m} \right] \left[\sum_{m=0}^{N-1} f_m e^{-2\pi i \bar{Q} \cdot \bar{R}_m} \right] \quad (10.3)$$

Here, the normalized total electric field equation is multiplied by its complex conjugate to yield the intensity. This is equivalent to the following double summation.

$$= \sum_{m=0}^{N-1} \sum_{n=0}^{N-1} f_m f_n e^{2\pi i \bar{Q} \cdot (\bar{R}_m - \bar{R}_n)} \quad (10.4)$$

In the following vector diagram for $\bar{R}_m - \bar{R}_n$, the origin is conveniently chosen to be at the location of the green “0” atom. The difference of \bar{R}_3 and \bar{R}_4 gives the inter-atomic distance between atoms 3 and 4, labeled \bar{r}_{34} .

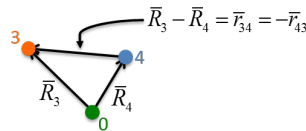


Figure 10.2: $\bar{R}_m - \bar{R}_n$

Now, the \bar{r}_{mn} inter-atomic spacing vector replaces $\bar{R}_m - \bar{R}_n$ and $\bar{r}_{mn} = -\bar{r}_{nm}$.

$$\frac{I_{Total}}{I_e} = I_{eu} = \sum_{m=0}^{N-1} \sum_{n=0}^{N-1} f_m f_n e^{2\pi i \bar{Q} \cdot \bar{r}_{mn}} \quad (10.5)$$

From this double summation, there are a total of N^2 terms.

There are N terms of the type: f_m^2 . These terms, in which $m=n$, are the scattered intensities from isolated atoms, in which no interatomic interference effects occur. Here $\bar{r}_{mn} = 0$, and therefore $e^{2\pi i \bar{Q} \cdot \bar{r}_{mn}} = 1$.

For terms where $m \neq n$, there are $\frac{N(N-1)}{2}$ interatomic interference effect terms of the type: $f_m f_n (e^{2\pi i \bar{Q} \cdot \bar{r}_{mn}} + e^{-2\pi i \bar{Q} \cdot \bar{r}_{mn}}) = 2f_m f_n \cos(2\pi \bar{Q} \cdot \bar{r}_{mn})$

This is the general equation for kinematical scattering from any type of atomic collection - i.e. gas, solid, liquid, crystal, amorphous, etc. The following conditions are specific to gases, liquids and crystals:

- ◊ gases & liquids ← require proper averaging of $\bar{Q} \cdot \bar{r}_{mn}$ (angle averaging)
- ◊ crystals are periodic ← can use symmetry to reduce N^2 terms

10.2 Scattering from Small Crystal

Consider an X-ray plane wave (λ, \bar{S}_0) incident on a small crystal with a detector for coherently scattered X-rays at R and direction \bar{S} , as seen in Figure 10.3 below.

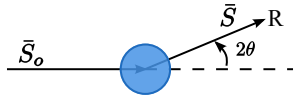


Figure 10.3: X-ray plane wave incident on crystal

The scattering vector determination is illustrated in Figure 10.4 below.

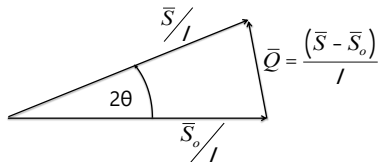


Figure 10.4: Scattering vector

The crystal contains $M = M_1 M_2 M_3$ unit cells. Each unit cell contains N atoms, which may or may not be of different types. Therefore, there are MN total atoms

in the crystal. Each atom in the unit cell is located by a vector \bar{r}_n , as shown in Figure 10.5 below. The atom is illustrated as a black dot in the unit cell block.

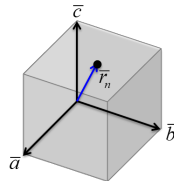


Figure 10.5: Atom located by \bar{r}_n in unit cell.

Assuming the crystal is parallelepiped, any unit cell's origin may be located by $m_1\bar{a} + m_2\bar{b} + m_3\bar{c}$, where $0 \leq m_i \leq M_i - 1$ is an integer. This is given by translational symmetry of unit cells. Therefore, any atom within the entire crystal is located by the following position vector:

$$\bar{R}_{m_1 m_2 m_3}^n = m_1\bar{a} + m_2\bar{b} + m_3\bar{c} + \bar{r}_n$$

$\nwarrow \uparrow \nearrow$
u.c. location
 \nwarrow
atom location in u.c.

The first three indices locate the specific unit cell containing the atom, using a translational symmetry operator. The \bar{r}_n term indicates the atom's position within that specific unit cell.

Figure 10.6 below illustrates the use of these four indices to locate an atom within a crystal. Note that the selected location of the origin is arbitrary.

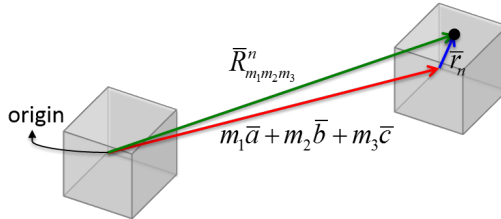


Figure 10.6: Location of an atom within the entire crystal by vector $(\bar{R}_{m_1 m_2 m_3}^n)$.

The scattered electric field from the entire crystal relative to the scattered field from a single electron is given by the following summation:

$$\frac{E_{Total}}{E_e} = \sum_{m_1=0}^{M_1-1} \sum_{m_2=0}^{M_2-1} \sum_{m_3=0}^{M_3-1} \sum_{n=0}^{N-1} f_n e^{2\pi i \bar{Q} \cdot \bar{R}_{m_1 m_2 m_3}^n} \quad (10.6)$$

$$= \sum_{m_1=0}^{M_1-1} \sum_{m_2=0}^{M_2-1} \sum_{m_3=0}^{M_3-1} \sum_{n=0}^{N-1} f_n e^{2\pi i \bar{Q} \cdot (m_1\bar{a} + m_2\bar{b} + m_3\bar{c})} e^{2\pi i \bar{Q} \cdot \bar{r}_n} \quad (10.7)$$

The four indices yield four summations.

The structure factor, given by the following summation, is the amplitude of the scattered electric field from the N atoms in a single unit cell:

$$F(\bar{Q}) = \sum_{n=0}^{N-1} f_n(Q) e^{2\pi i \bar{Q} \cdot \bar{r}_n} \quad (10.8)$$

This structure factor, which accounts for the internal interference effect from the N atoms within the unit cell, will be discussed later. For now, we will calculate the total scattered field from the M unit cells, which yields the following triple summation:

$$\frac{E_{Total}}{E_e} = F \sum_{m_1=0}^{M_1-1} e^{2\pi i \bar{Q} \cdot m_1 \bar{a}} \sum_{m_2=0}^{M_2-1} e^{2\pi i \bar{Q} \cdot m_2 \bar{b}} \sum_{m_3=0}^{M_3-1} e^{2\pi i \bar{Q} \cdot m_3 \bar{c}} \quad (10.9)$$

Consider the following simplification:

$$\sum_{m_1=0}^{M_1-1} e^{2\pi i \bar{Q} \cdot m_1 \bar{a}} = \sum_{m=0}^{M-1} x^m \quad (10.10)$$

This geometric series, with potentially a billion terms, converges to

$$= \frac{x^M - 1}{x - 1} = \frac{e^{2\pi i \bar{Q} \cdot \bar{a} M_1} - 1}{e^{2\pi i \bar{Q} \cdot \bar{a}} - 1} = \frac{e^{2i\eta M} - 1}{e^{2i\eta} - 1} \quad (10.11)$$

$$= \frac{e^{i\eta M} (e^{i\eta M} - e^{-i\eta M})}{e^{i\eta} (e^{i\eta} - e^{-i\eta})} = \frac{e^{i\eta M} \sin \eta M}{e^{i\eta} \sin \eta} \quad (10.12)$$

$$= \frac{\sin(\pi \bar{Q} \cdot \bar{a} M_1) e^{\pi i \bar{Q} \cdot \bar{a} M_1}}{\sin(\pi \bar{Q} \cdot \bar{a}) e^{\pi \bar{Q} \cdot \bar{a}}} = \frac{\sin(\pi \bar{Q} \cdot \bar{a} M_1)}{\sin(\pi \bar{Q} \cdot \bar{a})} e^{\pi i \bar{Q} \cdot \bar{a} (M_1 - 1)} \quad (10.13)$$

In one dimension, the total scattering intensity for M unit cells relative to the scattering intensity from one electron is given by the following:

$$\bar{I}_{eu} = \left| \frac{E_{total}}{E_e} \right|^2 = |F|^2 \frac{\sin^2(\pi \bar{Q} \cdot \bar{a} M)}{\sin^2(\pi \bar{Q} \cdot \bar{a})} \quad (10.14)$$

1D Interference Function

The intensity scattered from a single unit cell is given by the structure factor amplitude squared, and the second factor accounts for interference from M repeated unit cells.

In three dimensions, each factor is multiplied by its complex conjugate

$$\bar{I}_{eu} = \left| \frac{E_{total}}{E_e} \right|^2 = FF^* \left| \frac{e^{2\pi i \bar{Q} \cdot \bar{a} M_1} - 1}{e^{2\pi i \bar{Q} \cdot \bar{a}} - 1} \cdot \frac{e^{2\pi i \bar{Q} \cdot \bar{b} M_2} - 1}{e^{2\pi i \bar{Q} \cdot \bar{b}} - 1} \cdot \frac{e^{2\pi i \bar{Q} \cdot \bar{c} M_3} - 1}{e^{2\pi i \bar{Q} \cdot \bar{c}} - 1} \right|^2 \quad (10.15)$$

yielding the following three dimensional interference function. This is a rigorous theory for explaining X-ray scattering from a 3-D periodic lattice. Note that the three factors account for repeated unit cells along three axes.

$$\bar{I}_{eu} = |F|^2 \frac{\sin^2(M_1 \pi \bar{Q} \cdot \bar{a})}{\sin^2(\pi \bar{Q} \cdot \bar{a})} \cdot \frac{\sin^2(M_2 \pi \bar{Q} \cdot \bar{b})}{\sin^2(\pi \bar{Q} \cdot \bar{b})} \cdot \frac{\sin^2(M_3 \pi \bar{Q} \cdot \bar{c})}{\sin^2(\pi \bar{Q} \cdot \bar{c})} \quad (10.16)$$

3D Interference Function

Consider the 1D Interference Function, which has a mathematical form $\frac{\sin^2 Mx}{\sin^2 x}$. Both the numerator and denominator vary, with the numerator having M times more oscillations than the denominator. When the denominator goes to zero, this function does not blow up and go to infinity because the numerator also goes to zero. By L'Hopital's rule from Calculus, we find that

$$\frac{\sin^2 Mx}{\sin^2 x} = M^2 \text{ when } x = h\pi, \text{ where } h = 0, \pm 1, \pm 2, \dots$$

Physically, this corresponds to the occurrence of a Bragg peak at the condition when $\bar{Q} \cdot \bar{a} = h$.

Recall that $\bar{Q} \cdot \bar{a}$ is the extra path length in units of λ for the waves scattered by two atoms separated by \bar{a} . This makes sense with previous considerations of Braggs' law, in which an integer multiple wavelength difference in paths yields a diffraction peak. In Figure 10.7 below, $\sin x$, $\sin^2 x$, and $\frac{1}{5} \sin^2 5x$ are plotted against x . The green $\sin^2 x$ curve represents the denominator, and the red curve represents the $\sin^2 Mx$ numerator where $M=5$. Note that the red curve has five times the oscillations of the green curve and the two have three common zeros in this range of x . Namely at $x = 0, \pi$, and 2π .

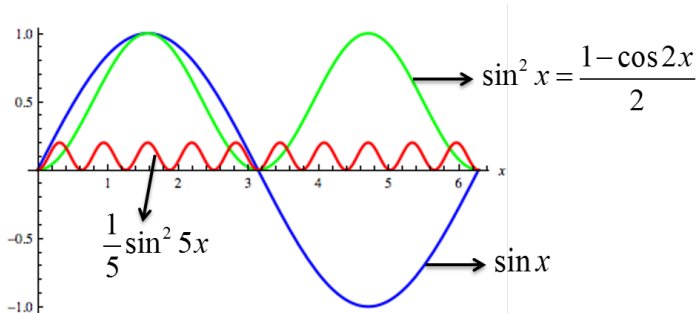


Figure 10.7: 1D interference oscillations

In the one-dimensional interference function, the red function in Figure 10.7 is divided by the green function to yield the plot in Figure 10.8.

Note that the one-dimensional interference function is multiplied by a $\frac{1}{M^2}$ factor to yield the following normalized function that has a maximum of one:

$$I(x) = \frac{\sin^2 Mx}{M^2 \sin^2 x} \quad (10.17)$$

Figure 10.8 illustrates the unity amplitude diffraction peaks that occur when the numerator and denominator have common zeros, at $x = h\pi$, where h is an integer. A zeroth order peak occurs when all waves are scattered in phase and in the forward direction. In addition, in between any two consecutive Bragg peaks there are $M - 2$ subsidiary peaks (Laue oscillations), due to the numerator, $\sin^2 Mx$, going to zero. The periodicity of these subsidiary peaks (or Laue fringes) is $\frac{\pi}{M}$. Note that the numerator also goes to zero at the Bragg peaks. Therefore the Bragg peaks' full-width-full-max, FWFM = $\frac{2\pi}{M}$.

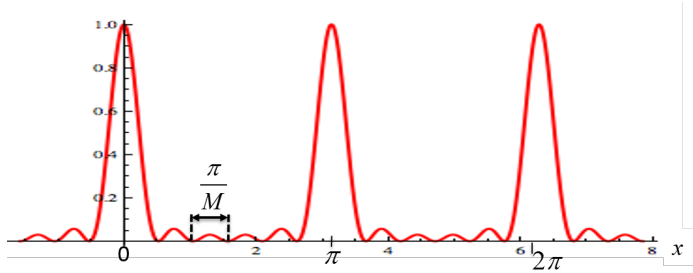


Figure 10.8: Normalized 1D interference function, where $M=6$

What is x in terms of the angle θ ?

The quantity x is the scattering vector \bar{Q} multiplied by π , and projected in the direction of the lattice constant, \bar{a} . If the lattice constant and the scattering vector are in the same direction, this simplifies to the following expression:

$$x = \pi \bar{Q} \cdot \bar{a} = \pi Q a = \pi \frac{|\bar{S} - \bar{S}_0|}{\lambda} a = \pi \frac{2 \sin \theta}{\lambda} a$$

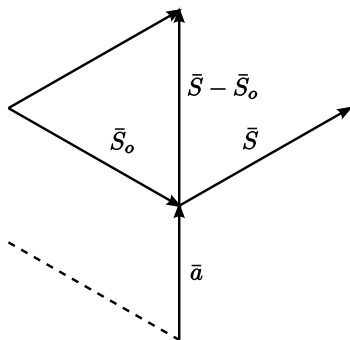


Figure 10.9: Physical relationship between X-ray directions, and \bar{a} - used in describing "x"

$$\text{At } x = \frac{\pi}{M} = \frac{2\pi \sin \theta_{min}}{\lambda} a \rightarrow \frac{\sin \theta_{min}}{\lambda} = \frac{1}{2Ma} \rightarrow \theta_{min} = \sin^{-1} \left[\frac{\lambda}{2Ma} \right]$$

Here, θ_{min} represents the first appearing minimum in the periodic intensity pattern.

For a very large M , $\sin \theta$ can be set equal to θ , and the following expression can be used to determine the full-width-full-max (FWFM) diffraction peak width as illustrated in Figure 10.10. Note that this is simply twice the value of θ_{min} .

$$2\Delta\theta = 2\theta_{min} = \frac{\lambda}{Ma} \text{ for } h=0$$

Therefore by measuring the FWFM of the entire diffraction peak, the value M may be determined, which indicates the number of unit cells in the direction of \bar{a} . Multiplying M by a yields the crystal's thickness in the direction of a . Notice that $\Delta\theta$ and Ma are inversely proportional; Therefore, as the thickness of a crystal Ma increases the $\Delta\theta$, or width of the peak, gets smaller.

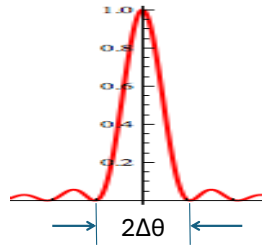


Figure 10.10: $2\Delta\theta$ (FWFM) of peaks shown in Figure 10.8

Note the following correlation with Bragg's Law:

$$\lambda = 2d \sin \theta, \text{ in this case } \lambda = 2a \sin \theta$$

$$\frac{2a \sin \theta}{\lambda} = 1 \rightarrow \bar{Q} \cdot \bar{a} = 1 = h$$

Furthermore, for all other peaks ($h \neq 0$)

$$FWFM = 2\Delta\theta = \frac{\lambda}{Ma \cos \theta} \quad (10.18)$$

Since the Bragg peak intensity goes as M^2 and the width goes as M^{-1} , it follows that the area under the Bragg peak is proportional to the number of unit cells M . As M approaches ∞ , the intensity pattern approaches a periodic series of delta functions as shown in Figure 10.11.

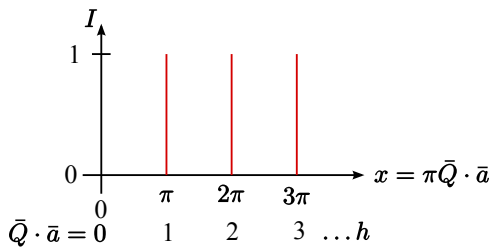


Figure 10.11: As $M \rightarrow \infty$, the normalized 1D interference function approaches a series of delta functions, where \bar{Q} is the scattering vector and \bar{a} is the 1D lattice constant.

10.2.1 1D Interference Function Summary

For the scattering vector \bar{Q} parallel to a 1D periodic array of M delta-function scatterers with lattice constant \bar{a} , kinematical scattering theory predicts the scattered intensity to be

$$I(Q) = \frac{\sin^2(M\pi Qa)}{\sin^2(\pi Qa)} \dots \dots Q = \frac{2\sin\theta}{\lambda} \quad (10.19)$$

Bragg peaks occur when the denominator $\rightarrow 0$ at $Q = \frac{h}{a}$.

The Bragg peak Intensity $I_{max} = M^2$.

Based on the numerator, the Laue fringe periodicity $\Delta Q = \frac{1}{Ma}$.

Based on the numerator, the Bragg peak width $\Delta Q \propto \frac{1}{Ma}$.

The Bragg peak area $\propto M$.

10.3 1D Interference Function Example

Let's see if we can interpret actual XRD data from a hetero-epitaxial thin film structure in terms of the 1D interference function. This published data [?] is for a ferroelectric (FE) capacitor grown by chemical vapor deposition (CVD) on a $\text{SrTiO}_3(001)$ single-crystal substrate. Referring to Fig. 10.12, the FE was a single crystal film of PbZrTiO_3 (PZT). The bottom electrode was a single crystal film of SrRuO_3 , and the top electrode was a Ag film that does not show up in this data because it was polycrystalline. This $\theta - 2\theta$ scan was collected at an APS undulator at a wavelength of $\lambda = 0.914\text{\AA}$. The three prominent peaks are the first-order (001) Bragg peaks for the three perovskite crystals as labeled. From the wavelength and peak positions in the incident angle θ , we can use Braggs' law to calculate the c lattice constants for the SrTiO_3 , SrRuO_3 , and PZT to be $c = d_{001} = 3.905$, 3.970 , and 4.130\AA . As predicted by the numerator of the interference function, the widths of peaks and their Laue fringe periodicity are inversely proportional to the film thickness (t). Namely, $t = Mc = \frac{\lambda}{2\Delta\theta \cos\theta}$, where $\Delta\theta$ is the period of the Laue fringes measured in radians.

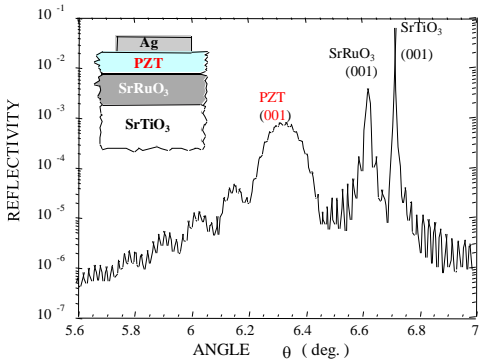


Figure 10.12: Experimental X-ray reflectivity from a PZT capacitor structure that was collected at $\lambda = 0.914\text{\AA}$. The inset shows the layers within the heteroepitaxial structure. If you measure the Laue fringe periodicity, you should find that the SrRuO_3 bottom electrode is 136-nm-thick and the PZT film is 20-nm-thick. The Ag top electrode is polycrystalline and does not measurably contribute to the scattered intensity in this high-resolution scan.

11 Crystal Diffraction in Reciprocal Space

From the perspective of reciprocal space, we will now combine wave scattering with what we learned earlier about crystallography. Recall the following 3D interference function for an X-ray plane-wave scattering from a small crystal with $M = M_1 M_2 M_3$ unit cells.

$$\bar{I}_{eu} = |F|^2 \frac{\sin^2(M_1 \pi \bar{Q} \cdot \bar{a})}{\sin^2(\pi \bar{Q} \cdot \bar{a})} \cdot \frac{\sin^2(M_2 \pi \bar{Q} \cdot \bar{b})}{\sin^2(\pi \bar{Q} \cdot \bar{b})} \cdot \frac{\sin^2(M_3 \pi \bar{Q} \cdot \bar{c})}{\sin^2(\pi \bar{Q} \cdot \bar{c})}, \quad (11.1)$$

11.1 Laue condition for diffraction

In three dimensions, Bragg diffraction occurs when all three denominators simultaneously go to zero; that is when the following three conditions are met:

$$\bar{Q} \cdot \bar{a} = h$$

$$\bar{Q} \cdot \bar{b} = k$$

$$\bar{Q} \cdot \bar{c} = l$$

where h, k, l are integers.

This is known as the **Laue condition** for diffraction. Note that the h, k, l indices are the same Miller indices used to describe the planes of a crystal in direct space.

The above three scalar equations, which describe the \bar{Q} values that lead to the Laue condition, are equivalent to the following single vector equation.

$$\bar{Q} = h\bar{a}^* + k\bar{b}^* + l\bar{c}^* = \bar{r}_{hkl}^* \quad (11.2)$$

Simply put, the Laue condition (Bragg diffraction) occurs whenever the scattering vector \bar{Q} , defined by the diffractometer, coincides with a reciprocal lattice vector \bar{r}_{hkl}^* , defined by the hkl crystal planes. At the Laue condition, \bar{Q} will be perpendicular to the hkl planes and have a length of $\frac{1}{d_{hkl}}$.

Considering the scalar of this vector equation, we derive Braggs' Law.

$$\bar{Q} = \bar{r}_{hkl}^* \rightarrow |\bar{Q}| = |\bar{r}_{hkl}^*| \rightarrow \frac{2 \sin \theta}{\lambda} = \frac{1}{d_{hkl}} \Rightarrow \lambda = 2d_{hkl} \sin \theta$$

Therefore, the maxima of the hkl diffraction peaks occur at:

$$\bar{Q} = \frac{\bar{S}}{\lambda} - \frac{\bar{S}_0}{\lambda} = \bar{r}_{hkl}^* \quad (11.3)$$

Where \bar{Q} is the scattering vector, $\frac{\bar{S}}{\lambda}$ is the scattered wave vector, $\frac{\bar{S}_0}{\lambda}$ is the incident wave vector, and \bar{r}_{hkl}^* is the reciprocal lattice vector for the hkl diffraction planes of the crystal.

This vector relationship is illustrated in Figure 11.1 below. The scattering vector \bar{Q} is continuously adjustable over a range in 3D reciprocal space through the adjustment of the incident direction, wavelength, and 2θ direction of the detector. (Usually, only the direction of the detector is varied in an X-ray diffraction (XRD) experiment.) The \bar{r}_{hkl}^* vectors describe the sample, a crystal consisting of discrete

sets of planes in discrete directions indexed by \bar{r}_{hkl}^* in reciprocal space. Therefore, as described by the Laue condition, a diffracted beam will be detected when the instrument's continuously variable \bar{Q} vector coincides with one of the discrete \bar{r}_{hkl}^* vectors of the samples.

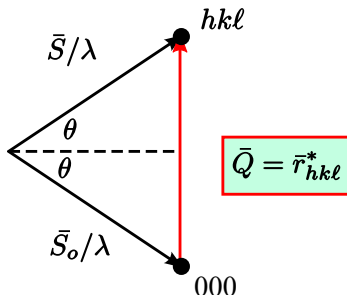


Figure 11.1: The hkl diffraction peak condition (or Laue condition) described by vectors in reciprocal space.

11.1.1 Vector Representation in Reciprocal Space

To picture a diffraction experiment in reciprocal space, recall that the crystal planes, as referenced by their hkl Miller indices, are transformed into hkl reciprocal lattice points in reciprocal space. Figure 11.2 illustrates the 012 reflection in the $h = 0$ reciprocal lattice layer of a cubic crystal. In this example, the incident beam is described by the incident wave vector $\frac{\bar{S}_o}{\lambda}$ with a fixed direction and wavelength. The sample crystal is at C, the center of the Ewald sphere with radius $\frac{1}{\lambda}$. The circle is the sphere's equator, coinciding with the $h = 0$ plane in reciprocal space. The line segment centered at C represents the 012 diffraction plane with an orientation to the incident beam. The incident angle has been rotated to the Bragg condition $\theta = \theta_B$. Coherent (same wavelength) scattered wave vectors $\frac{\bar{S}}{\lambda}$ emanate outward from C such that the locus of their tips forms a spherical surface referred to as the **Ewald sphere**. The Laue condition is satisfied whenever a point on this sphere coincides with an hkl reciprocal lattice point. The diffracted beam is detected by rotating the angle of the detector to $2\theta = 2\theta_B$.

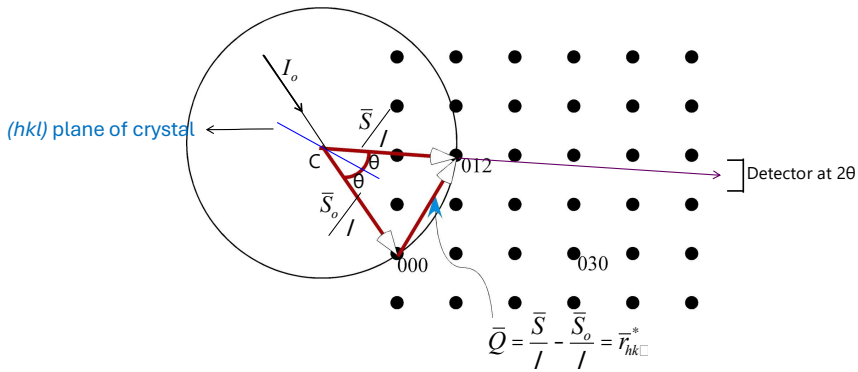


Figure 11.2: The Ewald sphere construction for the 012 Laue condition for a cubic crystal.

11.1.2 Ewald Sphere

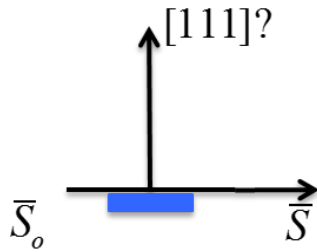
(Radius = $\frac{1}{\lambda}$)

If incident direction (\bar{S}_0) is fixed and λ is fixed

1. Sphere does not move or change size.
2. $\frac{\bar{S}_0}{\lambda}$ always points from center (C) to 000 .
3. As the crystal rotates in θ , the reciprocal lattice rotates in unison about 000 .
4. $\frac{\bar{S}}{\lambda}$ points from C to any points on sphere.
5. Diffraction occurs when an hkl reciprocal lattice point coincides with the surface of the Ewald sphere.
6. For X-ray wavelengths, multiple reflections are rare. This probability increases at higher energies where the Ewald sphere has a larger radius.

11.2 Single Crystal Diffractometer

Consider the scenario where you go to a friend's lab to borrow a Si(111) wafer. Your friend has Si wafers but does not know if they are (111) or (001). How would you use a $\theta - 2\theta$ diffractometer and a monochromatic beam to determine if its face is (111) or (001)?

**Figure 11.3:** Si wafer

1. Rotate detector to $2\theta = 0$
2. Rotate sample to $\omega = 0$, i.e., surface \parallel to beam as depicted in Fig. 11.3.

In reciprocal space, move \bar{r}_{hhh}^* into diffractometer plane, i.e., rotate crystal $\rightarrow \bar{r}_{hhh}^* \perp \bar{S}_0 \rightarrow \bar{r}_{hhh}^* \perp 2\theta$ axis beam as depicted at top of Fig. 11.4.

3. Do coupled $\theta - 2\theta$ scan.

Notice that at $\omega = 0$ and $2\theta = 0$, the incident wave vector and the scattered wave vector coincide with each other. ω and 2θ will be rotated, so that ω is always half of 2θ . This rotation is continued until the condition in the bottom of Figure 11.4b is reached. Note that the Ewald sphere is fixed, and the reciprocal lattice points are now angled, indicating the crystal is rotating.

4. Looking at the diffraction peaks, the silicon wafer face is found to be (111) since a (001) face would yield diffraction peaks of the order $(00l)$, with $l = 4, 8, 12, \dots$

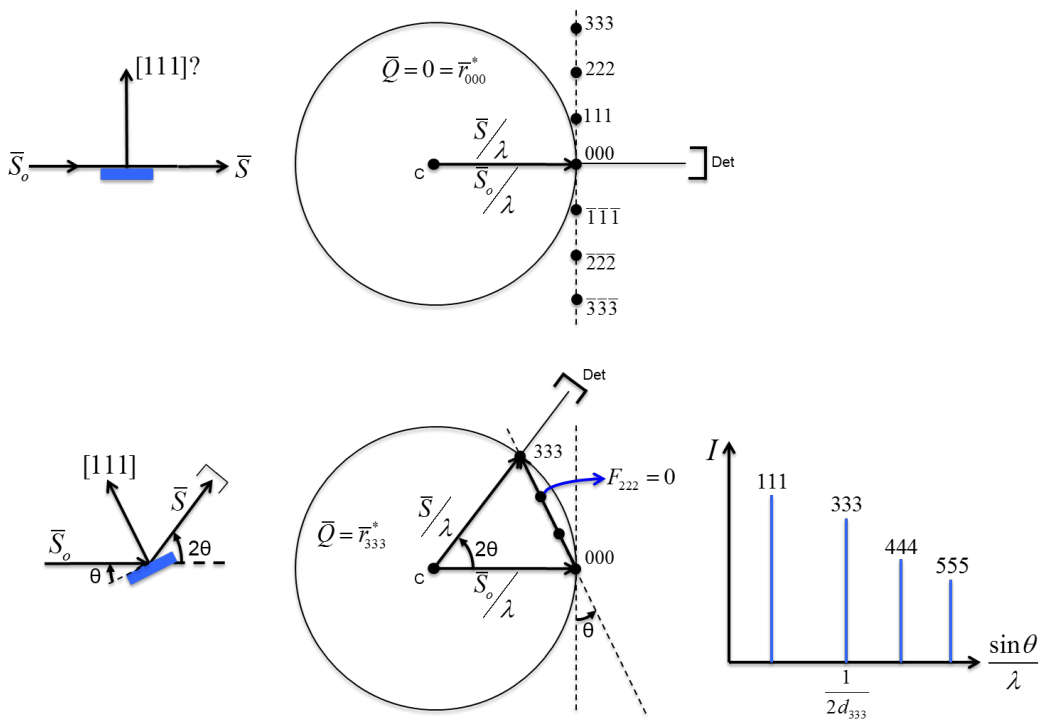


Figure 11.4: $\theta - 2\theta$ scan of Si wafer that produces a sequence of Bragg peaks expected for a wafer with a (111) surface. Top: The $2\theta = 0$ starting condition for the scan. Bottom: The point in the scan where the 333 Bragg condition occurs.

Note: The 222 is missing because $F_{222} = 0$ for Si.

11.3 Diffraction Methods

Table 9 summarizes the Laue method, rotating crystal method, and powder method based on the variability of λ and θ . The rotating crystal method, discussed in the previous section, uses a monochromatic beam of fixed wavelength and has a variable θ for scanning through a sequence of diffraction peaks. The Laue method has a fixed θ and a variable wavelength since the incident beam is continuous rather than monochromatic and allows for various diffraction peaks to appear at once. The powder method has a monochromatic beam of fixed wavelength and a variable θ since the crystallites in the beam have random orientations.

Diffraction Methods	λ	θ
Laue Method	Variable	Fixed
Rotating Crystal Method	Fixed	Variable
Powder Method	Fixed	Variable

Table 9: Diffraction methods

11.3.1 Laue Method - white beam / single crystal

For the Laue method, there is an incident white beam consisting of a Bremsstrahlung continuum of wavelengths that scatters from a crystal, as shown below in Figure 11.5. The crystal consists of sets of planes, indexed in reciprocal space by the \vec{r}_{hkl}^* vectors perpendicular to the planes in real space. Satisfying Braggs' law based on these crystal planes creates a Laue spot on the film or 2D detector located downstream from the sample. This film location is used in the transmission Laue experiment setup.

Transmission Laue $\theta < 2\theta < 90^\circ$

$0^\circ < \theta < 45^\circ$

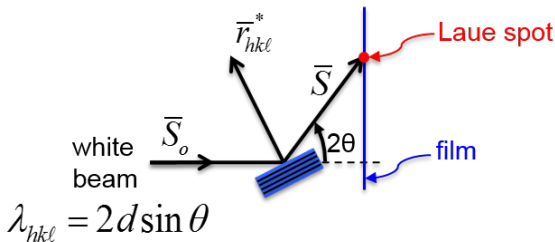


Figure 11.5: Transmission Laue diffraction.

In the back reflection geometry, the beam comes through a hole in the film or 2D area detector and hits the crystal planes in the single crystal sample as illustrated in Figure 11.6. The crystal selects a particular wavelength that matches up to a particular reflection of planes and spacings such that the scattered monochromatic beam satisfies Braggs' law. There are multiple wavelengths that are harmonics or integer multiples of each other that make up a Laue spot i.e. 220 , 440 , 880 , etc. However, the diffraction intensity gets weaker for higher harmonics due to several different factors, including the atomic scattering factor.

Back Reflection Laue

$90^\circ < 2\theta < 180^\circ$

$45^\circ < \theta < 90^\circ$

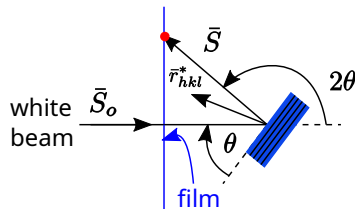


Figure 11.6: Back reflection Laue diffraction.

11.3.2 Reciprocal lattice treatment of Laue method

In reciprocal space, there is a continuum of Ewald spheres due to the continuum of wavelengths in the incident white beam. Recall that the Ewald sphere radius equals $\frac{1}{\lambda}$. All Ewald spheres touch the origin 000 , as illustrated in Figure 11.7. Note that this illustration shows cross sections of the Ewald spheres, and a cut of the orthorhombic P reciprocal lattice.

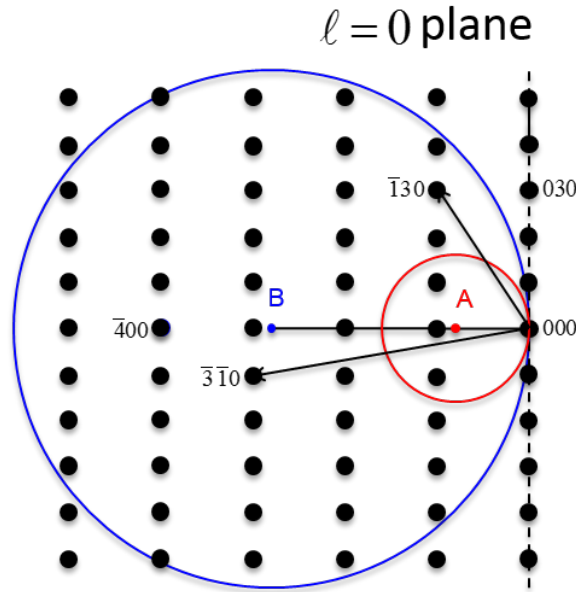


Figure 11.7: Orthorhombic P reciprocal lattice in conjunction with smallest and largest Ewald spheres for Laue method.

The incident wave vector is in the direction of \bar{S}_o , and its length is continuum over some range due to the continuum of wavelengths in the incident beam. In the case of Figure 11.8, the crystal is oriented in a fixed direction such that the [100] direction is coincident with the incident beam. The wavelength range of this beam is from the short wavelength limit set by the accelerating voltage to a rough upper limit of 2\AA due to absorption effects.

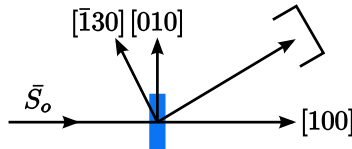


Figure 11.8: Incident wave vector
 $\lambda_{SWL} < \lambda < 2\text{\AA}$

Looking back at Figure 11.7, the smaller sphere corresponds to the upper wavelength limit of lower energy, and the larger sphere corresponds to the short wavelength limit

of higher energy. Note that the radius of the small sphere is AO , and the radius of the larger sphere is BO . The two radii correspond to the limits of the incident wave vector \bar{S}_0 , ranging in length from AO to BO .

- ◊ $AO < \frac{\bar{S}_0}{\lambda} < BO$
- ◊ $AO = \frac{1}{2A} = 0.5 \text{\AA}^{-1}$
- ◊ $BO = \frac{1}{\lambda_{SWL}} \approx 5 \text{\AA}^{-1}$

Consider the $(\bar{1}30)$ Bragg reflection, whose vector diagram is illustrated in Figure 11.9. Note that the length of the normalized incident wave vector is equal to that of the normalized scattering vector due to their equal wavelengths. This $(\bar{1}30)$ reflection is allowed since its vector is between the minimum and maximum Ewald spheres AO and BO in Figure 11.7. Note that the two vectors form an isosceles triangle and that the scattering vector \bar{Q} is coincident with the reciprocal lattice vector $\bar{r}_{\bar{1}30}^*$. Since the 2θ angle is less than 90° , this is the transmission Laue condition.

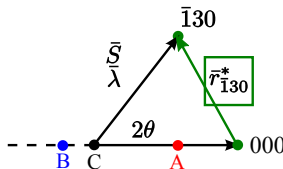


Figure 11.9: $(\bar{1}30)$ reflection

$2\theta < 90^\circ \rightarrow$ Transmission Laue

Now consider the $(\bar{3}\bar{1}0)$ reflection illustrated in Figure 11.10, in which 2θ is greater than 90° . This is a back reflection Laue condition. Note that the incident and scattered wave vector form two legs of an isosceles triangle with their vertex at some point between the smallest and largest Ewald spheres for the experiment.

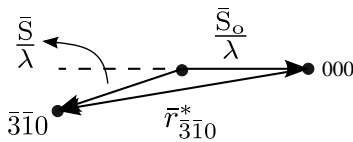


Figure 11.10: $\bar{3}\bar{1}0$ reflection

$2\theta > 90^\circ \rightarrow$ Back Reflection Laue

In general, the reciprocal lattice points outside the smallest Ewald sphere of radius $\frac{1}{2A}$ and inside the largest sphere of radius $\frac{1}{\lambda_{SWL}}$ may produce Bragg reflections.

11.4 Structure Factor Examples

Recall that at the Bragg peak, the intensity relative to the intensity of one electron scatterer is derived from the 3D interference function. The following equation yields this relative peak intensity: $I_{(eu)} = FF^* M^2$

Here, $M = M_1 M_2 M_3$ represents the number of unit cells that are diffracting, where in three dimensions M_1 , M_2 , and M_3 define the number of unit cells along the three distinct axes. The structure factor times its complex conjugate, $|F|^2$, affects the relative intensity of the Bragg peak, and is given by the summation of the individual atomic scattering factors of the N atoms in the unit cell and their respective phase factors.

$$F(\bar{Q}) = \sum_{n=0}^{N-1} f_n(Q) e^{2\pi i \bar{Q} \cdot \bar{r}_n} \quad (11.4)$$

Structure Factor for unit cell with N atoms

Recall that the individual atomic scattering factor has a form factor and anomalous dispersion corrections, such that $f_n = (f_0(\frac{\sin\theta}{\lambda}) + \Delta f' + i\Delta f'')_n$. We will simplify this by assuming that $f_n = (f_0)_n$.

You should consider the $e^{i\phi}$ phase factor as a unit vector in the complex plane. If two atoms scatter in phase, their unit vectors will point in the same direction in the complex plane. If they scatter π out of phase, the unit vectors will point in opposite directions. Of course, the relative phase between two scattered waves is variable, not just 0 or π . Carrying this further, the above summation can be thought of as summation of N vectors with lengths f_n and phases $2\pi \bar{Q} \cdot \bar{r}_n$ in the complex plane added tail to head in sequence to get the final resultant vector.

The position of the n^{th} atom is expressed as: $\bar{r}_n = x_n \bar{a} + y_n \bar{b} + z_n \bar{c}$.

At the hkl Bragg peak the scattering vector coincides with the reciprocal lattice vector \bar{r}_{hkl}^* . That is $\bar{Q} = \bar{r}_{hkl}^* = h\bar{a}^* + k\bar{b}^* + l\bar{c}^*$. Thus, \bar{r}_{hkl}^* replaces the scattering vector in the above structure factor equation such that

$$\bar{r}_{hkl}^* \cdot \bar{r}_n = (h\bar{a}^* + k\bar{b}^* + l\bar{c}^*) \cdot (x_n \bar{a} + y_n \bar{b} + z_n \bar{c}) = hx_n + ky_n + lz_n.$$

Notice that all the cross terms vanished in this dot product between a reciprocal space vector and real space vector because $\bar{a}_i^* \cdot \bar{a}_j = \delta_{ij}$. (Here the Kronecker delta is defined as: $\delta_{ij} = 1$, if $i=j$ and $\delta_{ij} = 0$, if $i \neq j$.)

Therefore, the hkl structure factor for any 3D crystal system, including triclinic, is:

$$F_{hkl} = \sum_{n=0}^{N-1} f_n e^{2\pi i (hx_n + ky_n + lz_n)}. \quad (11.5)$$

We will now put this formula to work for several simple crystal structures.

11.4.1 Primitive Unit Cell (P)

The simplest structure factor example is a primitive unit cell with one atom per lattice point. This atom is placed at the origin for convenience.

1 atom/lattice point $\rightarrow N=1$ $x_n = y_n = z_n = 0$

$$F_{hkl} = f\left(\frac{\sin\theta}{\lambda}\right) = f\left(\frac{1}{2d_{hkl}}\right) \quad (11.6)$$

$$FF^* = f^2, \text{ for all } hkl. \quad (11.7)$$

11.4.2 Body-Centered (I) Bravais Lattice

For the body-centered cubic, tetragonal, and orthorhombic Bravais lattices with one atom per lattice point, there are $N=2$ atoms per unit cell. A 2D projection is illustrated in Figure 11.11.

The 2 identical atoms are located at positions r_1 and r_2 :

$$\bar{r}_1 = 000, \bar{r}_2 = \frac{1}{2} \frac{1}{2} \frac{1}{2}$$

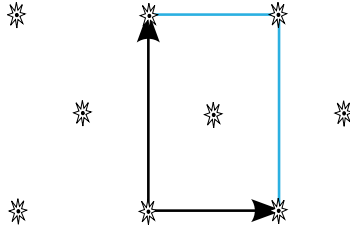


Figure 11.11: Body-centered (I) Bravais lattice

The following is the structure factor calculation for any body-centered Bravais lattice with one atom per lattice point:

$$F_{hkl} = f \left(1 + e^{2\pi i \left(\frac{h}{2} + \frac{k}{2} + \frac{l}{2} \right)} \right) = f(1 + e^{\pi i(h+k+l)}) \quad (11.8)$$

If $h+k+l$ is an even integer, the structure factor is equal to $2f$ because the two atoms are scattering perfectly in phase.

$$F_{hkl} = f(1 + 1) = 2f \quad (11.9)$$

for $h + k + l = 2n$ (even sum)

If $h+k+l$ is an odd integer, the structure factor is zero, because the two atoms are scattering perfectly out of phase.

$$F_{hkl} = f(1 - 1) = 0 \quad (11.10)$$

for $h + k + l = 2n + 1$ (odd sum)

Note:

$$e^{n\pi i} = (-1)^n = \begin{cases} -1, & \text{for odd } n \\ 1, & \text{for even } n \end{cases} \quad (11.11)$$

11.4.3 Base-Centered (C) Bravais Lattice

The base-centered lattices have two lattice points per unit cell. If there is 1 atom per lattice point $\rightarrow N=2$

The atoms are located at the following positions:

$$\bar{r}_1 = 000, \bar{r}_2 = \frac{1}{2}\frac{1}{2}0$$

Plugging these positions into the structure factor equation yields the following:

$$F_{hkl} = f(1 + e^{\pi i(h+k)}) = f(1 + (-1)^{h+k}) \quad (11.12)$$

Again, there are two cases, one in which the two atoms scatter perfectly in phase and one in which they scatter perfectly out of phase.

$$F_{hkl} = \begin{cases} 2f & h+k = 2n \\ 0 & h+k = 2n+1 \end{cases} \quad (11.13)$$

The l index does not turn off the Bragg condition.

11.4.4 Face-Centered (F) Bravais Lattice

For the face-centered lattice with one atom per lattice point, there will be four atoms total in the non-primitive unit cell.

1 atom per lattice point $\rightarrow N=4$

The atoms are located at the following positions within the unit cell:

$$\bar{r}_n = \{000, \frac{1}{2}\frac{1}{2}0, 0\frac{1}{2}\frac{1}{2}, \frac{1}{2}0\frac{1}{2}\}$$

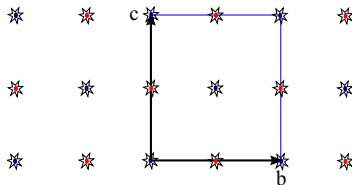


Figure 11.12: a-axis projection of a face-centered (F) Bravais lattice

The face-centered crystal with 1 atom per lattice point has the following structure factor:

$$F_{hkl} = f(1 + e^{\pi i(h+k)} + e^{\pi i(k+l)} + e^{\pi i(h+l)}) \quad (11.14)$$

There are two distinct cases for the face-centered structure. That is, when the hkl are unmixed (all even or all odd), then all four atoms scatter waves perfectly in phase, and when the hkl are mixed (even and odd), then the four atoms scatter waves cancel each other out in pairs.

$$F_{hkl} = \begin{cases} 4f & h, k, l \text{ unmixed} \\ 0 & h, k, l \text{ mixed} \end{cases} \quad (11.15)$$

For instance, the 022 planes would yield perfect constructive interference. While the 011 planes would yield perfectly destructive interference.

$$F_{022} = 4f \left(\frac{1}{2d_{022}} \right), \text{ and } F_{011} = 0$$

11.4.5 Hexagonal Closed Pack (HCP)

For the hexagonal closed-pack structure, there are two atoms of the same type per lattice point. Recall that the unit cell is hexagonal primitive, and there are two atoms in total. One atom is positioned at the origin 000 and the other atom is in the $\frac{1}{3}\frac{2}{3}\frac{1}{2}$ position.

Hexagonal-P Bravais Lattice

Ex. Zn, Ti, Mg

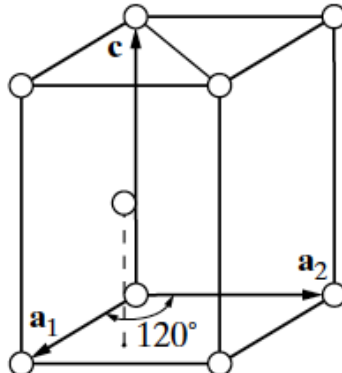


Figure 11.13: HCP structure

Using the hexagonal closed-pack atom locations yields the following structure factor:

$$F_{hkl} = f \left[1 + e^{2\pi i \left(\frac{h}{3} + \frac{2k}{3} + \frac{l}{2} \right)} \right] = f(1 + e^{2\pi iq}), \text{ where } q = \frac{h+2k}{3} + \frac{l}{2}$$

The structure factor times its complex conjugate eliminates the imaginary terms and simplifies the expression into the following:

$$FF^* = f^2 (2 + e^{2\pi iq} + e^{-2\pi iq}) = 2f^2(1 + \cos 2\pi q)$$

Because there are two atoms in the unit cell, we expect two extreme conditions - one in which the two scatter perfectly out of phase and one in which the two scatter perfectly out of phase. When the parameter q is an integer, $\cos 2\pi q$ will equal 1, producing a very strong reflection due to constructive interference. If q is equal to an odd integer, then $2\pi q$ will equal -1 , yielding a total intensity of zero.

Squaring the magnitude of the structure factor yields the following expression:

$$|F|^2 = 4f^2 \cos^2 \pi q = 4f^2 \cos^2 \left[\pi \left(\frac{h+2k}{3} \right) + \frac{l}{2} \right] \quad (11.16)$$

1. $l = 2n$ (even) AND $h + 2k = 3m$

$$\Rightarrow q = (m+n) \in Z \rightarrow \cos^2 \pi q = (\pm 1)^2 = 1$$

$|F|^2 = 4f^2$ e.g., (002), (112), ... very strong (in-phase scattering)

2. $l = 2n$ AND $h + 2k = 3m \pm 1 \Rightarrow q = (m+n) \pm \frac{1}{3} = m' \pm \frac{1}{3}$

$$\cos \pi q = \cos \pi m' \cos \frac{\pi}{3} \pm \sin \pi m' \sin \frac{\pi}{3} = \cos \frac{\pi}{3} = \frac{1}{2}$$

$|F|^2 = f^2$ e.g., (102), (200), (100)...weak reflection

3. $l = 2n + 1$ (odd) AND $h + 2k = 3m \Rightarrow q = n + \frac{1}{2} + m = m' + \frac{1}{2} \rightarrow \cos \pi q = \cos m' \pi \cos \frac{\pi}{2} - \sin m' \pi \sin \frac{\pi}{2} = 0$

$|F|^2 = 0$ e.g., (001), (111), ... forbidden reflection

4. $l = 2n + 1$ AND $h + 2k = 3m \pm 1 \Rightarrow q = n + \frac{1}{2} + m \pm \frac{1}{3} = m' \pm \frac{1}{6}$

$|F|^2 = 3f^2$ e.g., (103), (013), (101)... strong reflection

Therefore, there are four types of diffraction peak intensities for this hexagonal closed pack structure, ranging from forbidden reflections to very strong reflections.

11.4.6 More than one atom type per unit cell

We will now analyze the case of more than one atom type per unit cell such as the rock-salt lithium fluoride structure.

$\text{LiF} \rightarrow \text{NaCl structure} \quad \text{FCC}$

The following indices locate the lithium and fluorine atoms within the face centered cubic unit cell:

Li^+ at $000 + fct$

F^- at $\frac{1}{2}00 + fct$

$$fct = \left\{ 000, \frac{1}{2}\frac{1}{2}0, 0\frac{1}{2}\frac{1}{2}, \frac{1}{2}0\frac{1}{2} \right\}$$

The structure factor is given by the following equation:

$$F_{hkl} = \sum_{n=1}^8 f_n e^{2\pi i(hx_n + ky_n + lz_n)}$$

$$F_{hkl} = f_{Li^+} (1 + e^{\pi i(h+k)} + e^{\pi i(k+l)} + e^{\pi i(h+l)}) + f_{F^-} e^{2\pi i \frac{h}{2}} (1 + e^{\pi i(h+k)} + e^{\pi i(k+l)} + e^{\pi i(h+l)})$$

$$F_{hkl} =$$

◇ $4(f_{Li^+} + f_{F^-})$ for h, k, l all even $\rightarrow (200), (222)$, etc.

◇ $4(f_{Li^+} - f_{F^-})$ for h, k, l all odd $\rightarrow (111), (311)$, etc.

◇ 0 for h, k, l mixed $\rightarrow (210), (001)$, etc.

Recall, in the lab that you saw: a strong (200), weak (111), & forbidden (100) for LiF powder diffraction.

Note that the Laue method is useful for finding the symmetry of crystal orientations, but not useful for finding the lattice constant due to a variable wavelength. Furthermore, the Laue spot position is independent of the length of r^* and only dependent on its direction.

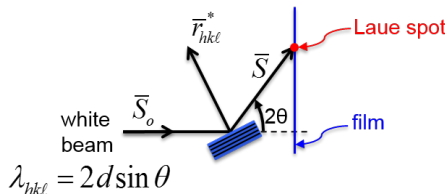


Figure 11.14: Laue spot position

11.5 Width of Diffraction Peaks (single crystal)

Reciprocal lattice points have dimensions which are inversely proportional to the size of a crystal in a given direction. $\propto \frac{1}{aM_1}, \frac{1}{bM_2}, \frac{1}{cM_3}$

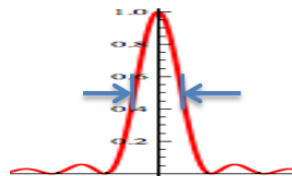


Figure 11.15: Diffraction peak intensity vs Q based on 1D interference function.

Recall the 3-D Interference Function whose M_1 component is given by the following:

$$\frac{\sin^2(M_1\pi\bar{Q} \cdot \bar{a})}{\sin^2(\pi\bar{Q} \cdot \bar{a})} \quad (11.17)$$

The numerator in the function causes the subsidiary oscillations and set the Bragg peak widths of the diffraction pattern, whereas the denominator causes the Bragg peaks to occur. When M_1, M_2 , and M_3 are small numbers, there is visibly broadening of the peaks in the diffraction pattern. There is also a decreased peak height, which varies as M^2 . The reciprocal lattice points which were previously assumed infinitesimal, now have a breadth related to the width of the Bragg peaks as shown in the two dimensional projection of Figure 11.16. Note that the size of the crystal may be different in the a and b directions.

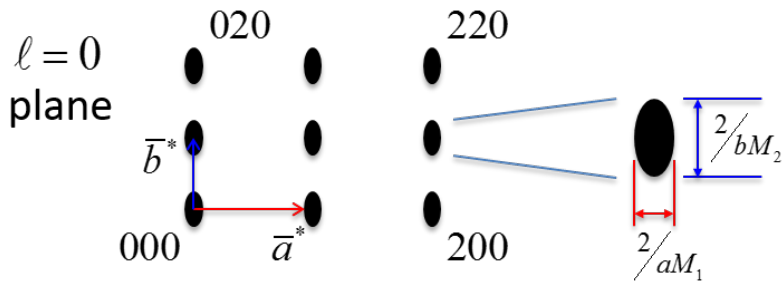


Figure 11.16: Widths of reciprocal lattice points to account for crystal size in the \bar{a} and \bar{b} directions.

For a $\theta - 2\theta$ scan along the \bar{r}_{100}^* direction, the diffraction peak width is proportional to the breadth of reciprocal lattice spot in \bar{r}_{100}^* direction or $\frac{2}{aM_1}$. The full width half max $\Delta\theta$ length is estimated by **Scherrer's Formula**,

$$\Delta\theta_{FWHM} = \epsilon_{1/2}(\text{radians}) = \left(\frac{\ln 2}{\pi} \right)^{1/2} \frac{\lambda}{D_{hkl} \cos\theta} = \frac{0.47\lambda}{D_{hkl} \cos\theta}, \quad (11.18)$$

Scherrer's Formula

where D_{hkl} is the crystal size (or X-ray coherence length) in the \bar{r}_{hkl}^* direction.

e.g., $D_{100} = aM_1$

If crystallites, such as those in a powder sample, are on the order of a tenth of a micron, then the width of the peak will be one milliradian. $D \approx 1000\text{\AA} \rightarrow \epsilon_{1/2} \approx 1\text{mrad} = 0.06^\circ$

Therefore when measuring a diffraction pattern, you first locate the peaks which give information about the lattice constant and symmetry of the crystal. The shape of the peak is an indicator of the crystal size in different directions.

Each Bragg peak maximum is given by $I_{hkl}^{(eu)} = |F_{hkl}|^2 M^2$, where F_{hkl} is affected by atomic positions in the unit cell.

Each Peak Width \rightarrow crystal size

In addition, crystal size may be determined from a transverse or longitudinal scan.

D_{hkl} from $\theta - 2\theta$ scan (longitudinal scan) $D_{(hkl)\perp}$ from ω scan (transverse scan) at fixed 2θ .

What else can affect the height and width of the diffraction peaks?

- ◊ Angular divergence of the incident beam - if an incident beam is very divergent
- ◊ Crystal defects - affects the width of the peak

To smooth over these two effects, we use angle integrated peak intensities to find relative values of $|F|^2$ (then compare to calculated $|F|^2$ from model).

11.6 Transverse scan (ω – scan) \equiv rock crystal through peak with 2θ fixed

In a **transverse scan** through an hkl point in reciprocal space, the incident angle ω is varied and 2θ is fixed at the Bragg condition, such that $Q = \frac{1}{d_{hkl}}$ or $2\theta = 2\sin^{-1}(\frac{\lambda}{2d})$. This experimental setup is illustrated in Figure 11.17 below, in which case the reciprocal lattice points rotate about 000, as illustrated by the black dashed lines on the left side of Figure 11.17. Since 2θ is restricted to the width of the slit, the Ewald sphere intersection with lattice point at 010 will produce a line of points that does not capture the entire integrated intensity of the reciprocal lattice ellipsoid. Recall that this is a two dimensional projection, and that the line of points depicted by a horizontal red line across the blue ellipse in Figure 11.17, is actually a plane intersection of the 010 reciprocal lattice ellipsoid. If we remove the slit and do the same scan across ω , the entire intensity is captured, as illustrated by the red ellipse in Figure 11.17. This is an angle integrated scan.

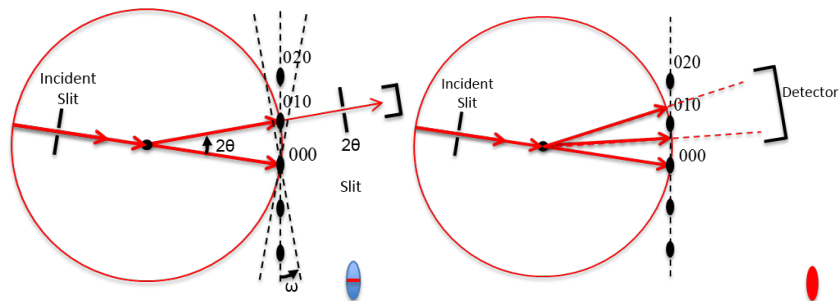


Figure 11.17: Transverse Scan through the 010 reciprocal lattice point with and without a slit.

The integrated counts or the energy in a peak is given by the following equation:

$$I_{hkl} = \frac{I_0 r_e^2 F^2 \lambda^3}{\omega' V_{uc}^2} \left(\frac{1 + \cos^2 2\theta}{2 \sin 2\theta} \right) \delta V \quad (11.19)$$

$\omega' = \frac{d\omega}{dt} \equiv$ angular velocity of crystal rotation, a step rotational scan is now used

$\omega' = \frac{\Delta\omega}{\Delta t} \equiv \frac{\text{angular step size}}{\text{time per step}} \rightarrow$ step rotational scan, a faster scan yields fewer counts

V_{uc} = unit cell volume $V_{uc} = (V_{uc}^*)^{-1}$

$\delta V \propto M_1 M_2 M_3$ = Effective volume of irradiated sample

$\left(\frac{1 + \cos^2 2\theta}{2} \right)$ = Polarization Factor for unpolarized beam

$(\sin 2\theta)^{-1}$ = Lorentz Factor for single crystal diffraction with constant ω' , $\theta \propto$ time taken to sweep Ewald sphere through a relative point (reciprocal lattice point)

Note that the tangential velocity of relative point through Ewald sphere is given by $\omega' \vec{r}_{hkl}^*$.

In Figure 11.18, notice that the 200 and 400 diffraction conditions are scanned at different speeds due to the geometry of the Ewald sphere. The intensity for the 200 lattice point will be greater because the Ewald sphere travels and scans more quickly through this point yielding a smaller intensity relative to the 400 lattice point.

This is another reason why $I_{200} > I_{400}$ for LiF

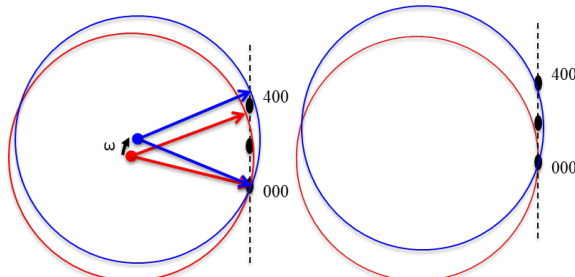


Figure 11.18: \bar{r}_{200}^* vs \bar{r}_{400}^* scan

11.7 Polycrystalline Aggregate (Powder sample)

In the **powder method**, the crystal is reduced to a fine powder of thousands of randomly oriented small single crystalline grains to be placed in a beam of monochromatic X-rays. In reciprocal space, this random orientation results in a set of concentric spherical shells centered at *000* with radii r_{hkl}^* . The illustration in Figure 11.19 below illustrates a reciprocal lattice vector range from r_{200}^* to r_{400}^* .

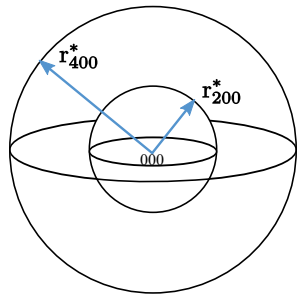


Figure 11.19: Ewald spheres for powder sample

The surface density of hkl relative points is equal to the number of crystallites divided by the surface area of the spherical shell.

$$\diamond \text{ Surface density } \propto \frac{N}{4\pi r_{hkl}^{*2}}$$

We assume that since the powder sample is isotropic, each sphere has uniform surface density. For a textured sample a preferred direction exists and the density is non-uniform.

11.7.1 Ewald construction

Note: for one r_{hkl}^* with uniform density

The Ewald sphere for one r_{hkl}^* with uniform density is illustrated in Figure 11.20 below. This blue Ewald sphere has a definite center and radius, and the monochromatic incident beam $\frac{\bar{s}_0}{\lambda}$ passes through its center to hit the origin of the sample's reciprocal lattice sphere at 000. The intersection of the Ewald sphere and the sample's sphere for one r_{hkl}^* , marked by the red dashed circle, represents the entire set of allowed scattered wave vectors $\frac{\bar{s}}{\lambda}$ that will emanate from the center of the Ewald sphere. This circular locus of points will produce a diffraction cone of scattered wave vectors beginning from the origin of the Ewald sphere and ending at the circular intersection of the two spheres. In a small slit powder diffractometer, only a segment of the circle is captured as the slit scans around 2θ . Placing a film downstream from the sample would show the entire **Bragg ring**.

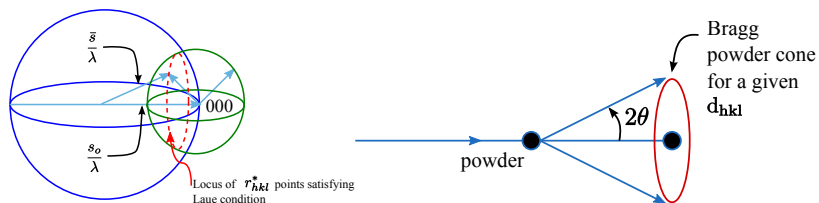


Figure 11.20: Ewald construction for powder method

This satisfies the Laue condition in which the scattering vector is equal to a specific reciprocal lattice vector of the sample.

$$\frac{\bar{s} - \bar{s}_0}{\lambda} = \bar{r}_{hkl}^*$$

11.7.2 Calculated Diffracted Intensity (Power)

$$P = I_0 \frac{\cos\theta}{2} r_e^2 F^2 \frac{\lambda^3}{V_{uc}^2} \left(\frac{1 + \cos^2 2\theta}{2 \sin 2\theta} \right) N \delta V \quad (11.20)$$

This is for entire Bragg Ring of circumference:

$$C = 2\pi R(\sin 2\theta), \cos \theta \propto \frac{\text{locus circle}}{\text{great circle of } r^*}$$

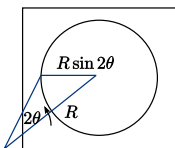


Figure 11.21: Spherical film of radius R

A horizontal diffractometer with 2θ detector slit at R and vertical slit height l records a fraction of the Bragg ring $\frac{l}{2\pi R \sin 2\theta}$.

11.7.3 Multiplicity Correction

The case of **multiplicity** occurs when different combinations of hkl have the same same r_{hkl}^* length in reciprocal space. Since these all contribute to the same spherical shell, then the overall intensity of the diffraction condition will be greater.

E.g. Cubic:

$$r_{100}^* = r_{010}^* = r_{001}^* = r_{\bar{1}00}^* = r_{0\bar{1}0}^* = r_{00\bar{1}}^* = \frac{1}{a}$$

$$\therefore m_{100} = 6, m_{h00} = 6$$

Note: C&S $m \rightarrow p$

11.7.4 Powder Diffraction Intensity

Adding in the multiplicity correction factor, the measure of the power for a diffraction condition of a given hkl is given by the following:

$$P'_{hkl} = \frac{I_0 l}{16\pi R} r_e^2 \frac{\lambda^3}{V_{uc}^2} F_{hkl}^2 m_{hkl} \left(\frac{1 + \cos^2 2\theta}{\sin 2\theta \sin \theta} \right) V_s \quad (11.21)$$

Where V_s = effective sample volume $N\delta V$ and $LP = \frac{1+\cos^2 2\theta}{\sin 2\theta \sin \theta} =$

Lorentz-Polarization factor for powder diffraction

Note: $\sin 2\theta = 2 \sin \theta \cos \theta$

Why do we use a symmetric reflection geometry for powder diffraction, if the random orientation of the crystals in the powder allow for various sampling angles and diffraction conditions at once?

(i.e. $\omega = \theta = \frac{2\theta}{2}$ or $\theta - 2\theta$ scan)

11.7.5 Absorption Effects

Recall that the linear absorption coefficient is represented by μ and that the absorption length of a material is given by $\frac{1}{\mu}$. A low Z material like water or a hydrocarbon has a longer absorption length $\frac{1}{\mu}$ than a solid metal.

Consider a large planar sample with thickness t in reflection geometry as illustrated in Figure 11.22. The incident beam with area A across enters at an angle α , and scatters from a differential volume at some depth z . The 2θ detector is lined up to pick up the scattered intensity at the angle β . In general, α and β do not have to be equal.

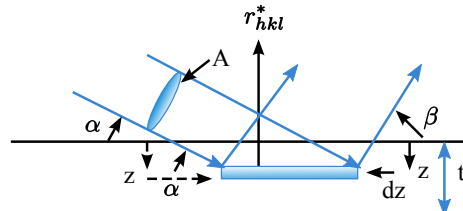


Figure 11.22: Planar sample in reflection geometry

the beam area produces a projected area of the slab that is $A/\sin\alpha$

Therefore the volume element is given by $dV = \frac{A}{\sin\alpha} dz$

The diffracted intensity at depth z is given by the following:

$$dI_z = C \frac{A}{\sin\alpha} dz I_0 e^{-uz/\sin\alpha} e^{-uz/\sin\beta} \quad (11.22)$$

There is an absorption effect that attenuates the beam as it enters and exits sample, which is accounted for by the following two transmission factors:

$e^{-uz/\sin\alpha}$ - in transmission factor

$e^{-uz/\sin\beta}$ - out transmission factor

To calculate the total intensity, we integrate over the total thickness:

$$I = \int_0^t dI_z = I_0 C \frac{A}{\mu} \left(1 + \frac{\sin\alpha}{\sin\beta}\right)^{-1} \quad (11.23)$$

Assuming the thickness is much greater than the attenuation length, or $\mu t \gg 1$ - for a typical oxide material this thickness is about 0.5 mm.

$\int_0^t dI_z = \int_0^\infty dI_z$ “t” drops out by assuming $\mu t \gg 1$ or $t \rightarrow \infty$

For symmetric reflection $\alpha = \beta = \theta \rightarrow I = I_0 C \frac{A}{2\mu} \frac{A}{2\mu} = \text{effective volume} = V_{eff}$

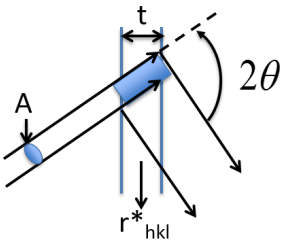
Note that the effective volume, V_{eff} , is constant and independent of θ for $\alpha = \beta = \theta$. As you increase the angle in this geometry, you are increasing the depth but decreasing the effective area. Therefore, it is convenient to use symmetric reflection geometry for a powder diffraction experiment, in order to be able to avoid varying absorption effects from a varying effective volume.

We could also do diffractometry in symmetric transmission mode as illustrated in Figure 11.23.

We want as much material in front of the beam to yield a high scattering intensity, but we also want a small enough thickness to avoid too much absorption. There is an optimal thickness in this transmission geometry, $\frac{1}{\mu}$, that yields the maximum scattering compromised correctly with the absorption. Recall that $\frac{1}{\mu}$ is the absorption length.

Effective Volume: $\frac{At}{\cos\theta} e^{\frac{-\mu t}{\cos\theta}}$

Here, V_{eff} depends on θ .

**Figure 11.23:** Transmission geometry**11.7.6 Summarize: Powder diffractometer in symmetric reflection geometry**

The area under the diffraction peak is proportional to:

$$I_{hkl} = |F_{hkl}|^2 m_{hkl} \left(\frac{1 + \cos^2 2\theta}{\sin^2 \theta \cos \theta} \right) e^{-2M} \quad (11.24)$$

F_{hkl} - structure factor hkl and $\sin \theta / \lambda$

m_{hkl} - multiplicity (hkl)

$\left(\frac{1 + \cos^2 2\theta}{\sin^2 \theta \cos \theta} \right)$ - Lorentz polarization factor, θ

e^{-2M} - temperature dependent Debye-Waller factor $\sin \theta / \lambda$ accounting for atomic vibrations

Our objective is to measure the integrated intensities I_{hkl} 's and use the structure factor F_{hkl} 's to determine the crystal structure.

At extreme angles, the Lorentz polarization factor has a considerable effect, as shown in Figure 11.24.

$$LP = \left(\frac{1 + \cos^2 2\theta}{\sin^2 \theta \cos \theta} \right) \begin{matrix} \leftarrow \text{Polarization correction} \\ \leftarrow \text{Geometrical correction} \end{matrix}$$

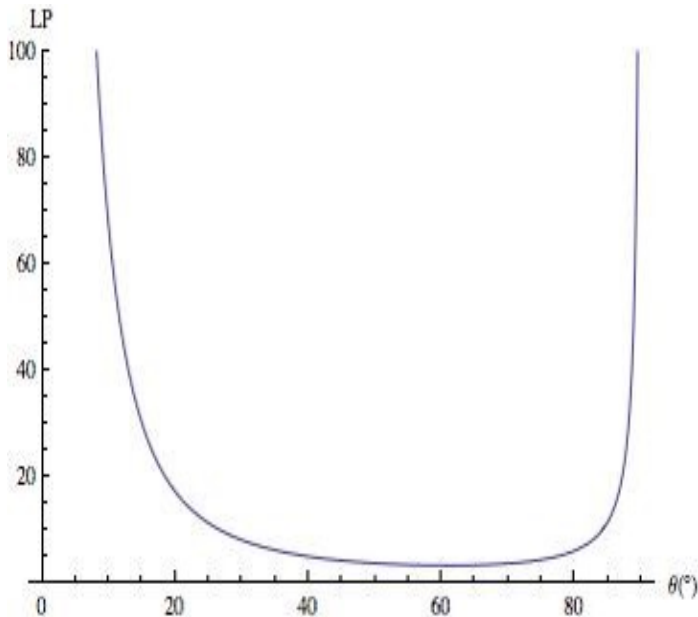


Figure 11.24: Lorentz polarization factor. LP vs. θ

11.7.7 Multiplicity Factor

m_{hkl} : number of (hkl) planes in the $\{hkl\}$ family for a given crystal system

Example:

0kk

022	02̄2
202	202
220	220
022	022
202	202
2̄20	220

Cubic $\rightarrow m_{0kk} = 12$, since all 12 $|r^*|$'s are equal

triclinic $a \neq b \neq c, \alpha \neq \beta \neq \gamma$

$r_{022}^* \neq r_{220}^*$ triclinic $m_{hkl} = 2$

$r_{022}^* = r_{02\bar{2}}^*$ Since only $r_{\bar{h}\bar{k}\bar{l}}^* = r_{hkl}^*$

See Cullity and Stock Appendix 11

Cubic:	$\frac{hkl}{48^*}$	$\frac{hhl}{24}$	$\frac{0kl}{24^*}$	$\frac{0kk}{12}$	$\frac{hh\bar{h}}{8}$	$\frac{00l}{6}$	
Hexagonal and Rhombohedral:	$\frac{hk\bar{l}}{24^*}$	$\frac{h\bar{h}l}{12^*}$	$\frac{0\bar{k}\cdot l}{12^*}$	$\frac{hk\cdot 0}{12^*}$	$\frac{h\bar{h}\cdot 0}{6}$	$\frac{0k\cdot 0}{6}$	$\frac{00\cdot l}{2}$
Tetragonal:	$\frac{hkl}{16^*}$	$\frac{hhl}{8}$	$\frac{0kl}{8}$	$\frac{hk0}{8^*}$	$\frac{hh0}{4}$	$\frac{0k0}{4}$	$\frac{00l}{2}$
Orthorhombic:	$\frac{hkl}{8}$	$\frac{0kl}{4}$	$\frac{h0l}{4}$	$\frac{hk0}{4}$	$\frac{h00}{2}$	$\frac{0k0}{2}$	$\frac{00l}{2}$
Monoclinic:	$\frac{hkl}{4}$	$\frac{h0l}{2}$	$\frac{0k0}{2}$				
Triclinic:	$\frac{hkl}{2}$						

Table 10: Multiplicity factors for powder XRD data

11.7.8 Indexing Powder Diffraction Patterns

We can determine r_{hkl}^* lengths (not directions) from experimentally measured θ' 's and a known λ using the following relationships:

$$\frac{2\sin\theta_{hkl}}{\lambda} = r_{hkl}^* = (\bar{r}^* \cdot \bar{r}^*)^{\frac{1}{2}} \quad (11.25)$$

$$= [(ha^*)^2 + (kb^*)^2 + (lc^*)^2 + 2hka^*b^*\cos\gamma^* + 2klb^*c^*\cos\alpha^* + 2hla^*c^*\cos\beta^*]^{\frac{1}{2}} \quad (11.26)$$

First index the series of peaks (i.e. determine $(hkl)_n$), then determine the lattice constants of the Bravais lattice : $a, b, c, \alpha, \beta, \gamma$

Initially check for cubic, the simplest case, where $a = b = c, \alpha = \beta = \gamma = 90^\circ$.

Cubic: $\underbrace{r^{*2}_{measured}}_{=} = \underbrace{a^{*2}[h^2 + k^2 + l^2]}_{unknown}$ subject to Bravais lattice conditions.

See Cullity and Stock,[?] Appendix 9 - also shown below in Table 11.

$h^2 + k^2 + l^2$	hkl	P	F	I	Diamond
1	100	x			
2	110	x		x	
3	111	x	x		x
4	200	x	x	x	
5	210	x			
6	211	x		x	
7					
8	220	x	x	x	x
9	300, 221	x,x			
10	310	x		x	
11	311	x	x		x
12	222	x	x	x	
13	320	x			
14	321	x		x	
15					
16	400	x	x	x	x

Table 11: Determining cubic unit cells from $h^2 + k^2 + l^2$. "x" indicates an allowed hkl reflection for a listed cubic Bravais lattice, P, F, or I, or for Diamond.

Therefore, we can check for pattern in the sequence of measured r^{*2} values, which are proportional to $h^2 + k^2 + l^2$, and relate these to the corresponding unit cells using Table 11.

$$\text{If } \{r_i^{*2}\} =$$

$$C\{1, 2, 3, 4, 5, 6, 8, \dots\} \rightarrow \text{Cubic-P}$$

$$C\{1, \frac{4}{3}, \frac{8}{3}, \frac{11}{3}, 4, \dots\} \rightarrow \text{Cubic-F}$$

$$C\{1, 2, 3, 4, 5, 6, 7, 8\} \rightarrow \text{Cubic-I}$$

$$C\{1, \frac{8}{3}, \frac{11}{3}, \frac{16}{3}, \frac{19}{3}, \dots\} \rightarrow \text{Diamond}$$

Note that we need to measure $r^* = 2 \sin \vartheta / \lambda$ for at least the first seven peaks to distinguish between Cubic-P and Cubic-I.

Tetragonal and hexagonal ("uniaxial")

$$\text{Tetragonal: } r_{hkl}^{*2} = a^{*2}(h^2 + k^2) + c^{*2}l^2 = a^{*2} \left[(h^2 + k^2) + \left(\frac{c^*}{a^*} \right)^2 l^2 \right]$$

$$\text{Hexagonal: } \cos \gamma^* = \frac{1}{2}$$

$$r_{hkl}^{*2} = a^{*2}(h^2 + k^2 + hk) + c^{*2}l^2 = a^{*2} \left[(h^2 + k^2 + hk) + \left(\frac{c^*}{a^*} \right)^2 l^2 \right]$$

$$\left(\frac{c^*}{a^*} \right)^2 = \left(\frac{a}{c} \right)^2 \text{ is unknown}$$

is 1st peak ?:

100 or 001 (P)

110 or 002 (Tetragonal I)

100 or 002 (HCP)

$$\sin^2 \theta = \frac{\lambda^2}{4} r_{hkl}^{*2} = A(h^2 + k^2) + Cl^2 \leftarrow \text{Tetragonal}$$

$$A(h^2 + k^2 + hk) + Cl^2 \leftarrow \text{Hexagonal}$$

11.7.9 Example 1

$\lambda = 1.542 \text{ \AA}$

Line No.	$\sin^2 \theta$	$\frac{(\sin^2 \theta)_n}{(\sin^2 \theta)_1}$		$h^2 + k^2 + l^2$	hkl
1	0.0603	1	3/3	3	111
2	0.1610	2.67	8/3	8	220
3	0.221	3.67	11/3	11	311
4	0.322	5.34	16/3	16	400
5	0.383	6.35	19/3	19	331
6	0.484	8.03	24/3	24	422
7	0.545	9.04	27/3	27	333
8	0.645	10.7	32/3	32	440

Table 12: Indexing Powder Patterns, Example 1

Ratios → Cubic

$$\frac{(\sin^2 \theta)_n}{(\sin^2 \theta)_1} = \frac{(h^2 + k^2 + l^2)_n}{(h^2 + k^2 + l^2)_1}$$

unmixed hkl: Cubic F

$h + k + l \neq 4n \pm 2$: diamond cubic

What is “a”?

$$r_{400}^* = 16a^*{}^2 = \frac{16}{a^2} = \frac{4 \sin^2 \theta_{400}}{\lambda^2}$$

$$a = \frac{4\lambda}{2 \sin \theta_{400}} = \frac{2 \times 1.542 \text{ \AA}}{(0.322)^{1/2}} = 5.434 \text{ \AA}$$

Silicon a=5.431 Å

11.7.10 Example 2

$\lambda = 1.542 \text{ \AA}$

Line No.	$\sin^2 \theta$	$\frac{(\sin^2 \theta)_n}{(\sin^2 \theta)_1}$	$nA + mC$	$(\sin^2)_{calc}$	hkl
1	0.0806	1.00	A+C	0.0806	101
2	0.0975	1.21	4C	0.0976	002
3	0.1122	1.39	2A	0.1124	110
4	0.210	2.61	2A+4C	0.210	112
5	0.226	2.80	4A	0.225	200
6	0.274	3.40	A+9C	0.276	103
7	0.305	3.78	5A+C	0.306	211
8	0.321	3.98	4A+4C	0.323	202

Table 13: Indexing powder patterns, example 2

Ratios → not cubic

Note Relations:

$$(4) = (2) + (3)$$

$$(5) = 2(3)$$

$$(7) = (5) + (1)$$

$$(8) = 4(1)$$

Assume Tetragonal:

$$\sin^2 \theta = A(h^2 + k^2) + Cl^2$$

Tetragonal P → (1) = 100 or 001

No peak at 2(1) → not P

$$2(1) = 110, \text{ if } (1) = 100$$

Tetragonal I: (1) = 110, 101, or 002

$$\text{Try } (1) = 101 \rightarrow \sin^2 \theta = A + C$$

$$\sin^2 \theta = A(h^2 + k^2)_n + C(l^2)_n$$

$$hk \quad 00 \ 10 \ 11 \ 20 \ 21 \ 22 \ 30 \ 31 \ 32 \dots \ l \ 0 \ 1 \ 2 \ 3 \ 4 \ \dots$$

$$h^2 + k^2 \quad 0 \ 1 \ 4 \ 5 \ 8 \ 9 \ 10 \ 13 \dots \ l^2 \ 0 \ 1 \ 4 \ 9 \ 16 \ \dots$$

$$\text{If } (1) = 101 = A + C \rightarrow (2) = 002 = 4C^*$$

$$\left. \begin{array}{l} \text{If } (1) = 002 = 4C \rightarrow (2) = 101 = A + C \\ \text{If } (1) = 110 = 2A \rightarrow (2) = 101 = A + C \end{array} \right\} \text{Think about it}$$

Try:

$$\left. \begin{array}{l} (2) \rightarrow 4C = 0.0975 \\ (1) \rightarrow A + C = 0.083 \end{array} \right\} A = 0.0562, C = 0.0244$$

$$\text{Note } (3) = 2A \rightarrow 110 = A(1^2 + 1^2) + C(0^2)$$

Check to see if each $(\sin^2 \theta)_n = A(h^2 + k^2)_n + Cl_n^2$ for $A = 0.0652$ and $C = 0.0244$

Conclusion: Tetragonal I

Lattice constant: $a=?$ $c=?$

$$(2) \rightarrow 2c^* = \frac{2}{c} = \frac{2 \sin \theta_{002}}{\lambda} \Rightarrow c = \frac{\lambda}{\sin \theta_{002}} = \frac{1.542 \text{\AA}}{(0.0975)^{\frac{1}{2}}} = 4.94 \text{\AA}$$

$$(3) \rightarrow \sqrt{2}a^* = \frac{\sqrt{2}}{a} = \frac{2 \sin \theta_{110}}{\lambda} \Rightarrow a = \frac{\lambda}{\sqrt{2} \sin \theta_{110}} = 3.62 \text{\AA} \quad \text{Indium}$$

Procedure for hexagonal similar to tetragonal except:

$$(\sin^2 \theta)_n = A(h^2 + k^2 + hk)_n + l^2 C$$

$$\text{where } h^2 + k^2 + hk = \{0, 1, 3, 4, 7, 9, 12, 13, \dots\}$$

Indexing difficulty increases as crystal symmetry decreases: need computer

Note: When $K\alpha_1$ and $K\alpha_2$ are unresolved (at lower 2θ), use weighted average $\lambda_{K\alpha} = 2/3\lambda_{K\alpha 1} + 1/3\lambda_{K\alpha 2} = 1.5418 \text{\AA}$

At higher 2θ , $K\alpha_1$ and $K\alpha_2$ may be resolved, use correct $\lambda_{K\alpha 1}$ and $\lambda_{K\alpha 2}$, not $\lambda_{K\alpha}$

11.7.11 Quantitative Analysis

Recall: $I_{hkl} = C|F_{hkl}|^2 \frac{m_{hkl}}{V_C^2} LP \frac{A}{2\mu}$, ignore e^{-2M}

Consider a 2 phase powder with:

v_A = volume fraction of phase A, $1 - v_A = v_B$ = volume fraction of phase B

Phase A diffraction peaks

$$I_A = C \left[|F_{hkl}|^2 \frac{m_{hkl}}{V_C^2} LP \right]_A v_A \frac{A}{2\mu} = CK_A v_A \frac{A}{2\mu} \quad (11.27)$$

K_A varies with hkl

μ varies with v_A

Phase B diffraction peaks

$$I_B = CK_B(1 - v_A) \frac{A}{2\mu} \quad (11.28)$$

μ is the same

Hence,

$$\frac{I_A}{I_B} = \frac{K_A}{K_B} \frac{v_A}{(1 - v_A)} \quad (11.29)$$

To determine the volume fraction for a mixture of 2 powder crystalline phases A&B

$$\frac{I_A}{I_B} = \underbrace{\frac{K_A}{K_B}}_{\text{measure}} \underbrace{\frac{v_A}{(1 - v_A)}}_{\text{determine } v_A} \quad \text{calculate} \quad (11.30)$$

The relative intensities of peaks for each phase should be checked to ensure an ideally random powder sample. **Texture** will cause errors in quantitative analysis.

In the analysis of the integrated area under the diffraction peaks, the Debye-Waller factor, e^{-2M_A} ; e^{-2M_B} , may be included if known. The two different phases are made up of atoms in two different lattices with different vibrational amplitudes. The vibrational amplitude M is given by the following:

$$M = \frac{2\pi^2 \langle u_{hkl}^2 \rangle}{d_{hkl}^2} \quad (11.31)$$

Here $\sqrt{\langle u_{hkl}^2 \rangle}$ is the root-mean-square (rms) vibrational amplitude in the hkl direction. These vibrations are typically isotropic with a magnitude of $\approx 0.1\text{\AA}$. An increase in temperature increases the vibrational amplitude of atoms.

11.8 Rotating Crystal Method

In the **rotating crystal method**, a single crystal is mounted with an axis that is normal to a monochromatic beam. A cylindrical film encloses the single crystal, which records a diffraction pattern as the crystal is rotated. This setup is illustrated in Figure 11.25. Whereas older films required chemical exposure to develop, X-ray sensitive image plates are used today, and diffraction patterns are read out by a laser.

In this procedure, the crystal is rotated smoothly about a chosen axis that coincides with the axis of the film cylinder and different planes cause diffraction peaks at points in the rotation. Diffraction peaks occur when a set of lattice planes make the correct Bragg angle for reflection. In the setup illustrated in Figure 11.25, prior to inserting the crystal in the camera, the c -axis of the crystal's unit cell was determined and the crystal is then rotated about this axis. Due to this rotation about the c -axis, the spots appear in layers with heights according to constant l index values. All of the center spots are $hk0$.

The rotating crystal method helps determine the structure of a crystal in an organized manner, and is useful for methods where a single crystal can be attained as well as when the c and c^* axes of a crystal's unit cell coincide with each other.

11.8.1 Rotating Crystal Method

1. Monochromatic X-ray beam diffraction from single crystal surrounded by film cylinder.
2. The crystal continually rotated about the axis that coincides with film cylinder axis
3. If rotation axis = unit cell axis (e.g., \bar{c}) then reflection pattern (spots) on film form circles at heights corresponding to constant (e.g., l)
 - ◊ This is for unit cells where $\bar{c}^* \parallel \bar{c}$

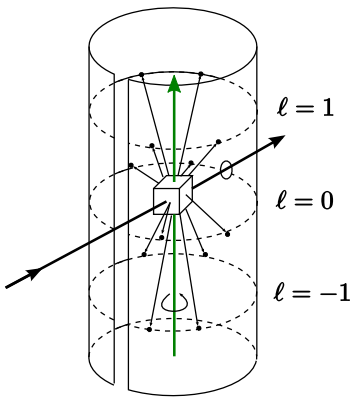


Figure 11.25: Rotating crystal method using a cylindrical camera.

Figure 11.26 below illustrates a developed rotating-crystal film of a quartz crystal. The extra streaks around the center of the pattern are due to Bremsstrahlung radiation not removed by the filter.

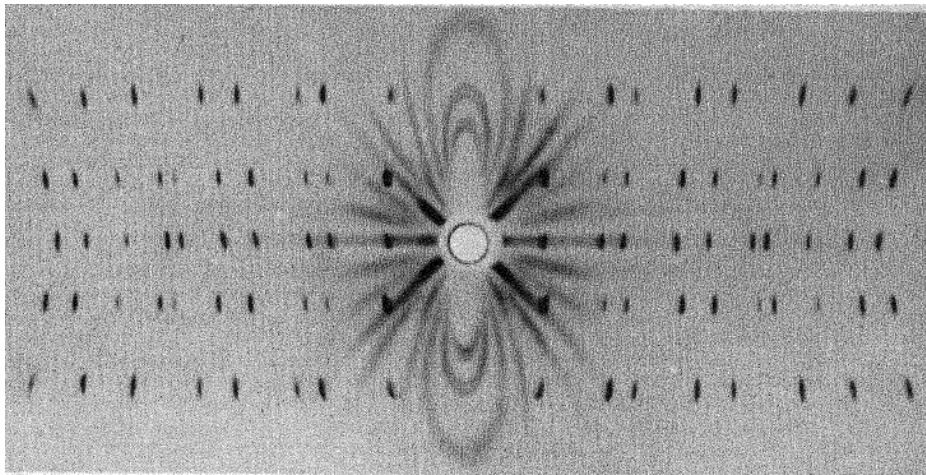


Figure 11.26: Rotating-crystal pattern of a quartz crystal (hexagonal) rotated about its c axis. Filtered copper radiation. (Courtesy of B.E. Warren.)

11.8.2 Reciprocal Lattice Treatment of Rotating-Crystal Method

How do we picture the rotating-crystal method in reciprocal space? Visualizing the method in reciprocal space, the Ewald sphere is the instrument, and the reciprocal lattice structure is the crystal sample. An orthorhombic crystal centered at the Ewald sphere may be rotated about the c -axis, as illustrated in Figure 11.27. Recall that the incident wave vector always points from the center of the Ewald sphere to the origin of the reciprocal lattice. If the crystal is rotating about the c -axis, then reciprocal lattice rotates about its \bar{c}^* or \bar{b}_3 axis. A diffraction peak will appear when a reciprocal lattice point touches the Ewald sphere. In this camera,

all diffracted beams will be detected and recorded except those that travel close to the cylinder's central axis and miss the film.

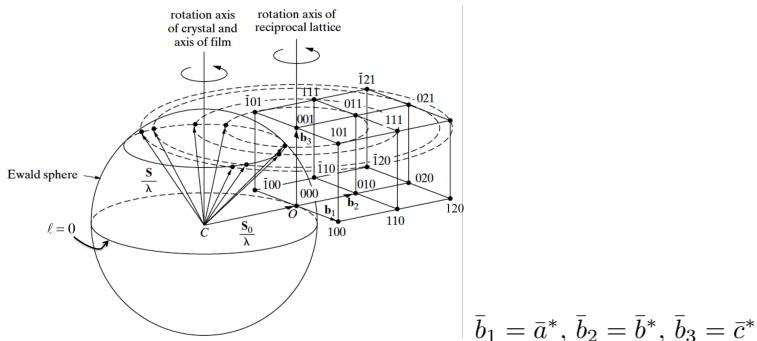


Figure 11.27: Rotating crystal method in reciprocal space

- ◊ The reciprocal lattice rotates about $\bar{r}_{100}^* = \bar{c}^*$ as the crystal rotates about \bar{c} .
- ◊ Spots appear on the film when reciprocal lattice points coincide with the Ewald sphere.
- ◊ Recall the Laue condition, when $\frac{\bar{S}}{\lambda} - \frac{\bar{S}_0}{\lambda} = \bar{Q} = \bar{r}_{hkl}^*$

We will divide the scattering vector into horizontal and vertical components, \bar{r}_H^* and \bar{r}_V^* . The α and β angles determine the in plane and out of plane components of \bar{r}_{hkl}^* .

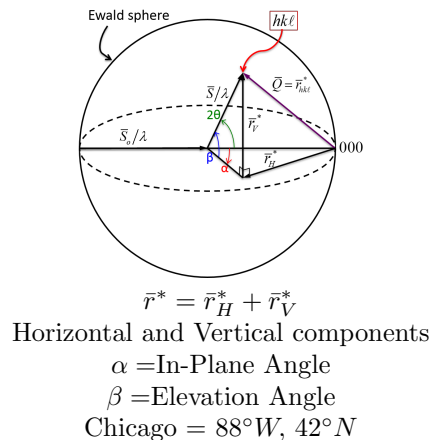


Figure 11.28: Ewald sphere geometry

After the scattered diffracted beam places various spots on the film, the film is unrolled and the specific x and y coordinates of these characteristic spots are noted. Using these coordinates and the radius of the cylinder, α and β may be determined using the following equations:

$$\tan\beta = y/R \quad (11.32)$$

$$\alpha = x/R \quad (11.33)$$

$$|\vec{r}_V^*| = \left(\frac{1}{\lambda}\right) \sin\beta \quad (11.34)$$

$$|\vec{r}_H^*| = |h\vec{a}^* + k\vec{b}^*|^2 = \frac{1}{\lambda^2} [2(1 - \cos\alpha \cos\beta) - \sin^2\beta] \quad (11.35)$$

Example: $\lambda = 1.542\text{\AA}$, $a^* = 0.25\text{\AA}^{-1}$, $b^* = 0.15\text{\AA}^{-1}$, $c^* = 0.36\text{\AA}^{-1}$, and $R = 50$ mm

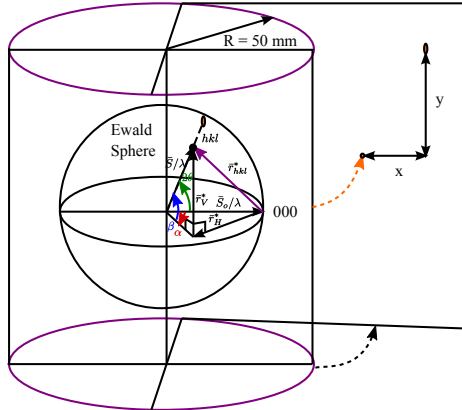


Figure 11.29: Convert x,y coordinates of film spot to α, β

11.8.3 Ewald Construction for Rotating Crystal Method

In the rotating crystal method, the diffraction spot positions (x, y coordinates) are experimentally determined and the film cylinder radius is known. The y coordinate gives the layer line, such as $l = 0, l = \pm 1$, etc. and the x coordinate indicates where this spot is located on the layer line. Using these values, we can determine the in-plane (α) and elevation (β) angles, as well as information about the scattering vector which is coincident with the reciprocal lattice vector for a diffraction spot. Geometric relationships using the Ewald sphere are pictured in Figure 11.20 below.

Define angles:

$$\alpha = x/R \rightarrow \text{in-plane angle}$$

$$\tan\beta = y/R \rightarrow \text{elevation angle}$$

$$\text{Separate } \vec{r}_{hkl}^* = \vec{r}_H^* + \vec{r}_V^*$$

$$|\vec{r}_V^*| = \left| \frac{\vec{S}}{\lambda} \right| \sin \beta \rightarrow \lambda r_V^* = \sin \beta$$

Note: $\cos 2\theta = \cos \alpha \cos \beta$

$$\lambda^2(r_H^*)^2 = 2(1 - \cos \alpha \cos \beta) - \sin^2 \beta$$

Bragg's law below

$$(r_{hkl}^*)^2 = (r_H^*)^2 + (r_V^*)^2 = \frac{4 \sin^2 \vartheta}{\lambda^2}$$

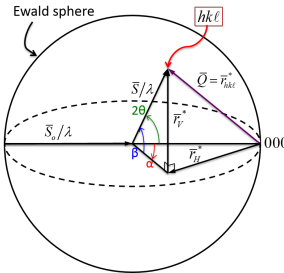


Figure 11.30: Ewald sphere for rotating crystal method

A. For hexagonal, tetragonal, cubic, orthorhombic, etc., where \bar{c} coincides with \bar{c}^* , measuring the y coordinate allows us to calculate the elevation angle, and the vertical component of the scattering vector $y \rightarrow \beta \rightarrow r_V^* \Rightarrow r_{00l}^* \rightarrow c$ determined directly

By remounting the crystal to rotate about \bar{a} or \bar{b} , we can determine a and b .

B. Indexing a reflection in layer line

For a given layer line, β is constant.

$$\vec{r}_H^* = h\bar{a}^* + k\bar{b}^* \text{ for } l = \text{constant layer line}$$

$$\lambda^2(r_H^*)^2 = [h^2(a^*)^2 + k^2(b^*)^2 + 2hka^*b^* \cos \gamma^*] \lambda^2$$

$$= 2(1 - \cos \alpha \cos \beta) - \sin^2 \beta$$

$$\alpha = x/R \tan \beta = y/R$$

$$\therefore x, y \rightarrow r_H^*, r_V^*$$

11.8.4 Bernal Chart

The **Bernal chart** is a graphical method that aids in the conversion the x and y coordinates of diffraction spots to λr_H^* , λr_V^* . This graphical aid can be superimposed on the film roll, as shown in Figure 11.31 below.

Graphical method for converting $x, y \rightarrow \lambda r_H^*, \lambda r_V^*$

Horizontal Lines \rightarrow constant l for \bar{c} axis rotating λr_H^* lines equally incremented from 0 to 2.0. The maximum is when $2\theta = \pi$ $\lambda r_H^* = 0 \rightarrow x = 0 \rightarrow \alpha = 0 \rightarrow h = 0$ $\lambda r_H^* = 2 \rightarrow x = \pi R \rightarrow \alpha = \pi \rightarrow r^* = r_H^* = \frac{2}{\lambda}$ for $l = 0$

Start with $l = 0$ layer

- ◊ Assume $a^* = b^*, \gamma^* = 90^\circ \rightarrow \frac{1}{a}(h^2 + k^2)^{\frac{1}{2}}$
- ◊ Assume $a^* \neq b^*, \gamma^* = 90^\circ \rightarrow r_H^* = \left(\frac{h^2}{a^2} + \frac{k^2}{b^2} \right)^{1/2}$

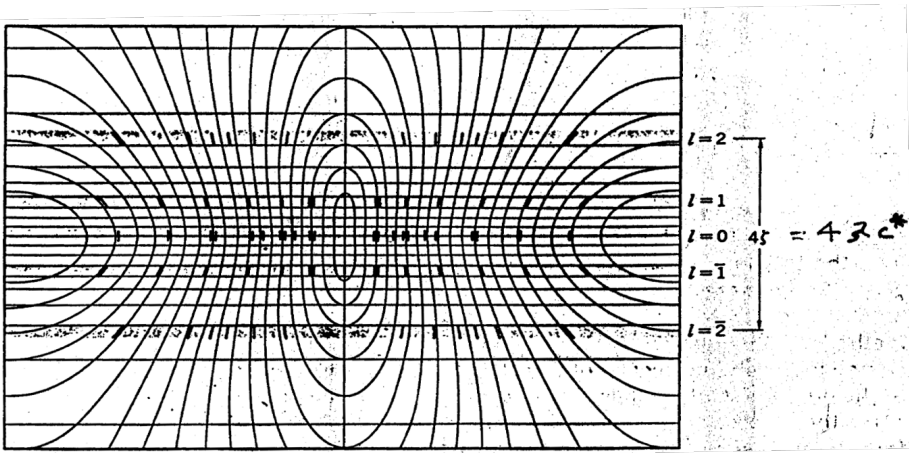
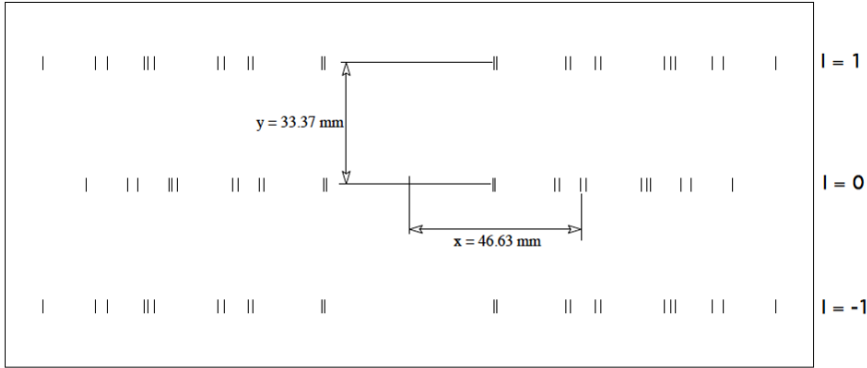


Figure 11.31: Schematic view of film overlain on a Bernal chart. Note that the X-ray diffraction spots lie along rows of constant ξ and ζ . (Only a few possible reflections are indicated)

Figure P2 C-axis-rotation photograph for 361 HW
(scale is approx 1:1)



Radius of the cylindrical camera = 50 mm

x-ray wavelength $\lambda = 1.542 \text{ \AA}$

$a^* = 0.25 \text{ \AA}^{-1}$, $b^* = 0.15 \text{ \AA}^{-1}$, $c^* = 0.36 \text{ \AA}^{-1}$

Figure 11.32: C-axis rotation photograph

Once the lattice constants and orthorhombic unit cell have been determined, index and determine Lattice Type: P, I, C, F.

Measure X and Y from the film

$$R = 50 \text{ mm}, \lambda = 1.542 \text{ \AA}$$

$$\text{For } l = 0 \text{ layer, } \rightarrow \beta = 0 \rightarrow r_H^* = \frac{1}{\lambda} \sqrt{2(1 - \cos \alpha)}$$

X [mm]	$\alpha = X/R$	$\alpha [^\circ]$	$r_H^* [\text{\AA}^{-1}]$	hkl
22.4	0.488	25.67	0.288	110
23.3	0.466	26.70	0.299	020
39.6	0.792	45.38	0.500	200
40.8	0.816	46.75	0.515	130
46.6	0.932	53.40	0.583	220
48.1	0.962	55.12	0.600	040
63.1	1.262	72.31	0.765	310
64.6	1.292	74.03	0.781	240
65.5	1.31	75.06	0.790	150
74	1.48	84.80	0.875	330
76.7	1.534	87.89	0.900	060
88	1.76	100.84	1.000	400

r_H^* defines radius of circle in the $l = 0$ reciprocal space plane

Table 14: Conversion of X to hkl

Figure 11.33 below demonstrates the graphical solution for layer $l = 0$.

Plot hk0 lattice: $a^* = 0.25\text{\AA}^{-1}$ & $b^* = 0.15\text{\AA}^{-1}$

Plot circles with radii r_H^* , shown in Figure 11.33 below.

The blue squares represent the reciprocal lattice points corresponding to the planes that caused diffraction to occur.

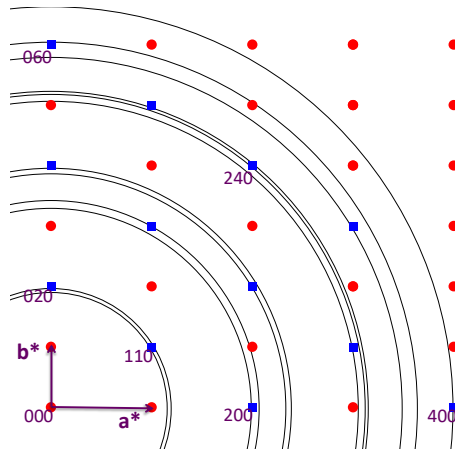


Figure 11.33: Graphical Solution for $r_H^* = h^2 a^*^2 + k^2 b^*^2$

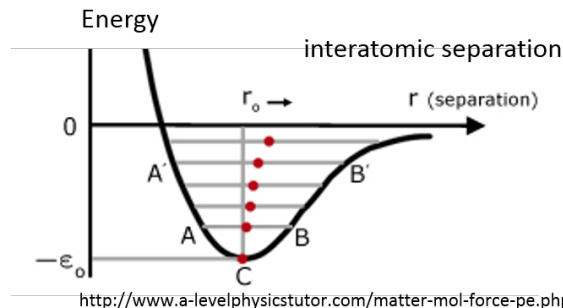
Repeat this procedure for $l = 1$ layer $\rightarrow \beta = \tan^{-1}(y/R)$

$$r_H^* = \frac{1}{\lambda} \sqrt{2(1 - \cos\alpha \cos\beta - \sin^2\beta)} \quad (11.36)$$

12 Temperature Effects

The atoms in a crystal vibrate about equilibrium lattice positions, even at 0°K, and the vibrational amplitudes increase as temperature increases. With increasing atomic kinetic energies, the unit cell expands, and the lattice constant becomes greater. This temperature effect, also known as the Debye-Waller effect, affects the area under diffraction peaks even at room temperature. It is important to account for this effect since the area under diffraction peaks gives information about the crystal structure via the structural factor.

Figure 12.1 illustrates a simple model of interatomic spacing in a crystal as a function of energy, in which the red dots indicate the average interatomic distance. Note that as temperature and energy increase, the width of the potential well widens to the right, towards a greater separation distance. An increase in temperature leads to a sampling of higher energies in the potential well and a lattice expansion, as indicated by the red dots in the plot. The width bounded by the two walls of the potential also increases, allowing the atoms to take greater path lengths and have greater vibrational amplitudes.



<http://www.a-levelphysicstutor.com/matter-mol-force-pe.php>

Figure 12.1: A simplified description of the potential well for bonding two neighboring atoms. There is a hard-sphere repulsion due to Pauli-exclusion at short interatomic separation. The widening of the well as kinetic energy (temperature) increases leads to increased vibrational amplitude. The asymmetry of the well leads to thermal expansion as temperature increases.

12.1 Describe a crystal in terms of a primitive unit crystal.

Considering a crystal of M primitive unit cells, the \bar{R}'_m will replace the former lattice point position vector, which now includes an extra factor - a time-dependent displacement vector for each atom.

- ◊ For simplicity sake, we will assume one atom per lattice point at the origin
- ◊ Let $M = M_1 M_2 M_3 = \# \text{ of unit cells}$
- ◊ Let $m = \{m_1 m_2 m_3\} = \text{unit crystal index}$
- ◊ Let $\bar{R}_m = \text{lattice point position vector to locate origin of the } m^{\text{th}} \text{ unit cell}$
- ◊ Let $\bar{R}'_m(t) = \bar{R}_m + \underbrace{\bar{\Delta}_m(t)}_{\triangleq \text{instantaneous displacement changing in time}}$

Atoms can vibrate longitudinally or transversely, as shown in the figures below.

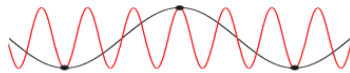


Figure 12.2: Transverse Wave

The summation of the coherently scattered wave intensities in electron units from M atoms for a crystal with one atom per unit cell is given by the following:

$$I_{(eu)}(\bar{Q}) = \left[\sum_m^M f_m e^{2\pi i \bar{Q} \cdot \bar{R}'_m} \right] \left[\sum_m^M f_m e^{-2\pi i \bar{Q} \cdot \bar{R}'_m} \right] = \sum_m^M \sum_n^M f_m f_n e^{2\pi i \bar{Q} \cdot (\bar{R}'_m - \bar{R}'_n)} \quad (12.1)$$

Assuming all of the atoms are the same, the f_m and f_n terms may be factored out of the summation. Adding in the time-dependent Debye-Waller factors yields the following:

$$I_{(eu)}(\bar{Q}) = f^2 \sum_m \sum_n e^{2\pi i \bar{Q} \cdot (\bar{R}_m - \bar{R}_n)} e^{2\pi i \bar{Q} \cdot (\bar{\Delta}_m - \bar{\Delta}_n)} \quad (12.2)$$

Recall that \bar{Q} is the scattering vector coincident with \bar{r}_{hkl}^* under the hkl Bragg diffraction (or Laue) condition.

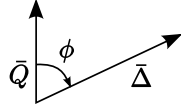


Figure 12.3: Scattering vector and Δ

$$\bar{Q} \cdot \bar{\Delta}_m = \frac{2 \sin \theta}{\lambda} \Delta_m \cos \phi_m \quad (12.3)$$

u_m is the projection of the instantaneous displacement vector along the scattering vector's direction:

$$u_m = \Delta_m \cos \theta_m \quad (12.4)$$

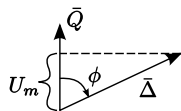


Figure 12.4: u_m

Note that $u_m = 0$ for longitudinal wave along diffraction plane.

Using $2\pi Q = \frac{4\pi \sin \theta}{\lambda} = q$, the intensity equation is the following:

$$I_{(eu)}(\bar{Q}) = f^2 \sum_m \sum_n e^{2\pi i \bar{Q} \cdot (\bar{R}_m - \bar{R}_n)} e^{iq(u_m - u_n)}$$

Note that $\Delta_m; u_m$ are instantaneous vibrational displacements that occur in a phonon lifetime which is on the order of $\sim 10^{-14}$ seconds, and the intensity measurement time is $\gtrsim 10^{-3}$ seconds. Therefore, a time average of these instantaneous intensities as affected by vibrational effects is used.

The function is integrated over a period of time T that is long relative to the fluctuations and is normalized by dividing by T .

$$\langle f(t) \rangle = \frac{1}{T} \int_0^T f(t) dt \quad (12.5)$$

The time-averaged intensity is indicated by bracket notation:

$$\langle I_{(eu)} \rangle = f^2 \sum_m \sum_n e^{2\pi i \bar{Q} \cdot (\bar{R}_m - \bar{R}_n)} \langle e^{iq(u_m - u_n)} \rangle \quad (12.6)$$

Simplifying, by Maclaurin series expansion:

$$e^{ix} = \sum_{n=0}^{\infty} \frac{i^n x^n}{n!} = 1 + ix - \frac{x^2}{2} - \frac{ix^3}{6} + \dots \quad (12.7)$$

$$\langle e^{iq(u_m - u_n)} \rangle = 1 + iq \langle u_m - u_n \rangle - \frac{q^2}{2} \langle (u_m - u_n)^2 \rangle - \dots \quad (12.8)$$

$$\approx 1 - \frac{q^2}{2} \langle (u_m - u_n)^2 \rangle = e^{-\frac{q^2}{2} \langle (u_m - u_n)^2 \rangle} = e^{-\frac{q^2}{2} \langle u_m^2 + u_n^2 - 2u_m u_n \rangle} \quad (12.9)$$

$$\langle u_m^2 \rangle = \langle u_n^2 \rangle = \langle u^2 \rangle \quad (12.10)$$

$$\Rightarrow \quad (12.11)$$

$$\langle e^{iq(u_m - u_n)} \rangle \approx e^{-q^2 \langle u^2 - u_m u_n \rangle} \quad (12.12)$$

Let

$$\langle u_m u_n \rangle = \underbrace{\alpha_{mn}}_{\text{correlation function}} \langle u^2 \rangle \quad (12.13)$$

which accounts for the correlation of vibrational motion between the atoms, and may range from 0 to 1.

$$\langle e^{iq(u_m - u_n)} \rangle = e^{-q^2 \langle u^2 \rangle (1 - \alpha_{mn})} \quad (12.14)$$

and

$$\langle I_{(eu)} \rangle = \sum_m \sum_n f^2 e^{2\pi i \bar{Q} \cdot (\bar{R}_m - \bar{R}_n)} \underbrace{e^{q^2 \langle u^2 \rangle \alpha_{mn}}}_{= 1 + q^2 \langle u^2 \rangle \alpha_{mn} \text{ for } q^2 \langle u^2 \rangle \alpha_{mn} \ll 1} \quad (12.15)$$

$$= e^{-q^2 \langle u^2 \rangle} \underbrace{\sum_m \sum_n f^2 e^{2\pi i \bar{Q} \cdot (\bar{R}_m - \bar{R}_n)}}_{[CR]} + \underbrace{q^2 \langle u^2 \rangle e^{-q^2 \langle u^2 \rangle}}_{xe^{-x}} \sum_m \sum_n f^2 \alpha_{mn} e^{2\pi i \bar{Q} \cdot (\bar{R}_m - \bar{R}_n)} \quad (12.16)$$

$[CR] = \text{Crystal Reflection} = f^2[\text{3-D interference function}]$

With higher 2θ , the diffraction peak intensities decrease due to the damping term $e^{-q^2 \langle u^2 \rangle}$ at the front.

$$xe^{-x} = x(1 - x + \frac{x^2}{2} - \dots) \approx x - x^2 \approx 1 - e^{-x} = x - \frac{x^2}{2} + \frac{x^3}{6} \dots \quad (12.17)$$

$$\Rightarrow \langle I_{(eu)} \rangle = e^{-q^2 \langle u^2 \rangle} [CR] + \left(1 - e^{-q^2 \langle u^2 \rangle}\right) \sum_n f^2 \alpha_{mn} e^{2\pi i \bar{Q} \cdot (\bar{R}_m - \bar{R}_n)} \quad (12.18)$$

$$q^2 \langle u^2 \rangle = (2\pi Q)^2 \langle u^2 \rangle = 2B \left(\frac{\sin\theta}{\lambda}\right)^2 = \frac{BQ^2}{2} = 2M \quad (12.19)$$

The new term, B, is sensitive to the temperature and vibrational amplitudes. Using B, the intensity can be written as follows:

$$\begin{aligned} & \text{Thermal diffuse factor increases with } Q \\ \Rightarrow \langle I_{(eu)} \rangle &= \underbrace{e^{\frac{-BQ^2}{2}}}_{\text{attenuated sharp diffraction peaks}} [CR] + \underbrace{\left(1 - e^{-\frac{BQ^2}{2}}\right) \sum_m \sum_n f^2 \alpha_{mn} e^{2\pi i \bar{Q} \cdot (\bar{R}_m - \bar{R}_n)}}_{\text{broadened peaks centered at } \bar{Q} = \bar{r}_{hkl}^*} \quad (12.20) \end{aligned}$$

Since the correlation function is equal to unity at an atom (i.e. $\alpha_{mm} = 1$) and only has a considerable effect at a small region around an atom, the diffraction peaks in the second summation are broadened. Recall that a smaller number of unit cells produces broader peaks than a relatively larger amount of unit cells.

Why time average?

Because measurement time for intensity (1 sec) \gg phonon lifetime (10^{-14} sec)

Why do odd powers of $\langle u^n \rangle = 0$?

We assume about $u = 0$

The average time displacement for odd powers averages to zero, but for even powers, the area under the curve is π . This explains why even powers are present in the time-average and odd powers are not.

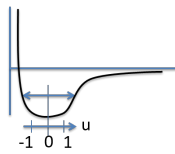


Figure 12.5: Harmonic oscillation assumes symmetric potential well

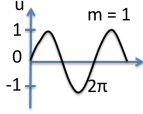


Figure 12.6: $\int_0^{2\pi} \sin(mx)dx = 0$

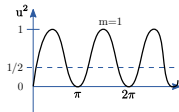


Figure 12.7: Area = $\int_0^{2\pi} \sin^2(mx)dx = \pi$

$$\text{Average} = \frac{\text{Area}}{2\pi} = \frac{1}{2}$$

12.2 Debye Theory of Lattice Dynamics/ Heat Capacity — Corrected by Waller

The quantity B, which describes the vibration of the atoms, is described by the following equation:

$$B = \frac{6h^2T}{m_A k_B \theta_D^2} Q\left(\frac{\theta_D}{T}\right) = 8\pi^2 \langle u^2 \rangle \quad (12.21)$$

where the variables are defined as follows:

- ◊ m_A = atomic mass = $A \times 1.660 \times 10^{-24} \text{g}/\text{amu}$
- ◊ h = Planck's constant = $6.628 \times 10^{-27} \text{erg} - \text{sec}$
- ◊ $T = {}^\circ \text{K}$ absolute temp
- ◊ k_B = Boltzmann's constant = $1.380 \times 10^{-16} \text{erg}/{}^\circ \text{K}$
- ◊ θ_D = Debye temperature (related to stiffness of crystal) e.g. $\theta_D^{Ge} = 360 {}^\circ \text{K}$, $\theta_D^{Al} = 394 {}^\circ \text{K}$, $\theta_D^{Si} = 625 {}^\circ \text{K}$

$Q(\theta_D/T) \approx 1$ for $T > \theta_D/2$ declines rapidly for $T < \theta_D/2$

Unvarying constants: $\frac{6h^2}{m_A K} = 1.151 \times 10^{-12} \text{cm}^2 = 1.151 \times 10^4 \text{\AA}^2/A$

$$B[\text{\AA}^2] = 1.151 \times 10^4 \frac{T[\text{K}]}{A[\text{amu}] \theta_D^2 [\text{^\circ K}]} Q\left(\frac{\theta_D}{T}\right)$$

Therefore, the mean square vibrational amplitude (assume Q=1) is given by the following:

$$\langle u^2 \rangle = \frac{B}{8\pi^2} = 145.8 \frac{T}{A\theta_D^2} [\text{\AA}^2] \quad (12.22)$$

- ◊ For Si^{28.1} ($\langle u^2 \rangle$)^{1/2} = 0.063 Å at R.T. ($T = 300^\circ\text{K}$)
- ◊ For Ge^{72.6} ($\langle u^2 \rangle$)^{1/2} = 0.068 Å at R.T. ($T = 300^\circ\text{K}$)
- ◊ For Al²⁷ ($\langle u^2 \rangle$)^{1/2} = 0.10 Å at R.T. ($T = 300^\circ\text{K}$)

Debye-Waller Factor = $e^{-2M} = e^{-BQ^2/2} = e^{-4\pi^2 \langle u_{hkl}^2 \rangle / d_{hkl}^2}$

If we look at the Debye-Waller factor in terms of real components, u_{hkl} and d_{hkl} , we see a comparison between the vibrational displacement and the d-spacing within a crystal.

For silicon, the (220) peak intensity is diminished by 4% as shown below. If we move to higher-order peaks, such as (880) with a smaller d spacing, the attenuation significantly affects the peak intensity.

- ◊ For Si (220), $d_{220} = 1.92 \text{\AA}$ $e^{-2M} = e^{-0.0425} = 0.958$ at R.T.
- ◊ For Si (880), $d_{880} = 0.48 \text{\AA}$ $e^{-2M} = (e^{-0.0425})^{16} = e^{-0.0680} = 0.506$ at R.T.

Note that the (880) d-spacing is 1/4 of the (220) d-spacing. Since the d_{hkl} is squared in the Debye-Waller factor, this causes the peak intensity of the (880) to be $\frac{1}{d_{hkl}^2} = \frac{1}{16}$ of the (220) intensity.

$$\frac{e^{-2M_{h_2 l_2 k_2}}}{e^{-2M_{h_1 k_1 l_1}}} = (e^{-2M_{h_1 k_1 l_1}})^{\overbrace{(h_2^2 + k_2^2 + l_2^2) / (h_1^2 + k_1^2 + l_1^2)}^{\text{if cubic}}} = (0.0958)^{16} = 0.503 \quad (12.23)$$

$$\langle I_{eu} \rangle = e^{-BQ^2/2}[CR] + \underbrace{(1 - e^{-BQ^2/2}) \sum_m \sum_n f^2 \alpha_{mn} e^{2\pi i \bar{Q} \cdot (\bar{R}_m - \bar{R}_n)}}_{f^2 M}$$

Note : Original Debye Theory $\alpha_{mn} = \{ 1, m=n; 0, \text{otherwise} \} = (1 - e^{-BQ^2/2})f^2 M$

Suppose we only account for the 3-D interference function and divided by f^2 . In that case, the intensity will always have an intensity of M^2 , as shown by the dashed curves in Figure 12.8. However, the Debye-Waller factor attenuates the peaks in an exponential fashion with an increasing Q , as shown by the three peaks with amplitudes following the $e^{-BQ^2/2}$ curve. Finally, the TDS increases the background and produces broad peaks below the sharp Bragg peaks, but this effect is exaggerated in the figure below.

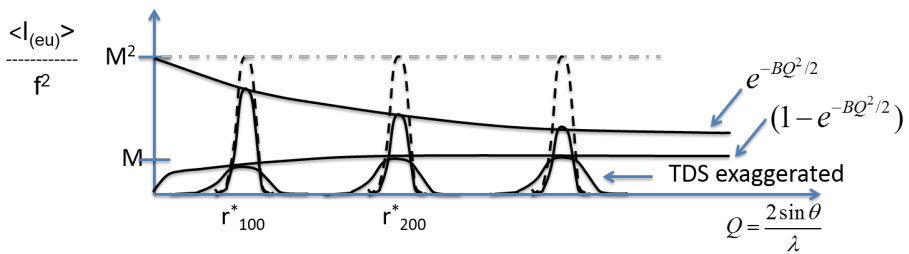
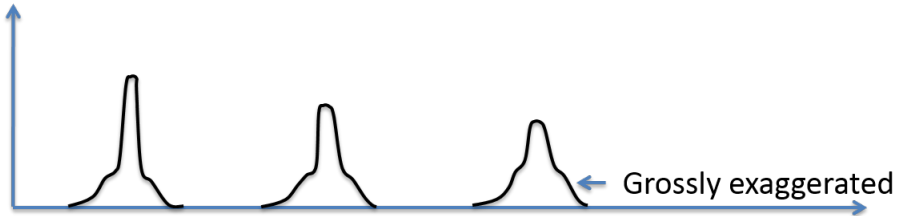
Figure 12.8: Intensity as a function of Q 

Figure 12.9: Intensity with temperature effects

12.3 Symmetrical Reflection Powder Diffraction

$$P' = \frac{I_0 l}{16\pi R} r_e^2 \frac{\lambda^3}{V_c^2} m_{hkl} |F_{hkl}|^2 e^{-2M} (LP) \frac{A}{2\mu} = C(LP) m_{hkl} |F_{hkl}|^2 e^{-2M} \quad (12.24)$$

The intensities are multiplied by the Debye-Waller factor - $e^{-2M} = e^{-BQ^2/2}$, therefore as Q increases, the integrated peak intensities diminish.

M depends on:

- ◊ crystal type (Si, Ge, etc.)
- ◊ direction of r_{hkl}^* (anisotropic crystals) - network of “springs” different in different directions, such as graphite
- ◊ d-spacing $\sim 1/r_{hkl}^*$
- ◊ Temp. T
- ◊ Crystal bonding (covalent, molecular, etc.)

“B” can be measured by comparing integrated intensity of hkl to $2h 2k 2l$ reflection, Measuring B is like measuring bonding properties and temperature effects.

$$\text{For } h k l \ P'_1 = C m_{hkl} e^{-BQ_1^2/2} |F_{hkl}|^2 (LP)_1$$

$$\text{For } 2h 2k 2l \ P'_2 = C m_{hkl} e^{-BQ_2^2/2} |F_{2h2k2l}|^2 (LP)_2$$

$$\frac{P'_1}{P'_2} = \frac{(LP)_1}{(LP)_2} \frac{|F_{hkl}|^2}{|F_{2h2k2l}|^2} e^{2BQ_1^2/2} \text{ Since } Q_2 = 2Q_1 \ Q_2^2 = 4Q_1^2$$

All of the above are known, except B $B = 8\pi^2 \langle u^2 \rangle$ where, u is the vibrational amplitude around a given atom.

13 Thin Film X-ray Scattering

The growth of single-crystal epitaxial thin films is at the heart of many different types of electronic, magnetic, and optical device technologies. This type of epitaxy starts with an atomically clean, supporting, single-crystal substrate surface that forms a 2D lattice closely matching that of the film and thereby providing a template for controlling the crystallographic growth direction of the film. Chemical vapor deposition (CVD) and physical vapor deposition (PVD) are typically used for growing epitaxial films.[?]

Low-angle X-ray reflectivity (XRR) characterizes the film electron density, thickness, and interfacial roughnesses. High-angle X-ray scattering defines the film's crystal structure, determines the orientation of the film's crystallographic axes relative to those of the substrate, measures the strain induced in the film by the lattice mismatch at the interface, and determines the film's single crystal domain size.

Most single crystal epitaxial films have a low-indexed growth direction that matches the hkl surface normal of their supporting substrate, such as 001 , 110 , or 111 . The specular scattered intensity from the thin film is directly related to the 1D interference function as it senses the projection of the electron density along the surface normal, **z**-axis. In this specular geometry, the scattering vector **q** points along the surface normal direction. In this chapter we will use small **q**, instead of big **Q**. Where

$$q = 2\pi Q = \frac{4\pi \sin \theta}{\lambda}$$

$\theta = \frac{1}{2}$ of the scattering angle 2θ

An incident wave vector and a scattered wave vector, as well as the scattering vector are illustrated in Figure below.

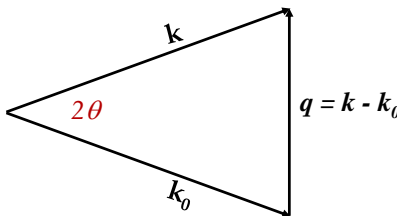


Figure 13.1: Reciprocal space vector diagram defining the scattering vector \bar{q} .

13.1 1-D interference function

If there are N scattering points along a line with period d and the scattering vector \mathbf{q} is parallel to this line, the scattered intensity from these points is

$$I(q) = \frac{\sin^2(Nqd/2)}{\sin^2(qd/2)}. \quad (13.1)$$

Note that the function peaks at N^2 , as shown in Figure 13.2. The Bragg peak half width full max and the period of the Laue fringes come from the period of the numerator, given by $\Delta q = 2\pi/t$. Where $t = Nd$.

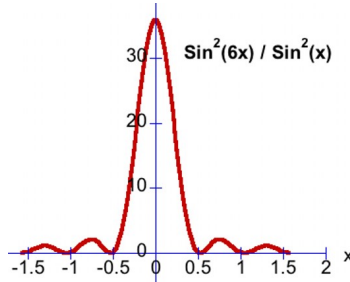


Figure 13.2: 1-D interference for $N=6$ unit cells. $x = qd/2$.

- ◊ Peak intensity $\propto N^2$
- ◊ Denominator $\rightarrow 0 \rightarrow$ Bragg peaks
- ◊ Numerator $\rightarrow 0 \rightarrow$ Bragg peak width
- ◊ Crystal size (thickness) $= Nd = t$
- ◊ Bragg peak HWFM = Fringe period = period of the numerator $= \Delta q = 2\pi/t$
- ◊ Bragg peak area $\propto N$

13.2 HRXRD of single crystal Ferro-Electric Ultra-Thin Film

In the following high-resolution X-ray diffraction (HRXRD) experiment from Thompson et al.,[?] a $PbTiO_3$ film was grown epitaxially by CVD on a $SrTiO_3(001)$ substrate. While the two perovskite lattices have the same in-plane lattice constant, their out-of-plane lattice constants differ by 6 %, which causes their respective Bragg peaks to appear at different q values in a $\theta - 2\theta$ specular scan.

At the 001 Bragg peak $\rightarrow d_{001} = c = \frac{2\pi}{q_{peak}}$

$SrTiO_3$ is cubic with $a = c = 3.905\text{\AA}$

$PbTiO_3$ is tetragonal with $a = 3.905\text{\AA}$ and $c = 4.135\text{\AA}$

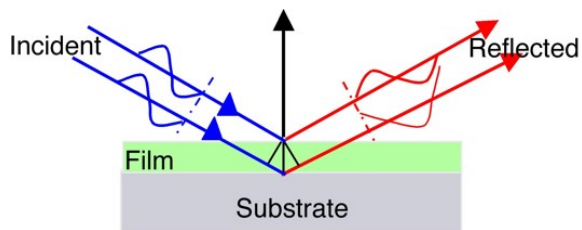


Figure 13.3: Thin film scattering in specular geometry.

The following figure shows the reflectivity from this thin film collected in a $\theta - 2\theta$ scan through the (001) peaks of the $SrTiO_3$ substrate and $PbTiO_3$ thin film. The strontium titanate is like a semi-infinite crystal, therefore yielding a very narrow delta function-like Bragg peak. As predicted in the previous section, the broad $PbTiO_3$ peak has a FWFM that is twice the width of the subsidiary peaks (Laue fringes). From this, we can calculate the film thickness as

$$t = \frac{2\pi}{\Delta q} = \frac{2\pi}{0.063\text{\AA}^{-1}} = 99\text{\AA} \rightarrow N = 24 \text{ unit cells thick.}$$

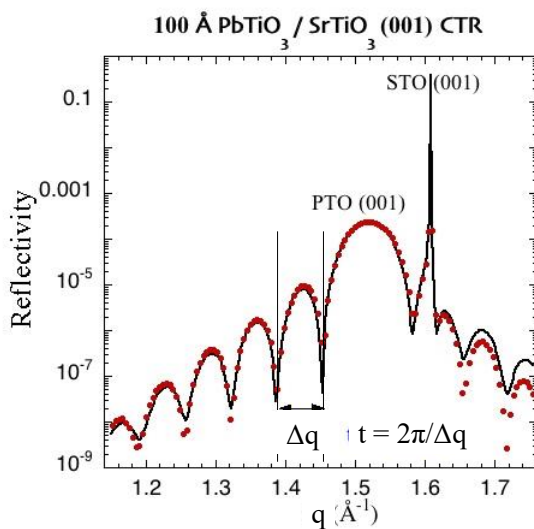


Figure 13.4: Reflectivity from $PbTiO_3$ film grown on $SrTiO_3(001)$.

As illustrated in Figures 13.5 and 13.6, $PbTiO_3$ is a ferroelectric with the center of its Pb and Ti cation sublattices offset along the c-axis from the center of its O anion sublattice. Two energy-equivalent domains can form: polarized up or polarized down. $PbTiO_3$ transforms from ferroelectric to paraelectric when the temperature goes above $490^\circ C$. Single c-domain films can be grown on $SrTiO_3(001)$ for thicknesses less than 700\AA .

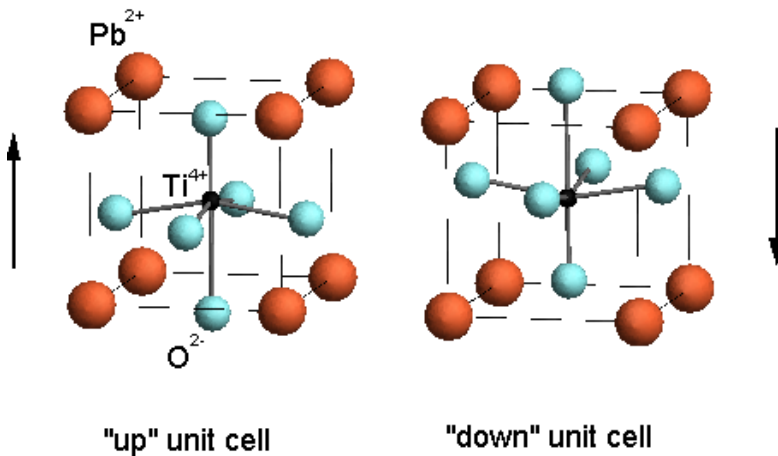


Figure 13.5: Tetragonal $PbTiO_3$ perovskite crystal structure with electric dipole polarized up or down.

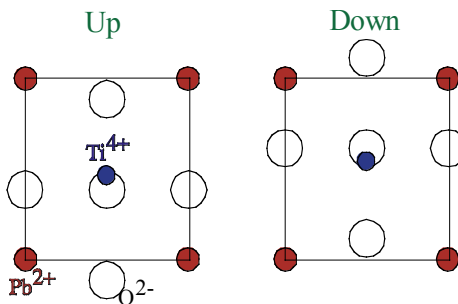


Figure 13.6: b-axes projections of polarized up and polarized down $PbTiO_3$ crystal structure.

Can the measured reflectivity be used to determine the polarization direction of the film? Note that the y-axis scale in Fig. 13.4 is on an absolute reflectivity scale. The reflected counts per second into the detector were divided by the counts per second in the straight-through beam at $2\theta = 0$ with the sample out of the beam.

In determining the structure factor, the exact positions of the atoms must be known.

13.3 Friedel's Law

If X-ray Absorption is neglected, then $F_{-H} = F_{H^*}$

$PbTiO_3$

3.9051 3.9051 4.156 90.0 90.0 90.0

400.

1.0 1.0 1.0

3 1 1 1

Atoms in basis # 1

Pb

82 1.000

1

0.00 0.00 0.1159

Atoms in basis # 2

Ti

22 1.000

1

0.500 0.500 0.5769

Atoms in basis # 3

O

08 1.000

3

0.50 0.00 0.5

0.50 0.5 0.00

0.0 0.50 0.50

13.4 Experimental Reflectivity along the (00L) Crystal Truncation Rod (CTR) for ferro-electric PZT thin-film capacitor heterostructure

$$PZT = Pb(Zr_{0.3}Ti_{0.7})O_3$$

In Figure 13.7, the experimentally measured X-ray reflectivity of the PZT capacitor structure is taken at $\lambda = 0.914\text{\AA}$. The inset shows the layers within the heteroepitaxial structure, a $SrTiO_3(001)$ substrate, a 136-nm-thick $SrRuO_3$ bottom electrode, a 20-nm-thick PZT film and a 30-nm-thick Ag top electrode. The angle positions for the three distinct (001) Bragg peaks mark off the the three distinct c lattice constants of $SrTiO_3$, $SrRuO_3$, and PZT.

$$c = 3.905, 3.970, 4.130\text{\AA}$$

The two patterns of oscillation are due to the thickness of the $SrRuO_3$ and PZT films, where the smaller period oscillation belongs to the thicker film. The Ag top electrode has a polycrystalline structure and does not measurably contribute to the scattered intensity in this high-resolution scan.

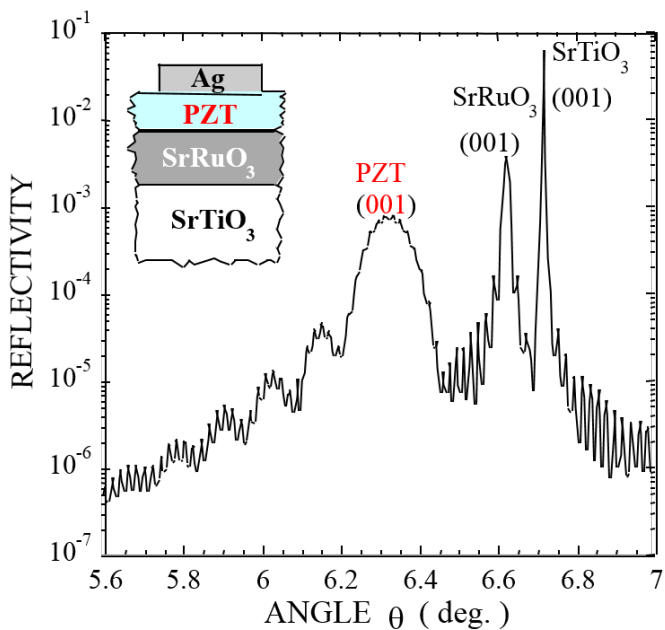


Figure 13.7: Reflectivity of PZT thin film

As predicted by the numerator of the interference function, the widths of the peaks and their Laue fringes are inversely proportional to the film thickness.

$$t = 2\pi/\Delta q = \lambda / \underbrace{(2\Delta_\theta)}_{\hookrightarrow \text{radians}} \cos\theta \quad (13.2)$$

$$q = \frac{4\pi \sin\theta}{s^2} \quad (13.3)$$

$$\Delta q = \frac{4\pi \cos\theta \Delta\theta}{s^2} \quad (13.4)$$

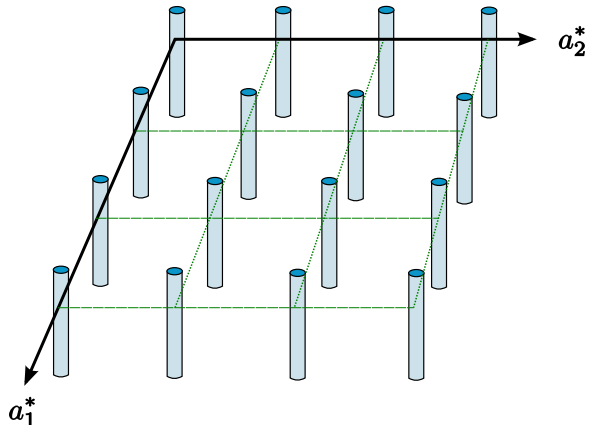
What about diffraction from 2D crystals?

In one dimension, there is a set of periodic scatterers and in reciprocal space, there exists a set of parallel periodic planes with a $\frac{1}{a}$ spacing. In two dimensions, there are two constants for the Laue condition, yielding a net of parallel rods in reciprocal space as shown in Figure 13.8.

Crystal D	Real-Space Basis	Laue Condition	Recip. Space Periodicity
1D	a	$ha^* = \text{const.}$	\parallel planes, $\perp a$
2D	a_1, a_2	$h\bar{a}_1^* = \text{const.}$ $k\bar{a}_2^* = \text{const.}$	\parallel rods, $\perp a_1 a_2$ plane
3D	a_1, a_2, a_3	$h\bar{a}_1^* = \text{const}$ $k\bar{a}_2^* = \text{const.}$ $l\bar{a}_3^* = \text{const.}$	points

Table 15: Real Space \Leftrightarrow Reciprocal Space**From 1D Laue Condition:**

h^{th} diffraction peak at $Q = ha^* \rightarrow Qa = h \rightarrow h\lambda = 2a \sin \theta_h$

**Figure 13.8:** 2D Reciprocal Space Periodicity

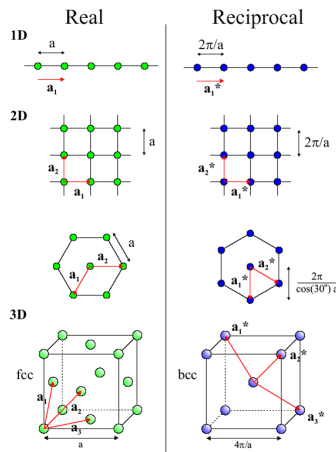


Figure 13.9: Real \Leftrightarrow Reciprocal Space (From Ref. [?])

2D crystal diffraction can be explained in reciprocal space by combining the $\frac{1}{\lambda}$ radius Ewald sphere with the set of rods depicted in Figure 13.8. The Ewald sphere center (C) connects to the k-space origin by the incident wave-vector k_0 .

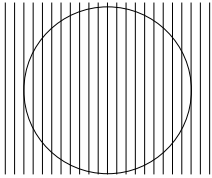


Figure 13.10: Ewald reciprocal-space diagram for diffraction from a 2D square lattice with the incident beam k_0 perpendicular to the ab-plane

Figure 13.10 illustrates an example of low energy electron diffraction (LEED), where k_0 is directly perpendicular to the 2D crystal AC-plane. This is a cut in k-space showing only the (h0) rods with $\sim 13\lambda$.

Diffracted wave vectors k_{hk} (or k) extend from C to the intersection point of the (hk) rod and the Ewald sphere. Note that each rod can produce a forward diffracted beam and a back reflected beam, due to two intersections with the Ewald sphere. This diagram also portrays diffraction from a 1D periodic grating, in which case the (h0) rods become (h) planes seen edge-on in k-space.

Low-Energy Electron Diffraction

For a low energy electron diffraction instrument, the accelerating voltage is controlled.

Recall the de Broglie relation for X-rays: $\lambda = \frac{hc}{E}$, where $hc=12.4$ keV. More generally, $\lambda = h/p$, where momentum $p = mv$ and $p = Ec$ for a photon since $m = E/c^2$

- ◊ For non-relativistic massive particles, $\lambda = \frac{h}{mv} = \frac{h}{\sqrt{2m(\frac{1}{2}mv^2)}}$
- ◊ For electrons: $\lambda(\text{\AA}) = \frac{12.3}{\sqrt{V(\text{volts})}} \rightarrow \lambda = 1\text{\AA}$ for 150V (electron beam with a wavelength on one angstrom requires 150 V).
- ◊ For neutrons: $\lambda = 1\text{\AA}$, $KE_n = \frac{150eV}{m_n/m_e} = \frac{150eV}{1839} = 82\text{ meV}$. Greater kinetic energy is required for neutron of greater mass relative to electrons.
- ◊ Thermal neutrons $kT = 26\text{ meV}$ at RT.
- ◊ Neutron diffraction has a different sensitivity to elements than x-rays.

The filament is in vacuum, and a negative potential relative to sample at ground is applied to accelerate the electrons toward the sample. The diffracted electrons hit a fluorescent screen placed below the sample reveals the diffraction spots.

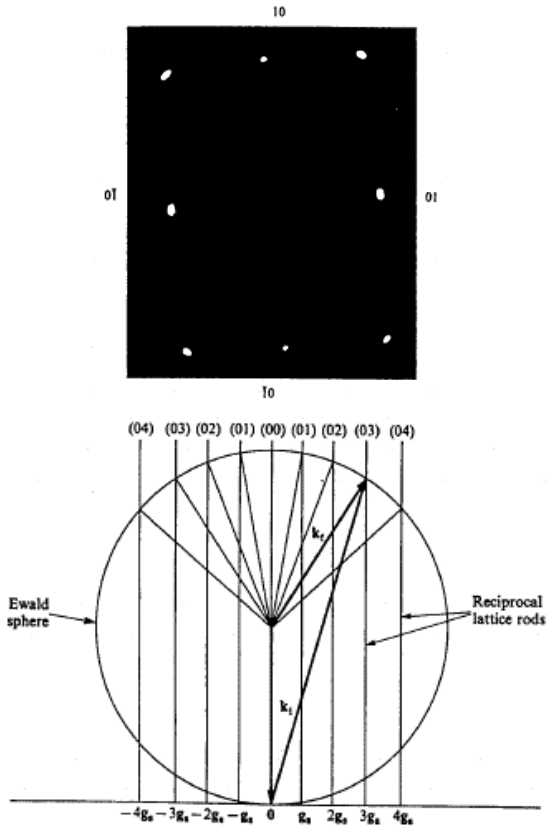


Figure 13.11: LEED pattern from Cu(110) surface

Wavelength gives radius, spacing is $\frac{1}{a}$ for copper.

Why is electron diffraction surface sensitive, in comparison to x-ray diffraction?

Electron beam interacts very strongly with matter, showing scattering from top one or two layers whereas x-rays interact very weakly. Universal mean free path for electrons based on inelastic scattering (plot vs KE)

To achieve surface sensitivity with x-rays we must use total external reflection which produces and evanescent wave with nanometer penetration depth.

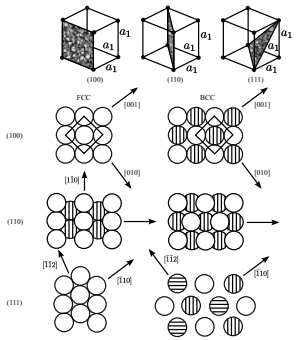


Figure 13.12: Low-index ideal surfaces of hard-sphere cubic-F & cubic-I crystals

4-Bromostyrene SAM on Si (111) surface.

$R(q_z)$ calculated for 1/2 ML coverage.

A z-axis projection can be performed for the structure.



Figure 13.13: caption

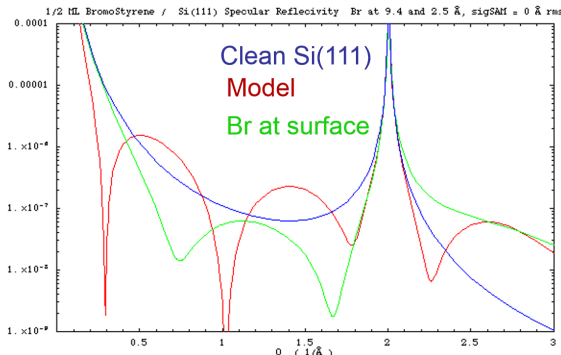


Figure 13.14: simulated specular reflectivity from Si(111) with and without 1/2 mL of bromostyrene.

Substrate Reflectivity:

$$R_s = |r_s(q)|^2$$

like 1D interference function. The period of the subsidiary peaks has gone to zero since N is so large.

$$r_s(q) = \frac{4\pi i r_e F_s(q)}{Aq(1 - e^{-iqc})} \quad (13.5)$$

$$A = \text{Area of } 1\times 1 \text{ u.c.} = 12.8 \text{ \AA}^2$$

$$F_s(q) = 2f_{Si} \cos(qc/8), \quad (13.6)$$

$$c = d_{111} = 3.135 \text{ \AA} \quad (13.7)$$

$$R_{Tot}(q) = |r_s(q) + r_M(q)^2|^2 \quad (13.8)$$

$$r_M(q) = \frac{4\pi i r_e \Theta F_M(q)}{Aq} \quad (13.9)$$

Θ = Molecules per 1x1 u.c = 1/2

$$F_M(q) = f_c(q) \sum_{j=1}^8 e^{iqz_i^C} + f_{Br}(q) e^{iqz^B r} \quad (13.10)$$

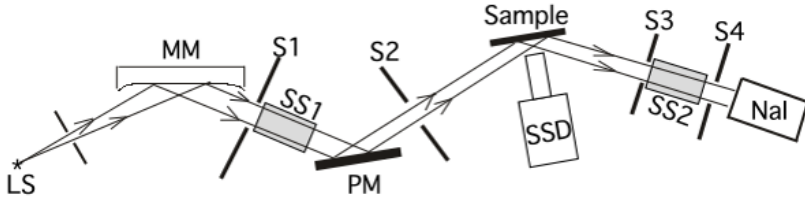


Figure 13.15: Overhead schematic view of 18kW rotating anode setup in Nu X-ray Lab used for XRR, XRF and XSW measurements of SAM-Si (111) samples

- ◊ LS: Vertical Line Source, at focus of parabola.
- ◊ Cu Anode (8.04 keV) used for XRR;
- ◊ Mo anode (17.44 keV) used for XRF and XSW
- ◊ MM: Parabolic multilayer-mirror
- ◊ S1-4: slits
- ◊ SS1&2: solar slit for 1°vertical collimation
- ◊ PM: Si (111) post-monochromator to increase angle resolution
- ◊ Sample on stepping motor driven $\theta - 2\theta$ 2-circle, X-translation, and x -tilt
- ◊ Nal: pulse counting X-ray detector for reflected intensity on 2θ arm
- ◊ SSD: Solid-state XRF detector with pulse-height analysis and multi-channel analyzer

13.4.1 Total External Reflection of X-rays from a Mirror Surface

Start with the zeroth order structure factor $F_{000} = F_0$ = number of electrons in the unit cell

F_0 is related to the zeroth order Bragg diffraction peak

For x-rays, the index of refraction: $n < \approx 1$, because x-rays are above the natural frequency of the electrons in the sample.

$$n = 1 - \delta \text{ where } \delta = \frac{1}{2}\Gamma F_0, \Gamma = \frac{r_e \lambda^2}{\pi V_{u.c.}}, r_e = 2.818 \times 10^{-5} \text{ \AA}$$

N_e = electron density

$\theta_2 = 0 \rightarrow TER \rightarrow \theta_1 = \theta_c$ critical angle

Snell's law

$$n_1 \cos \theta_1 = n_2 \cos \theta_2$$

therefore $\cos \theta_c = n_2/n_1 = n_2$ for $n_1 = 1$

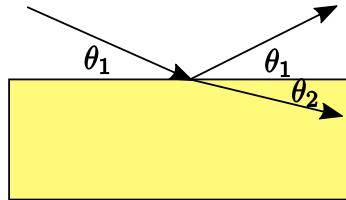


Figure 13.16: caption

Dynamical Theory for Total External Reflection of X-rays form a Mirror Surface

$$n = 1 - \delta - i\beta \quad (13.11)$$

$$\delta = \frac{N_e r_e \lambda^2}{2\pi}, \beta = \frac{\lambda \mu}{4\pi}$$

Fresnel Theory for reflectivity from ideal mirror

$$\frac{E_R}{E_0} = \frac{x - \sqrt{x^2 - 1 - iy}}{x + \sqrt{x^2 - 1 - iy}} \quad (13.12)$$

where $x = Q/Q_c$ and $y = \beta/\delta$

$$R = \left| \frac{E_R}{E_0} \right|^2 \quad (13.13)$$

Penetration Depth: For $\theta \gg \theta_c \rightarrow \Lambda = \sin \theta / \mu$

For $\theta < \theta_C \rightarrow \Lambda$

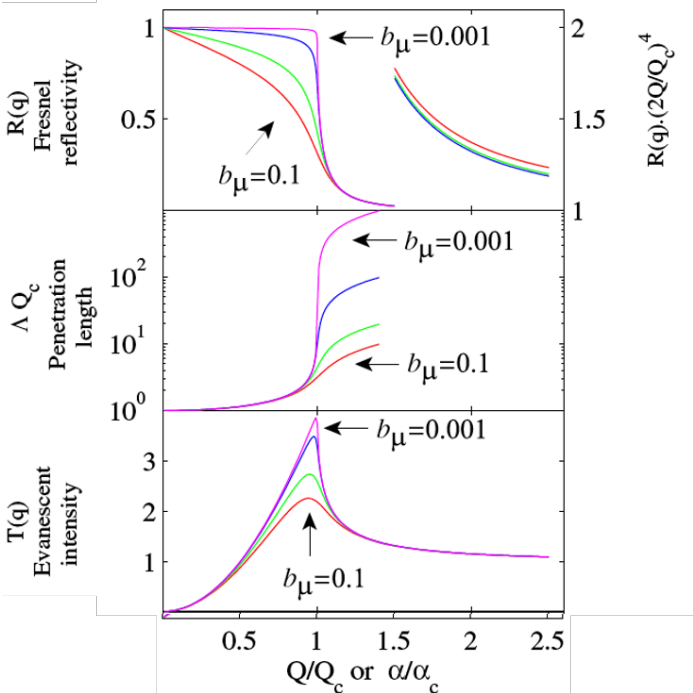


Figure 13.17: caption

This is a Dynamical Theory

X-ray Reflectivity (XRR) Analysis

XRR is very sensitive to surfaces

Example: SAM/Si (111)

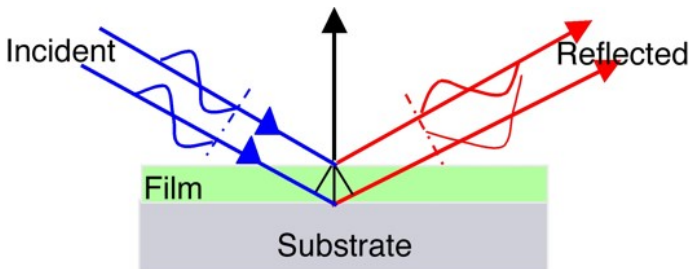


Figure 13.18: SAM/Si (111)

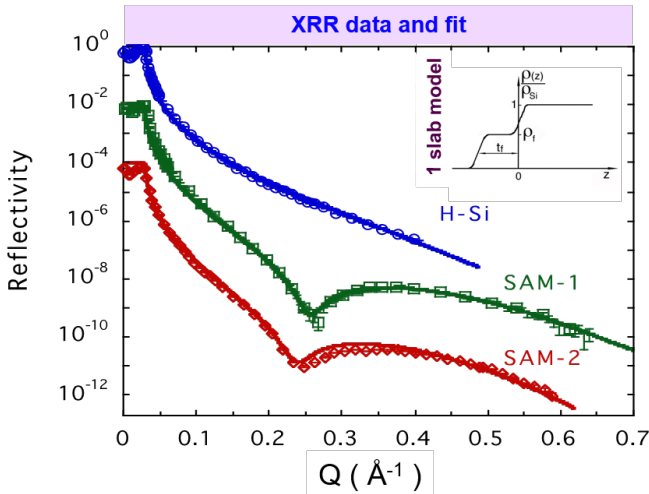


Figure 13.19: XRR data and fit

$$q = 4\pi \sin \theta / \lambda$$

Fresnel Theory:

$$R \sim q \text{ for } q < q_c = 0.031 \text{\AA}^{-1} \text{ Si mirror TER}$$

$$R_F = (2q/q_c)^{-4} \text{ for } q \gg q_c. \text{ Fourier transform of a step function}$$

At 1st dip, the scattered plane-waves from the top and bottom interfaces have a $\lambda/2$ path-length difference (or π phase difference).

Modulation period \rightarrow film thickness Range: 1 to 100nm

Modulation amplitude \rightarrow relative electron density of film

Modulation damping \rightarrow roughness of interface(s) Range: \downarrow 2nm

13.4.2 X-ray Reflectivity of UDAME monolayer on Si (111) Substrate

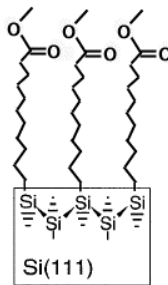
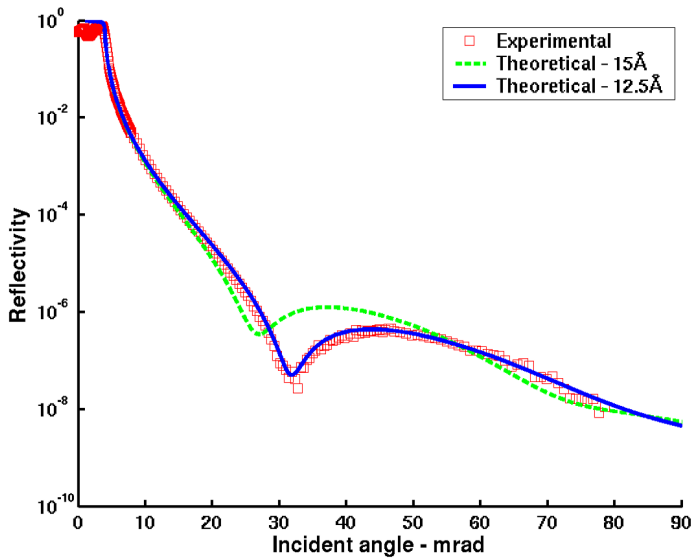
First step in DNA covalent attachment

Sample: Reagan Kinser (Prof. Mark Hersam)

UDAME: $CH_2 = CH - C_8H_{16} - COO - CH_3$

$H - Si(111)$

UDAME-Si (111)

**Figure 13.20:** Sample**Figure 13.21:** Tilt Angle = 33°, 8.04keV @NWU X-ray Lab March 2003

	Exper.	Theor.
$N_e(e^-/\text{\AA}^3)$	0.28	0.30(liq)
$t(\text{\AA})$	12.5	15.0
$\sigma_s(\text{\AA})$	1.8	
$\sigma_l(\text{\AA})$	3.8	

$$0.28e^-/\text{\AA}^3 = 0.41\text{ML}$$

Table 16: caption

13.4.3 X-ray Reflectivity Analysis Fundamentals

Kinematical approach:

$$q = 4\pi \sin \theta / \lambda$$

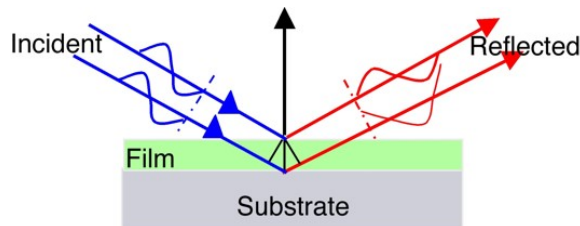


Figure 13.22: caption

$$R(q) = R_F(q)|\Phi(q)|^2 \quad (13.14)$$

$$\Phi(q) = \frac{1}{\rho_\infty} \int \frac{d\rho}{dz} e^{iqz} dz \quad (13.15)$$

FT of gradient of e^- density profile

$$\frac{R(q)}{R_F(q)} = [1 - 4b(1-b)\sin^2(qt/2)]e^{-q^2\sigma^2} \quad (13.16)$$

For 1 slab model

$\rho(z) = e^-$ density profile, $b = \rho_F/\rho_{Si}$, $\sigma = \sigma_s = \sigma_l = (rms) roughness$, t = film thickness

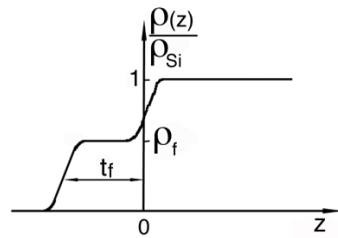


Figure 13.23: caption

b	$t(\text{\AA})$	$\sigma(\text{\AA})$
0.5,0	12.2	3.2
0.5,3	13.3	3.6

Table 17: Table caption

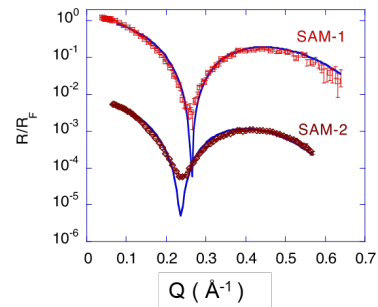


Figure 13.24: XRR Analysis of C_{60} attached to Silica surface; Grown by the Mirkin Group at NU

14 Order-Disorder

14.1 Order-disorder geometry

Consider β Brass CuZn (Cubic Structure)

- ◊ **Ordered** from →Cu at 000, Zn at $\frac{1}{2} \frac{1}{2} \frac{1}{2}$, or CsCl structure
 - Diffraction pattern would indicate Cubic P structure
- ◊ **Disordered** →some Cu occupy Zn sites, some Zn occupy Cu sites. In a randomly disordered structure, each site has an equal likelihood of Zn or Cu occupation Cubic I.
 - Diffraction pattern would indicate Cubic I structure

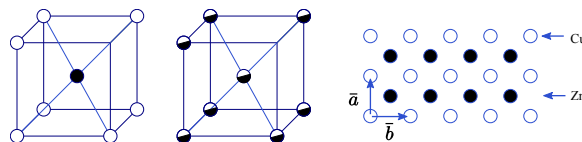


Figure 14.1: Ordered β brass CuZn; Superlattice reflections (100),(300),(111), etc.
→ allowed by Cubic P and disallowed by Cubic I

The Zn is out of phase, and the zinc and copper do not scatter equally. The absent reflections for the randomly disordered phase are called superlattice reflections, and are sensitive to the order of the crystal.

Fundamental reflections are allowed by both P and I : $h + k + l = 2n$

The intensity in the superlattice reflection indicates the degree of order present in the crystal. A high temperature form is generally disordered, while one that is cooling down has ordered domains meeting at domain walls. Zinc would like to have copper nearest neighbors and copper would like to have zinc nearest neighbors, therefore favoring an ordered structure at cooling.

14.2 Long-range Order (W.L. Bragg and E.J. Williams)

Consider a binary compound (CuZn, Au_3Cu , etc.) with 2 types of atoms - A and B - and two correct sites in the unit cell - α and β .

There are N_A atoms of type A and sites α and N_B atoms of type B and sites β . Therefore the total number of atoms in the crystal is given by the following:

$$N = N_A + N_B$$

The following are fractions that change with temperature:

- ◊ r_α = fraction of rightly occupied α sites
- ◊ w_α = fraction of wrongly occupied α sites
- ◊ r_β = fraction of rightly occupied β sites
- ◊ w_β = fraction of wrongly occupied β sites

The fraction of wrongly occupied sites and rightly occupied sites sum to one:

$$r_\alpha + w_\alpha = r_\beta + w_\beta = 1.0$$

In the complete order case, $r_\alpha = r_\beta = 1.0$, $w_\alpha = w_\beta = 0$.

For complete or random disorder $\rightarrow r_\alpha = N_A/N = m_A$

In general $N_a w_\alpha = N_B w_\beta \rightarrow m_A w_\alpha = m_B w_\beta$

14.2.1 Long range order parameter

The unitless quantity S is the long range order parameter, ranging from 0 to 1. Complete order has a value of S=1 and random disorder has a value of S=0.

$$S = r_\alpha - w_\beta = r_\beta - w_\alpha$$

Consider Au_3Cu in P cubic cell

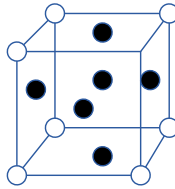


Figure 14.2: P cubic cell

$B \rightarrow Cu$ at (000) β site

$A \rightarrow Au$ at $\{\frac{1}{2}\frac{1}{2}0, \frac{1}{2}0\frac{1}{2}, 0\frac{1}{2}\frac{1}{2}\}$ α sites

$$\diamond m_A = \frac{3}{4} = \frac{N_A}{N} \quad m_B = \frac{1}{4} \quad 2w_\alpha = w_\beta$$

14.2.2 Effective Atomic Scattering Factor

The ensemble average of the atomic scattering factor from the α and β sites is calculated by the following equations:

$$\diamond f_\alpha = r_\alpha f_A + w_\alpha f_B \quad \alpha \text{ site scattering factor}$$

$$\diamond f_\beta = r_\beta f_B + w_\beta f_A \quad \beta \text{ site scattering factor}$$

For hkl unmixed

$$\diamond F_{hkl} = f_\beta e^0 + f_\alpha (e^{\pi i(h+k)} + e^{\pi i(h+l)} + e^{\pi i(k+l)})$$

\diamond The beta site is at 000 and the alpha sites are face centered.

$$\diamond = f_\beta + 3f_\alpha$$

$$\diamond = r_\beta f_B + w_\beta f_A + 3r_\alpha f_A + 3w_\alpha f_B = (3r_\alpha + w_\beta)f_A + (r_\beta + 3w_\alpha)f_B$$

Simplifying with $3r_\alpha + w_\beta = 3(1 - w_\alpha) + w_\beta = 3 - 3w_\alpha + w_\beta = 3$

\diamond yields $F_{hkl} = 3f_A + f_B$ for hkl unmixed (fundamental reflection) independent of S

For hkl mixed (superlattice reflections)

- ◇ $F_{hkl} = f_\beta e^0 + f_\alpha (e^{\pi i(h+k)} + e^{\pi i(h+l)} + e^{\pi i(k+l)})$
- $= f_\beta + f_\alpha(-1)$
- $= (r_\beta f_B + w_\beta f_A) - (r_\alpha f_A + w_\alpha f_B)$
- $= (r_\beta - w_\alpha)f_B - (r_\alpha - w_\beta)f_A$
- $= (f_B - f_A)S$ recall $S = r_\alpha - w_\beta = r_\beta - w_\alpha$ This is completely sensitive to the long range order parameter.

Therefore, for Au_3Cu

- ◇ $F_{hkl} = 3f_{Au} + f_{Cu}$ for hkl unmixed and $F_{hkl} = (f_{Au} - f_{Cu})(-S)$ for hkl mixed

Note $f_{Au} > f_{Cu}$, $z_{Au} > z_{Cu}$, $79 > 29$

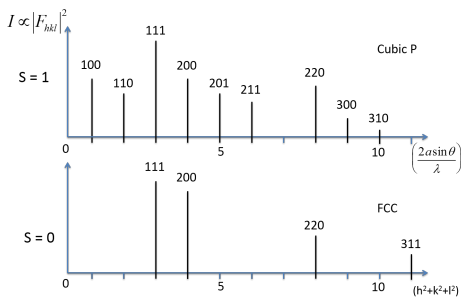


Figure 14.3: Au_3Cu Powder XRD Patterns

Powder diffraction pattern, as S goes from 1 to zero, there is a

14.2.3 Order-disorder phase transitions

Measured by comparing a superlattice XRD peak to a fundamental

Temperature is normalized by the critical temperature. Measure S by comparing a fundamental diffraction peak intensity to a superlattice diffraction peak intensity.

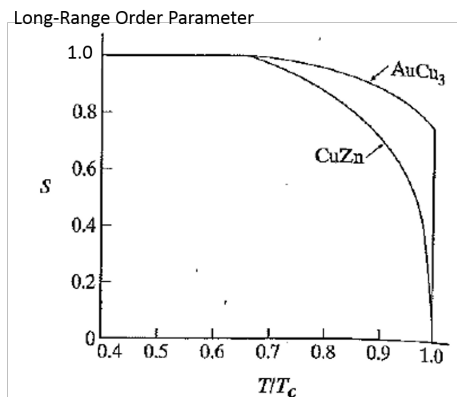


Figure 14.4: Order-disorder phase transitions

1st order phase transition: $AuCu_3$ and Au_3Cu both have a discontinuity at T_C , $T_C = 633K$ for $AuCu_3$

2nd order (continuous) phase transition $CuZn$ $T_C = 730K$

15 Special Topics: X-ray Absorption Spectroscopy (XAS)

As discussed in Ch. 8, X-rays undergo several types of interactions with matter. One of which is the photoelectric effect. Wherein an X-ray photon of energy $E_\gamma = \hbar\omega$ interacts with (is absorbed by) an atom to cause one of its core-level electrons with binding energy, E_B , to be emitted with a kinetic energy,

$$KE = E_\gamma - E_B .$$

As Einstein found, the photoelectron is only emitted for $E_\gamma > E_B$. This Nobel prize winning discovery proved that light behaves as a quantum particle, which we call a photon. The E_γ dependence of the probability (cross-section) for the core photoelectron emission by an atom is described by its X-ray absorption spectrum (XAS), with threshold jumps (or edges) at photon energies matching the binding energies for ground state energy levels of the atom. See Fig. 15.1. Since each element has a unique number of protons (Z), these energy levels are unique for each element. Thus making XAS a sensitive measure of the elemental composition of a material. As we will see, XAS is used to determine the local atomic-scale structure, and unlike XRD, does not require any long-range order. Therefore, XAS can be applied to gasses, liquids, and amorphous solids.

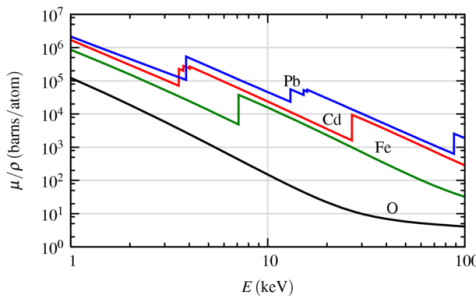


Figure 15.1: X-ray energy dependence of photoelectric effect cross section for four different atoms.

For a monoatomic, ground state, gas like krypton (Kr) you would see an X-ray absorption spectrum that has a linear relation to the photoelectric effect cross section calculated for a single Kr atom. However, the same is not true for atoms arranged in other forms of matter, such as molecular gasses and liquids, pure metals, ionic compounds, etc. For these materials the XAS, or probability for an atom to emit a photoelectron as a function of photon energy, is affected by its closely surrounding atoms in two measurable ways. These two ways refer to different processes that modify different regions of the spectrum as illustrated in Fig. 15.2. In the photon energy range near an absorption edge the XAS is referred to as the X-ray absorption near-edge structure (XANES). The range above the XANES region is referred to as the extended X-ray absorption fine structure (EXAFS).

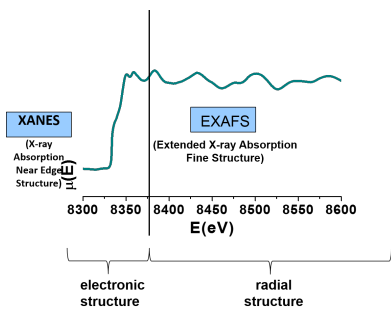


Figure 15.2: The Ni K-edge XAS showing the XANES and EXAFS regions.

15.1 X-ray Absorption Near-Edge Structure (XANES)

Modifications to the XAS in the XANES region are due to changes to the electronic structure of the emitting atom brought about by bonding to neighboring atoms. For example, if we compare the Fe K-edge XANES spectra of pure Fe to that of its oxides: wustite (FeO), hematite (Fe_2O_3), and magnetite (Fe_3O_4) as shown in 15.3, we see that the threshold photon energy for emission of the 1s electron shifts to higher energies as the Fe oxidation state goes from Fe^0 in metallic Fe to Fe^{+2} in FeO , and to Fe^{+3} in Fe_2O_3 . The increase in binding energy occurs because there are fewer outer valence electrons to shield the positive charge from the 26 protons in the iron (Fe) nucleus. This results not only in a shift of the energy edge but also alters the shape of the XANES spectrum. This is due to the photoelectron probing the unoccupied density of states near the Fermi level which differs for different local environment surrounding the Fe atom.

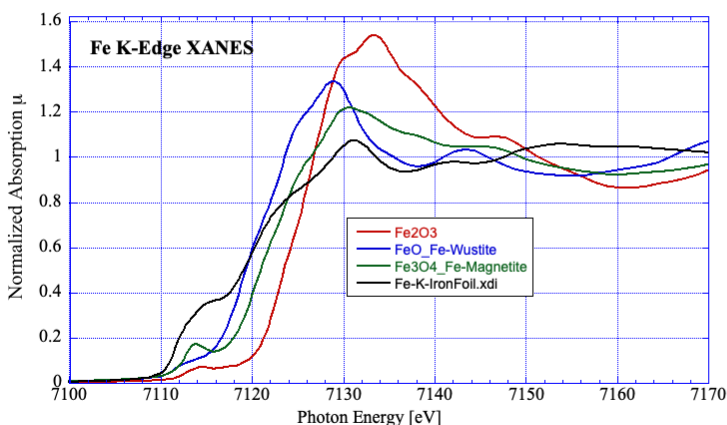


Figure 15.3: Fe K-edge XANES spectra for iron in different oxidation states. This data was collected in transmission mode at NSLS-II beamline 6BM by Supriyo Majumder.

As a simple "fingerprint" technique, one can compare a XANES spectrum from an unknown material to known standard spectra to determine the chemical state and local coordination of the target element. At a more sophisticated level of analysis one would propose a model for the local structure and then compare the density functional theory (DFT) predicted spectrum to the measured spectrum.

15.2 Extended X-ray Absorption of Fine Structure (EXAFS)

The incident x ray beam causes the emission of a core photoelectron. The electron "feels" the surrounding atoms, which yields an absorption spectrum.

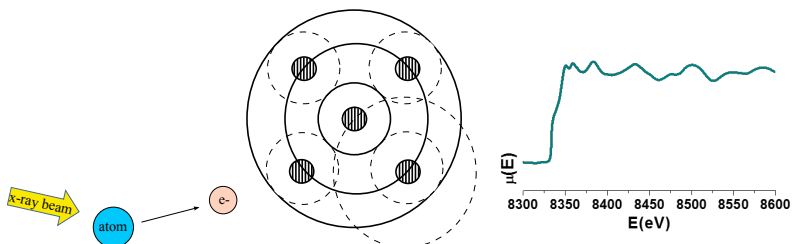


Figure 15.4: XAFS overview

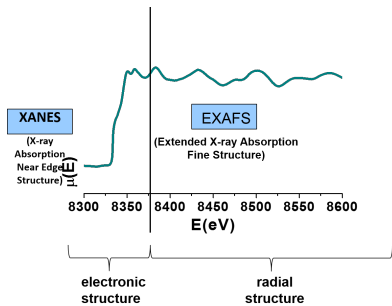


Figure 15.5: Subdivision of the XAS spectrum into XANES and EXAFS regions.

X-ray Absorption Spectroscopy proves the perfect tool for studying in-depth nanoparticle structure.

From the lower energy **XANES** region of the spectrum, we can determine the oxidation state, charge transfer, and chemical fingerprint of our element of interest.

From the extended **EXAFS** region, we obtain information about atomic coordination, inter-atomic spacing, as well as structural and thermal disorder. This ultimately enables us to answer the question: How many of what type of atom are at what distance from my element of interest?

15.3 Outgoing photoelectron: electrons as spherical waves

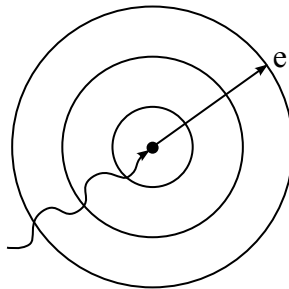


Figure 15.6: Outgoing photoelectron

The de Broglie wave-particle duality principle, as applied to the nonrelativistic emitted photoelectron, tells us that the emitted electron has a wave number k , wavelength λ , and momentum p with the following relationship:

$$k = \frac{2\pi}{\lambda} = p/\hbar$$

$$KE = \hbar\omega - E = \frac{p^2}{2m} = \hbar^2 \frac{k^2}{2m}$$

$$k = \frac{\sqrt{2m(\hbar\omega - E)}}{\hbar}, \text{ or } k(\text{\AA}^{-1}) = 0.521\sqrt{KE(eV)}$$

Due to electron delocalization, we can describe the emitted core photoelectron as a spherical wave to describe its wavefront.

$$\Psi_{out}(\vec{r}') = \frac{\Psi_0 e^{i\vec{k} \cdot \vec{r}'}}{r} = \frac{\Psi_0 e^{ikr}}{r}$$

15.4 XAFS spectra of mono and diatomic gases

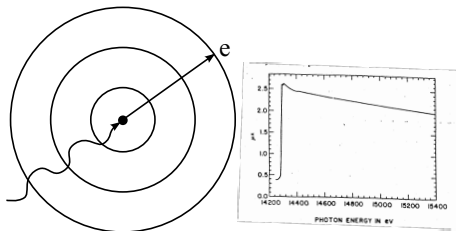


Figure 15.7: Photoelectron wave emitted by a monatomic gas atom like Kr.

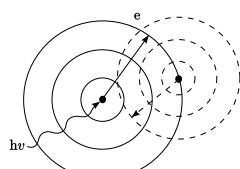


Figure 15.8: Photoelectron wave emitted by an atom in a diatomic gas molecule like Br_2 , which can scatter from the other atom.

How the photoelectron interacts with surrounding atoms

Here, Ψ_{inc} is the wave incident on the second atom at \mathbf{R} , f is the scattered fraction, and $e^{i(k|\vec{r}-\vec{R}|+\phi)}$ is the new spherical wave centered on the second atom

$$\Psi_{scattered}(\vec{r}) = \frac{\Psi_{inc.} f e^{i(k|\vec{r}-\vec{R}|+\phi)}}{|\vec{r}-\vec{R}|}$$

$$\Psi_{inc.} = \Psi_{out.}(\vec{r} = \vec{R})$$

$$\Psi_{scattered}(\vec{r}) = \frac{\Psi_0 e^{ikR}}{R} \frac{f e^{i(k|\vec{r}-\vec{R}|+\psi)}}{|\vec{r}-\vec{R}|}$$

The scattered wave at the center of the original emitting atom (i.e., at $r = 0$):

$$\Psi_{scattered}(\vec{r} = 0) = \frac{\Psi_0}{R^2} f e^{i(2kR+\phi)}$$

15.4.1 How surrounding atoms affect the modulations

How the nearby atom affects the probability of creating a core hole is calculated by summing the two wave functions together at $r=0$.

$$\Psi_{total} = \Psi_0 + \Psi_{scat.} = \Psi_0 \left(1 + \frac{f}{R^2} e^{i(2kR+\phi)} \right)$$

The wavefunction times its complex conjugate gives the probability of creating the core hole.

$$I = \Psi \Psi^* \propto 1 + \underbrace{\frac{2f}{R^2} \sin(2kR + \phi)}_{\text{interference between incoming and outgoing waves}} + \dots$$

interference between incoming and outgoing waves

Recall from earlier in the course: $I = |E|^2$

15.4.2 How XAFS data is measured: transmission and fluorescence detection

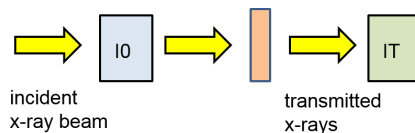


Figure 15.9: Transmission mode for collecting XAS data.

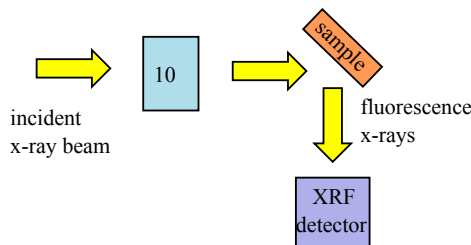


Figure 15.10: Fluorescence mode for collecting XAS data.

Transmission $\mu \propto -\ln(\frac{I_T}{I_0})$ and Fluorescence $\mu \propto (\frac{I_F}{I_0}) \curvearrowright$

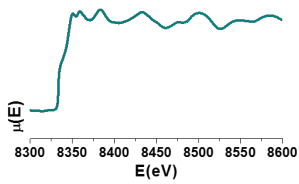


Figure 15.11: Ni K-edge absorption spectrum.

15.4.3 Background subtraction: extracting the quasi-periodic modulations

$\mu \rightarrow \gamma_0$, pre $\rightarrow \gamma$, post $\rightarrow \gamma^*$

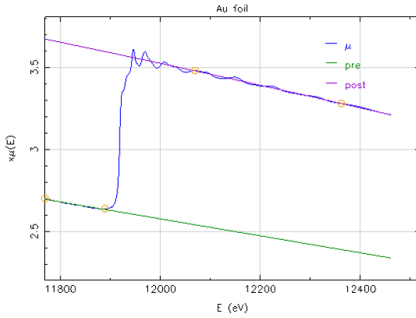


Figure 15.12: Subtracting the background: fitting pre-edge and post-edge lines

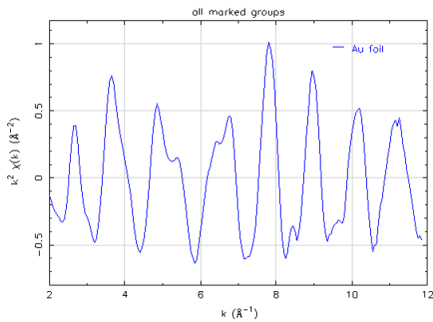


Figure 15.13: Background subtracted data in k-space

$$\chi(E) = \frac{\gamma - \gamma_0}{(\gamma_0 - \gamma^*)} \quad (15.1)$$

15.4.4 E-Space to K-Space conversion

$$E(eV) = h\nu - E_0 = \hbar^2 \times \frac{k^2}{2m} \rightarrow k(\text{\AA}^{-1})0.5123(h\nu - E_0)^{1/2}$$

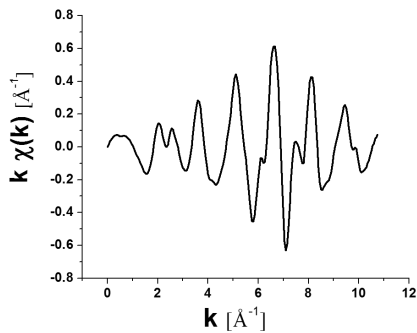


Figure 15.14: K-Space conversion

15.4.5 The EXAFS equation: Describing the k-space data mathematically

$$\chi(k) = \frac{NS_0^2 f(k)}{kR^2} e^{-2k^2\sigma^2} \sin[2kR + \delta(k)] \quad (15.2)$$

N - Degeneracy; S_0^2 - Amplitude Reaction Factor

$f(k)$ - Scattering Factor; k - Wave number

R - Interatomic distance; σ^2 - Mean-squared disorder

$\delta(k)$ - Phase shift

15.4.6 What affects the k-space data?

Reduction in CN \rightarrow reduction in amplitude of k-space oscillations

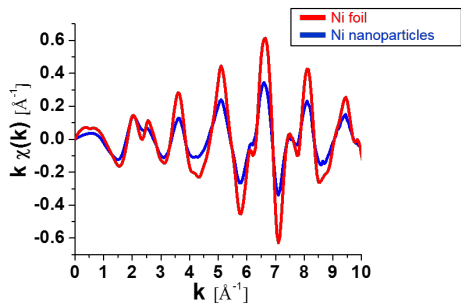


Figure 15.15: Reduction in CN

Change in interatomic spacing → change in period of k-space oscillations

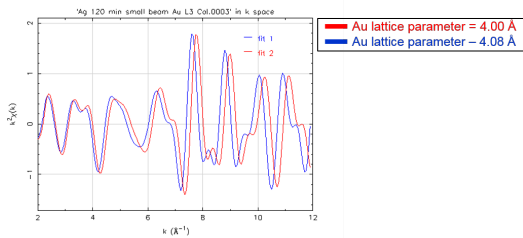


Figure 15.16: Change in interatomic spacing

15.4.7 Fourier transform

$k \rightarrow r$ (Fourier transform):

$$\tilde{A}(r) = \left(\frac{1}{\sqrt{\pi}}\right) \int A(k) e^{2ikr} dk$$

$r \rightarrow k$ (inverse Fourier transform):

$$A(k) = \left(\frac{1}{\sqrt{\pi}}\right) \int \tilde{A}(r') e^{-2ikr'} dr'$$

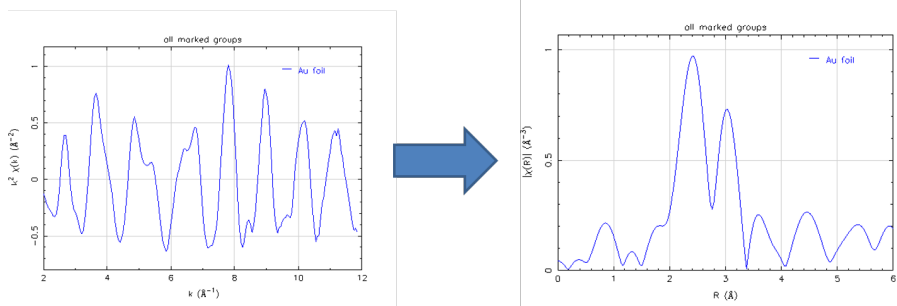


Figure 15.17: Transforming EXAFS data in k-space to EXAFS data in R space

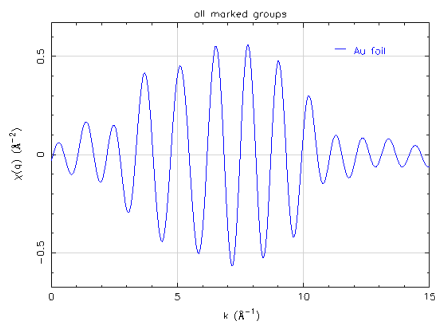


Figure 15.18: Inverse Fourier transform

15.4.8 How do multiple coordination shells affect the spectrum?

In the figure below, the Au spectrum with only the first shell is shown in red, and the Au spectrum with the first four shells is shown in blue.

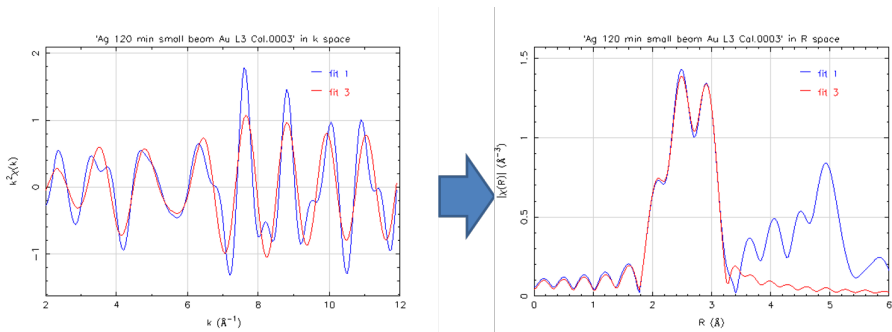


Figure 15.19: Single vs. multiple coordination shells

15.4.9 Recap: Extended X-ray Absorption Fine Structure (EXAFS)

The EXAFS method allows one to determine how many of what type of atom is at what distance from the absorbing atom.

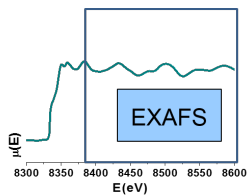


Figure 15.20: EXAFS region

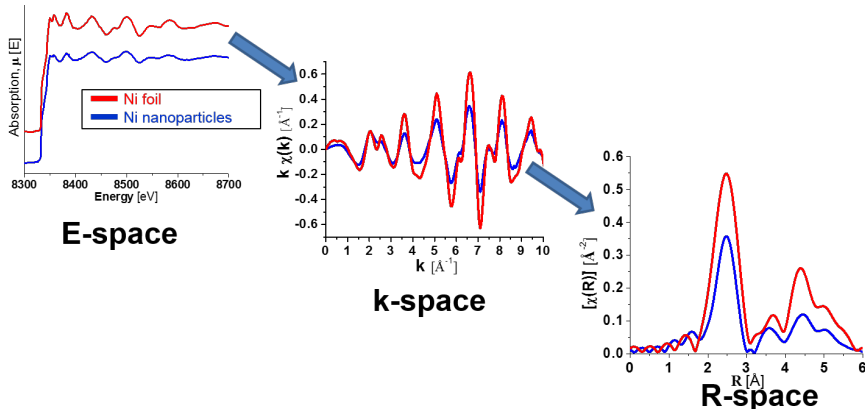
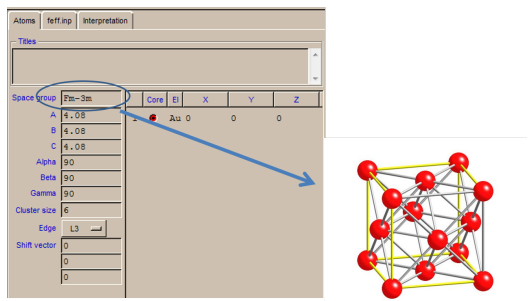


Figure 15.21

15.4.10 The modeling process (crystallography)

Figure 15.22: $Au(FCC)$, space group $Fm\bar{3}m$

Pathways generated from crystal structure

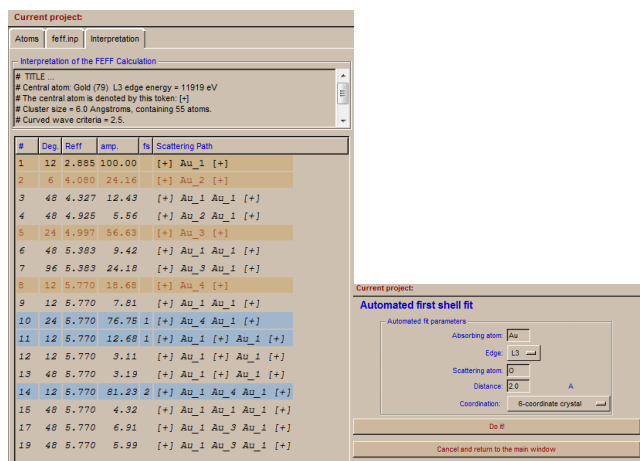


Figure 15.23: Pathways

You can also generate own pathways based on pre-existing knowledge. Each pathway has its own set of variables which must be considered.

15.4.11 The EXAFS equation: how do we treat this in creating a model?

Recall: $\chi(k) = \frac{NS_0^2 f(k)}{kR^2} e^{-2k^2\sigma^2} \sin[2kR + \delta(k)]$

- ◊ Parameters we can determine through theoretical modeling
- ◊ Parameters calculated using fitting program, a function of the material
- ◊ Parameters which are related to the measurement

15.4.12 Variables defined for each pathway

1. N is related to the average coordination number
2. R is defined in fitting as ΔR , or the deviation from the interatomic distance defined in the pathway creation
3. σ^2 is the mean squared disorder, a convolution of the Debye-Waller factor (thermal disorder) and the radial disorder

15.4.13 Evaluating best-fit model (Statistics)

$$\chi^2 = \frac{N_{idp}}{\epsilon N_{data}} \sum_{min}^{max} [Re(\chi_d(r_i) - \chi_t(r_i))^2 + lm(\chi_d(r_i) - \chi_t(r_i))^2] \quad (15.3)$$

$$\chi_v^2 = \frac{\chi^2}{v}; v = N_{idp} - N_{var}; \epsilon = \text{measurement uncertainty}$$

$$R = \frac{\sum_{i=min}^{max} [Re(\chi_d(r_i) - \chi_t(r_i))^2 + lm(\chi_d(r_i) - \chi_t(r_i))^2]}{\sum_{i=min}^{max} [Re(\chi_d(r_i))^2 + lm(\chi_d(r_i))^2]} \quad (15.4)$$

A “good” model minimizes the χ^2 factor and R factor with physically reasonable parameters. There are many “well-fitting” models but only one “correct” model.

15.4.14 Some Examples: Materials Science problems solved by EXAFS

EXAFS is particularly useful in systems which involve amorphous phases or dopant atoms, such as amorphous thin films, heavy atoms in glass or polymeric materials, nanoparticles, phase-change materials, as well as systems where element-specific structural details are not available by other methods

1. EXAFS discovers amorphous phases

Moreau, Ha et. al, 2013. Chem. Mater. 25 (12), 2394.

Moreau, Ha et. al. Nano Letters, 2012, 12, 4530

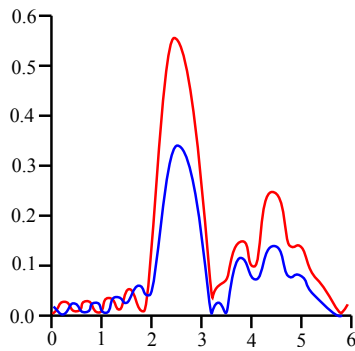


Figure 15.24: Amorphous phases

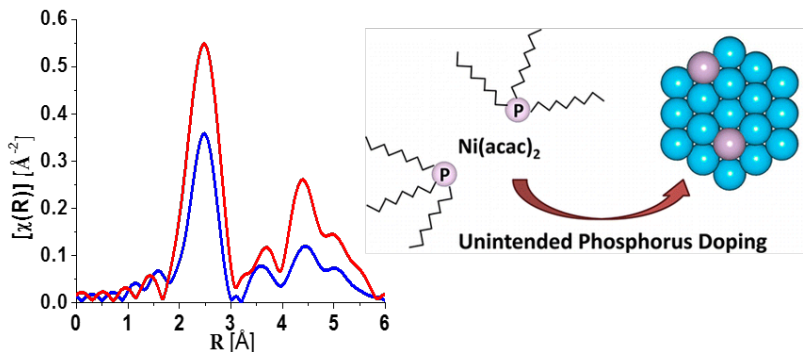


Figure 15.25

2. EXAFS as a means to study nanoscale transformation

Ha, Moreau et. al. J. Mater. Chem, 2011, 21, 11498.

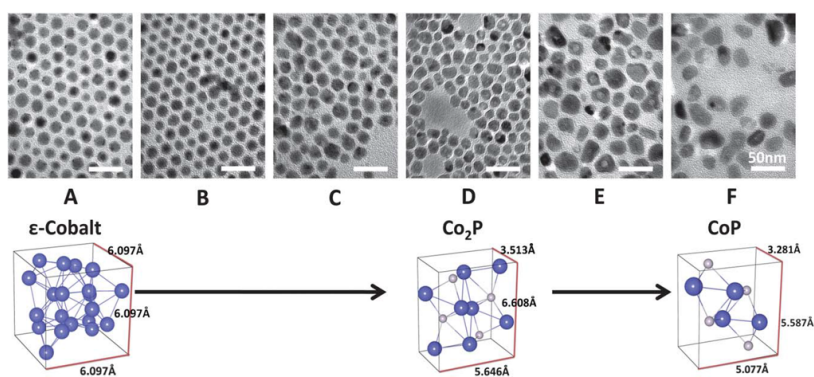


Figure 15.26: Nanoscale transformation

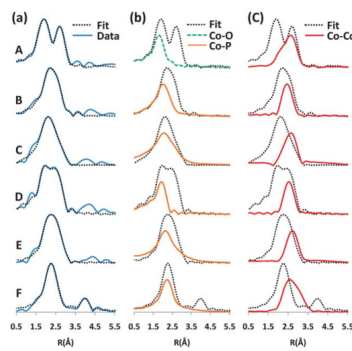


Figure 15.27

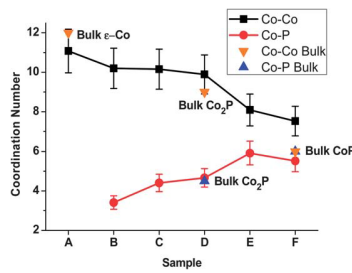


Figure 15.28

3. EXAFS elucidates nanoparticle growth mechanisms

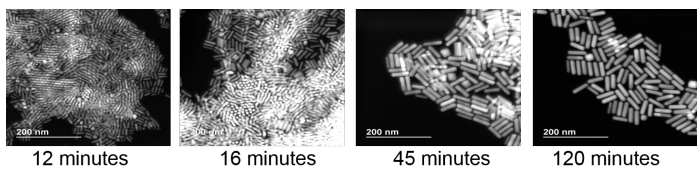


Figure 15.29: caption

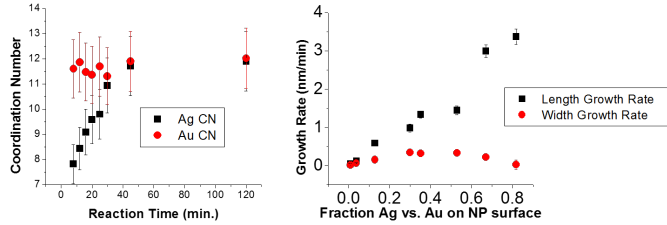


Figure 15.30

From EXAFS results (top) we can determine the coordination number of an average Au atom and Ag atom within the nanorods as a function of reaction time (still time course). We expect that the coordination number will be 12 when the atoms are in the bulk and less than 12 when atoms are on the surface. From the plot we see that although the CN for Au is approximately 12 in all cases, the CN for Ag increases over time until it reaches 12 by ~30 minutes. This reveals that Ag is initially on the nanoparticle surface and over time as deposition of Ag slows, very little to no Ag is on the nanoparticle surface.

Combining EXAFS, XRF and TEM results (bottom) we can relate the growth rate of the length and width of the nanorods (as determined from TEM) to the fraction of Ag vs. Au on the nanoparticle surface (determined from XRF and EXAFS data). We see that the length growth rate of the nanorods is directly correlated with surface Ag. Early on in the reaction (higher fraction Ag vs. Au on the surface), Ag on preferential facets causes the length growth rate to exceed the width and anisotropy is induced. As the reaction progresses and less Ag is on the surface, the length and width growth rates equilibrate and the aspect ratio of the nanorods is maintained.

4. Probing nanoscale surface structure

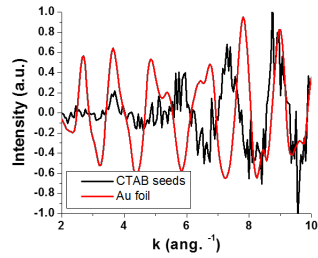


Figure 15.31: Au EXAFS

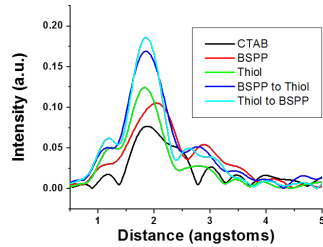


Figure 15.32: caption

2nm particle structure cannot be determined with bulk pathways alone.

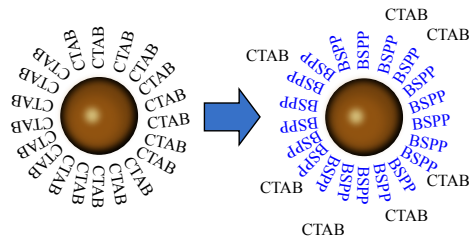


Figure 15.33: caption

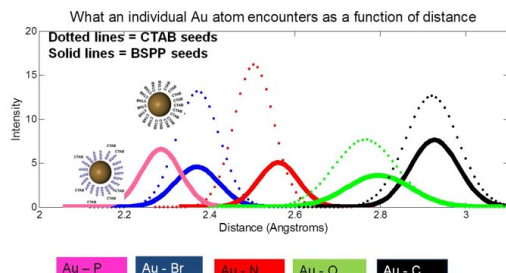


Figure 15.34: What an individual Au atom encounters as a function of distance